Universität Hamburg
DER FORSCHUNG | DER LEHRE | DER BILDUNG

Masterarbeit M.Sc. Physik

Electron Temperature Measurements in Discharge Capillaries

vorgelegt von
Julian Michael Hörsch

2022

Deutsches Elektronen-Synchroton DESY
Universität Hamburg UHH
FLASHForward

Erstgutachter:	Dr. Jens Osterhoff	MPA Group, DESY
Zweitgutachter:	Prof. Dr. Wolfgang Hillert	Institut für Experimentalphysik, UHH
Betreuer:	Dr. Mathew James Garland	MPA Group, DESY

The version of this document differs at three places from the version submitted to the university. The original version did not contain the correct error-bars in Fig. 5.7 and an outdated version of Fig. 5.9. Those figures were updated and two imprecise formulations in Section 2.4.2 adapted for the present document.

Abstract

The electron temperature of hydrogen and argon plasmas, that were produced at gas pressures of a few millibar and with electron densities in the range of 1×10^{15} cm^{-3} to 1×10^{17} cm^{-3}, were investigated. These working points are typical of plasma sources which are used in beam-driven plasma wakefield accelerators such as FLASHForward. The particular plasmas were produced with a high voltage discharge inside a sapphire capillary that allowed, by means of their transparency, optical emission spectroscopy measurements. To determine the electron temperature emission lines were measured and the Boltzmann plot method, which requires optical thin emission lines and partial local thermodynamic equilibrium (pLTE), applied. These requirements were discussed and it was shown that the argon plasma is likely to exhibit stronger deviations than the hydrogen plasma. In hydrogen the maximum electron temperature could be successfully determined to 1.60 eV ± 0.40 eV and this with significantly smaller uncertainties than in previous measurements. For argon this method was less successful and yielded un-physical results. This was in agreement with possibly stronger deviations from the pLTE conditions for argon and necessitated the implementation of a more complex collisional radiative model (CRM) for the temperature determination. The temperatures resulting from the CRM approach were similar to those obtained with the Boltzmann plot analysis and could therefore not improve the results. With these first results this study has laid the ground-work for the electron temperature characterisation in discharge capillaries for FLASHForward, which is a key for improving electron density measurements, plasma modelling and future active plasma lenses.

Kurzfassung

Die Elektronentemperatur in Plasmen aus Wasserstoff und Argon, welche bei wenigen Millibar Gasdruck und mit Elektronendichten im Bereich von $1 \times 10^{15}\,\mathrm{cm}^{-3}$ bis $1 \times 10^{17}\,\mathrm{cm}^{-3}$ erzeugt wurden, wurde untersucht. Diese Arbeitspunkte sind typisch für Plasmaquellen, welche in strahlgetriebenen Plasma-Wakefield Beschleunigern wie FLASHForward eingesetzt werden. Die untersuchten Plasmen wurden durch eine Hochspannungsentladung in einer Kapillare aus Saphir erzeugt, die durch ihre Transparenz auch optische emissionsspektroskopische Messungen ermöglichte. Um die Elektronentemperatur zu bestimmen wurden Emissionslinien gemessen und die Boltzmann-Plot Methode, welche optisch dünne Emissionslinien und partielles lokales thermodynamisches Gleichgewicht (pLTE) erfordert, angewandt. Diese Voraussetzungen wurden diskutiert und dabei gezeigt, dass für Argon stärkere Abweichungen als für Wasserstoff wahrscheinlich sind. In Wasserstoff konnte die maximale Elektronentemperatur erfolgreich und mit signifikant kleineren Unsicherheiten als in vorherigen Messungen, zu $1.60\,\mathrm{eV} \pm 0.40\,\mathrm{eV}$ bestimmt werden. Für Argon war diese Methode weniger erfolgreich und resultierte in unphysikalische Ergebnisse. Dies war in Übereinstimmung mit den möglicherweise stärkeren Abweichungen von den pLTE Bedingungen für Argon, was die Implementierung eines koplexeren Kollisions-Strahlungs-Models (CRM) zur Temperaturbestimmung erforderte. Die resultierenden Temperaturen dieses CRM Ansatzes waren ähnlich zu denen der Boltzmann-Plot Methode und konnten diese Ergebnisse deshalb nicht verbessern. Mit diesen ersten Ergebnissen legt diese Arbeit die Grundlage für die Charakterisierung der Elektronentemperatur in Hochspannungsentladungskapillaren für FLASHForward, was ein Schlüssel zur Verbesserung von Elektronendichtemessungen, Plasmamodellierung und zukünftigen aktive Plasmalinsen ist.

Contents

Chapter 1

Introduction

Plasma wakefield accelerators (Tajima et al. 1979; Chen et al. 1985) are advanced accelerator concepts which offer acceleration gradients that are orders of magnitudes larger than achievable with conventional accelerators. By this, they have the potential to decrease the size of accelerators by the same factor (Hooker 2013). They proved to have the capacity to create electric fields and accelerate electron bunches within cm-scale plasma cells with up to 100 GV m^{-1} (Blumenfeld et al. 2007; Gonsalves et al. 2019; Litos et al. 2014; Esarey et al. 2009). The properties of these accelerating fields are controlled by the local plasma electron density, which is therefore a key parameter in the design of such accelerators. For creating these plasma structures, capillary discharges (Butler et al. 2002; Spence et al. 2003; Karsch et al. 2007; Leemans et al. 2014) are commonly employed, because they are capable of providing specific plasma density profiles for various purposes (Garland et al. 2021).

Under this perspective it becomes highly relevant to investigate the plasma properties as electron temperatures and electron densities for the characterisation of these plasmas. Temperature measurements on their own can already help to improve the understanding of the uncertainty in electron density measurements from plasma diagnostic techniques, like the commonly used spectral line broadening method (Gigosos et al. 1996; Garland et al. 2021). They are also essential for the operation of future active plasma lenses (Panofsky et al. 1950; Lindstrøm et al. 2018), where a precise knowledge of electron density and temperature is necessary to achieve a strong focusing of the particle beams. Already, they are also needed to compare simulations of the discharge plasma with experiments and to improve these simulations.

As an experimental facility and high-performance test-bed, the FLASHForward facility (D'Arcy et al. 2019) provides an environment for plasma wakefield accelerator research and enables the study of capillary discharge plasmas. For experiments at FLASHForward typically argon plasmas are used and for research purposes also hydrogen plasmas, which are easier to approach from a theoretical view. The aim of this study is to investigate the plasma properties in those gases within the regimes in which FLASHForward operates. The working point for FLASHForward yields plasmas with peak electron densities of 1×10^{17} cm^{-3} (Garland et al. 2021) and pressures in the few mbar range inside the discharge capillary.

A promising and simple technique to explore the plasma properties is plasma spectroscopy

and in particular optical emission spectroscopy (OES) (Fantz 2006; Griem 1997; Gigosos et al. 1996). OES is a passive method, experimentally simple to establish and allows, with the observation of radiation from atoms, molecules or ions a non-invasive, real time characterization. To investigate electron temperatures with OES, the intensity of spectral emission lines can be used. The emission lines are correlated with the particle density of the transitions upper level and this density is dependent on plasma properties as electron density and temperature and makes therefore an electron temperature determination possible. Depending on the properties of the plasma, different schemes must also be applied to extract the temperature and it is therefore important to know which plasma conditions prevail.

Chapter 2 will outline the theoretical concepts for electron temperature measurements in discharge plasmas and Chapter 3 will introduce the experimental setup and methods. Chapter 4 and Chapter 5 will be devoted to the data analysis and the discussion of the experimental results for hydrogen and argon while Chapter 6 will conclude the results and give an outlook along possible improvements.

Chapter 2

Theoretical Framework

This chapter will establish a framework for the characterization of electron temperatures in hydrogen and argon plasmas and opens with the fundamental equilibrium relations and the definition of the electron temperature. Subsequently this chapter will discuss the validity regimes of those equilibria, which models need to be applied in each case and finally connect these models to spectroscopic measurements.

2.1 Kinetics of Atomic Energy Levels in Plasmas

It is initially important to understand how internal plasma processes and characteristic properties such as electron density and temperature are related. By ionizing a gas, electrons are removed from their atoms and can move independently from the remaining ions. An electron may now collide with another atom or ion and influence its energy state, for example by excitation. There are a number of processes, mainly collisional and radiative processes, which change the energy states of atoms or ions and therefore contribute to the population and de-population of atomic or ionic energy levels. In a general form, the local population $n_z(p)$ of an ion with charge z and atomic state p is determined by a rate equation as (Kunze 2009, p. 135, Graef 2012, p. 10)

$$\frac{\partial n_z(p)}{\partial t} + \nabla \cdot \Gamma_z(p) = R_z(\rightarrow p) - R_z(p \rightarrow) \tag{2.1}$$

which is the zeroth moment of the Boltzmann transport equation. Here $R_z(\rightarrow p)$ is the sum of all rates of radiative and collisional processes that contribute to the population of level p, $R_z(p \rightarrow)$ the sum of depopulating rates and $\Gamma_z(p)$ the flux by diffusion and convection (e.g. reactions with the wall). The left hand side of Eq. (2.1) can also be considered as temporal and spatial relaxation of the population density (Vries et al. 2006).

To completely model the plasma kinetics we would need to take all energy levels p of atoms and ions into account and would obtain a multitude of coupled equations with the form of Eq. (2.1). The system is coupled since each equation for a level p also depends on other levels q that are themselves described by a balance equation. It is not possible to solve this set of coupled equations in a general way to obtain the population densities that describe the state of the plasma, since a large number of processes and levels would have to be considered and not all rate constants for those processes are known with good enough accuracy (Kunze 2009).

Instead of solving the whole system, the number of equations is therefore commonly reduced to the most relevant subset to simplify the analysis (Kunze 2009; Graef 2012).

2.1.1 Quasi Steady State Solution

For many plasmas an additional simplification can be obtained if we distinguish between the time that is needed to establish a steady state for an excited energy level and ground states or meta stable energy levels. Steady state is established if populating and depopulating processes equilibrate. For excited levels the longest time scale to reach this is the relaxation time by radiative decay (Bates et al. 1962). This is the inverse of the smallest Einstein coefficient A for spontaneous emission from level p to a lower energy level, such that the relaxation time is $\tau_{\text{relax}} = 1/A(p \rightarrow)$. For many plasmas these time scales for excited levels are approximately on the order of 1×10^{-8} s (Vries et al. 2006). The slowest relaxation times for free electrons, ground level atoms and sometimes also meta stable states are much longer because ionization and recombination affect these populations on longer time scales (Kunze 2009, p. 135).

The time scales for transport related processes (left hand side of Eq. (2.1)) are often on the order of 1×10^{-4} s (Vries et al. 2006), which means that excited levels reach steady state without being affected by the much slower transport. Transport related processes and as such the temporal and spatial relaxation in Eq. (2.1), can therefore be neglected for most of the excited levels and the left hand side of Eq. (2.1) set to zero. This is the so called quasi steady state solution (QSSS) (Bates et al. 1962), which can be applied to excited levels but not to ground levels or sometimes also meta stable levels. The population density of excited levels is also usually much smaller than that of free electrons and bare nuclei. If the mean thermal energy in the system is also much less than the energy of the first excitation, then the density $n(p)$ of an excited level p is also much smaller than the ground state density n_g (Bates et al. 1962).

2.2 Plasma Equilibrium Relations

The collisional and radiative processes introduced above constitute of pairs of excitation and de-excitation processes that are, under certain conditions, in equilibrium with each other and depending on which equilibria prevail we can classify a plasma in different categories.

2.2.1 Thermodynamic Equilibrium

In thermodynamic equilibrium (TE) all types of processes are in balance and the physical state of the plasma can be fully determined by its temperature. Thermodynamic equilibrium can be conceptualized as a plasma which is confined in a closed theoretical box that includes a radiation

field that can not escape. In this conceptual picture the plasma is in thermodynamic equilibrium with the walls at temperature T and the physical state is fully described by the temperature. For such plasmas the following relations (Kunze 2009, p. 136) hold:

- The radiation field is fully described by Planck's law (spectral radiance of the blackbody):

$$L_\lambda^B(\lambda, T) = \frac{2hc^2}{\lambda^5} \frac{1}{\exp(h\nu/k_B T) - 1} \tag{2.2}$$

  were h is the Planck constant, c the speed of light, λ the wavelength, ν the frequency, k_B the Boltzmann constant and T the temperature (Kunze 2009, p. 76).

- The energy / velocity distribution of each particle species (electrons, ions, neutral atoms) can be described by a classical Maxwell-Boltzmann distribution, which for the energy E can be written as (Boffard et al. 2010)

$$f(E) = 2\sqrt{\frac{E}{\pi}} \left(\frac{1}{k_B T}\right)^{3/2} \exp\left(-\frac{E}{k_B T}\right), \tag{2.3}$$

  where T is the temperature and k_B the Boltzmann constant. For very high electron densities, when quantum effects manifest, the electron distribution follows a Fermi-Dirac distribution instead.

- The population density of an energy level is given by the Boltzmann distribution. The ratio $n_z(u)/n_z(l)$ of two states (u) and (l) with $(u) > (l)$ of an atom or ion with charge z is then given by the ratio of the Boltzmann distributions (not to be confused with the Maxwell-Boltzmann distribution) for the respective levels. This leads to

$$\frac{n_z(u)}{n_z(l)} = \frac{g_z(u)}{g_z(l)} \exp\left(-\frac{E(u) - E(l)}{k_B T}\right), \tag{2.4}$$

  where g is the degeneracy of the energy level.

- A process and its inverse process are in equilibrium with each other and the number of excitation processes equals to the number of de-excitation processes (Graef 2012, p. 55):

$$n_e n^B(p) K(p, q) = n_e n^B(q) K(q, p), \tag{2.5}$$

  where n_e is the electron density, $K(q, p)$ the rate constant for the process and n_p^B and n_q^B the level density of level p respectively q according to the Boltzmann distribution. This is the so called principle of detailed balance (Kunze 2009, p. 139).

The Boltzmann distribution of Eq. (2.4) can be extended to continuum states to find a relation for the ionization stages in thermodynamic equilibrium plasmas as shown by Kunze 2009,

pp. 137–138. The result is the Saha, also known as Saha-Eggert equation which relates the population density ratio of two adjacent ionization stages in a thermodynamic equilibrium to each other:

$$\frac{n_{z+1}(g)n_e}{n_z(q)} = 2\frac{g_{z+1}(g)}{g_z(q)}\left(\frac{m_e k_B T}{2\pi\hbar^2}\right)^{3/2}\exp\left(-\frac{E_{z,+}(q)}{k_B T}\right), \tag{2.6}$$

where $n_{z+1}(g)$ is the population density for the ground state of an ion with charge $z+1$, $n_z(q)$ the density at level q for an ion with charge z, m_e the electron mass, k_B the Boltzmann constant, T the temperature and $E_{z,+}(q) = E_z(+) - E_z(q)$ the ionization energy of level q.

2.2.2 Local Thermodynamic Equilibrium

Although thermodynamic equilibrium is a powerful concept to simplify the physics in plasmas, it will never be realized in laboratory plasmas, but prevails in the interior of stars (Kunze 2009, p. 139). The limiting factor which prevents TE from being realized is usually the radiation field, which against the prerequisites for TE, often easily escapes from the plasma. To avoid the radiation to escape, the plasma would need to be optically thick at all frequencies which would essentially be a black body (Cristoforetti et al. 2010). In this case emission and absorption processes would equilibrate.

The concept of complete TE can be weakened by the concept of local thermodynamic equilibrium (LTE) where the radiation field does not need to follow a Planck distribution. It is called local because the non-local nature of radiation, which means that emission is produced at some location in the plasma and absorbed at another, is excluded in this concept. If the electron densities are high enough such that electron collisions maintain a steady-state population density, then radiative processes become unimportant and the radiation (Planck) balance decouples from the Boltzmann and Saha balances. In this case the level populations will still be distributed according to a Boltzmann distribution (Eq. (2.4)) and the ionization stages according to the Saha equation (Eq. (2.6)) (Kunze 2009, pp. 139–140). In such an equilibrium the energy loss by radiation (not absorbed radiation) is small compared to that energy involved in other (collisional) processes and LTE can be assumed. The physical state of the plasma in LTE is no longer fully described by only one temperature T, but is rather described by different temperatures for the radiation field and the other constituents, which relate with (Cristoforetti et al. 2010):

$$T = T_\mathrm{e} = T_\mathrm{h} \neq T_\nu, \tag{2.7}$$

where T_e is the electron temperature, T_h the heavy particle temperature (atoms and ions) and T_ν the temperature of the radiation field.

2.2.3 Partial Local Thermodynamic Equilibrium

Likewise, the concept of LTE can be replaced by the less stringent concept of partial local thermodynamic equilibrium (pLTE) where only a subset of all energy levels needs to be in LTE (Kunze 2009; Cristoforetti et al. 2010). If pLTE exists there will be a boundary level n above which the energy levels will be populated according to a Boltzmann distribution as in LTE, but below which (including n) there will be deviations from the Boltzmann distribution and LTE because the imbalanced Planck equilibrium will contribute too much.

The process of electronic de-/excitation is more efficient for highly excited levels, when with increasing principal quantum number the energy level spacing ΔE_{nm} decreases, the radiative de-excitation however, is less efficient for higher excited levels with smaller energy level spacings (Cristoforetti et al. 2010). This also implies for plasmas which are not in LTE, that at a fixed electron density there will be a level where the de-excitation rate by electron collisions and radiative decay is the same. To illustrate the concept of pLTE we start from the ionization limit and descend to lower lying energy levels (Drawin 1969). Close to the ionization limit, two-body ionization and three-body collisional recombination are frequent and therefore the bound electrons will be in LTE with the free electrons. By descending to lower lying levels, the coupling of the excited levels with the free electrons will decrease. For highly excited levels the collisional excitation and de-excitation rates between closely spaced levels will still be dominant, such that LTE with the free electrons is established, but the situation changes if a level u is reached where the spontaneous radiative decay to a level lower than u is equal or larger than the collisional induced de-excitation to level $l = u - 1$. If the collisional excitation from level l to u can not compensate this stronger radiative decay, this will lead to deviations from LTE for this energy level.

For energy levels that are not in pLTE the temperature will also not equal the electron temperature whilst it will equal the electron temperature for the levels that are in pLTE (Cristoforetti et al. 2010). The relation of Eq. (2.7) does therefore also not apply for pLTE and the temperature of the heavy particles T_h decouples from the electron temperature T_e.

2.3 Electron Temperature

The electron temperature T_e is only defined if the electron energy distribution (EEDF) follows a Maxwell-Boltzmann distribution (Eq. (2.3)) because it is the temperature itself that characterizes this Maxwell-Boltzmann distribution. In TE this distribution is statistically the most probable one, but for example in low temperature and weakly ionized plasmas this is often not the case (Boffard et al. 2010; Carbone et al. 2012) and there it is not generally valid to assume Maxwellian

EEDFs (Fantz 2006). If a Maxwellian EEDF and LTE prevails, then the level population follows a Boltzmann distribution and the temperature in Eq. (2.4) is sometimes also denoted as the the excitation temperature T_{exc} (Kunze 2009, p. 188).

For weakly ionized and low temperature plasmas, or medium to high pressure plasmas, often some part of the EEDF is over or underpopulated and for example the tail (high energy part) of the distribution does not follow the Maxwellian shape. For gas mixtures the deviations can be even stronger, such that tail and bulk can not be distinguished any longer (Carbone et al. 2012). Since the electron temperature is only defined for Maxwellian distributions, a substitute concept for arbitrary EEDFs is to use an effective electron temperature which is 2/3 of the average electron energy (Boffard et al. 2010). Sometimes the EEDF can also be described by a 'bi-Maxwellian' distribution with different temperatures for the bulk and the tail or, if needed, also by more complex distributions (Boffard et al. 2010). If non-Maxwellian distributions are expected, Boltzmann solvers (Hagelaar et al. 2005) or particle in cell (Siepa et al. 2014) can be useful. In the discharge plasmas in this study it was expected and also for simplicity assumed, that the EEDF is close to a Maxwellian after approximately 10 ns of the discharge (private communications Gregory Boyle).

2.4 Validity Criteria for LTE Conditions

To quantitatively discuss if LTE or pLTE conditions hold for certain plasma conditions, it is useful to introduce validity criteria based on parameters the electron density. Strictly, the concept of LTE requires the plasma to be in a temporal steady state and also to be spatially uniform / homogenous (Fujimoto et al. 1990). Plasmas that have sufficiently high electron densities to maintain LTE are however rarely at the same time homogenous and stationary (Griem 1963). For simplicity only plasmas that are homogenous in space will be discussed, for non-homogenous plasmas see Cristoforetti et al. 2010. It is indeed likely that the plasmas which we are concerned with are non-homogenous, at least at some point of their evolution, but as process like diffusion to the walls, which lead to non-homogeneity are not entirely understood, non-homogeneity was not considered in this analysis.

2.4.1 Criteria for LTE

The simplest case is first to consider a plasma homogenous in space and without time evolution (steady state). If we start from complete LTE and decrease the electron density, electron-atom collisions will become less frequent and the levels separated by the largest energy gap, will first show deviations from the Boltzmann distribution (Kunze 2009, p. 141). Griem 1963 suggested

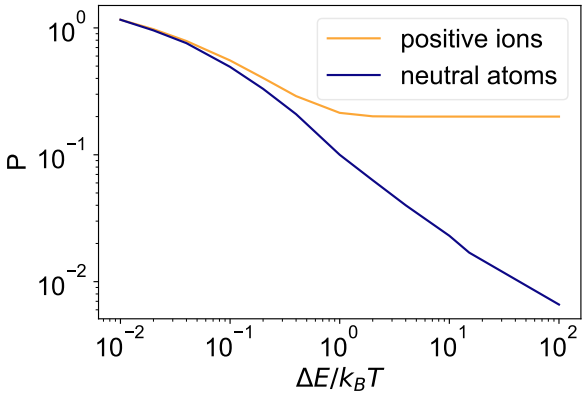

Figure 2.1: The dimensionless Gaunt factor for positive ions and neutral atoms. The plot was reproduced with the data from van Regemorter 1962.

that a minimum electron density is needed to reach LTE and proposed that collisional rates between levels with the largest energy gap should be ten times larger than the corresponding radiative rates, such that the deviation from LTE is within 10 %. This is to say (Kunze 2009):

$$n_z(u) n_e X_z(u \to l) \geq 10\, n_z(u) A_z(u \to l), \tag{2.8}$$

where $n_z(u)$ is the population density of an upper level of an atom / ion with charge z, n_e the electron density, $X_z(u \to l)$ the collisional rate from an upper level u to a lower level l and $A_z(u \to l)$ the Einstein coefficient for spontaneous radiative decay to level l.

We want to use Eq. (2.8) to find a validity criterion for LTE based on the electron density. First, we express the collisional de-excitation $X_z(u \to l)$ with the effective Gaunt factor approximation (Kunze 2009, p. 140)

$$X_z(u \to l) = 16\sqrt{\frac{\pi}{3}} \alpha c \pi a_0^2 \frac{g_z(l)}{g_z(u)} f(l \to u) \frac{E_R}{\Delta E_{ul}} \left(\frac{E_R}{k_B T_e}\right)^{1/2} P\left(\frac{\Delta E_{ul}}{k_B T_e}\right), \tag{2.9}$$

where α is the fine structure constant, c the speed of light a_0 the Bohr radius, g_z the corresponding degeneracy, $f(l \to u)$ the absorption oscillator strength, E_R the Rydberg energy, $\Delta E_{ul} = E_z(u) - E_z(l)$ the energy difference between level u and l, k_B the Boltzmann constant and P the Gaunt factor. The Gaunt factor was originally published by van Regemorter 1962 and measures the probability that an incident electron is promoted from the initial energy E_i to a final energy E_f. The dimensionless Gaunt factor is a quantum-mechanical correction factor (Hey 1976; Cristoforetti et al. 2010) for positive ions and neutral atoms and is shown in Fig. 2.1.

The radiative decay rate for dipole transitions $A_z(u \to l)$ can be written as (Kunze 2009)

$$A_z(u \to l) = \frac{2 r_e}{\hbar^2 c} \frac{g_z(l)}{g_z(u)} f(l \to u) {\Delta E_{ul}}^2, \tag{2.10}$$

with the electron radius r_e and the reduced Planck constant $\hbar$. Inserting Eqs. (2.9) and (2.10) into Eq. (2.8), yields after reordering a criterion for the critical electron density for LTE conditions

(Hey 1976; Kunze 2009)

$$n_e \geq \frac{5}{16\pi}\sqrt{\frac{3}{\pi}}\left(\frac{\alpha}{a_0}\right)^3\left(\frac{\Delta E_{ul}}{E_R}\right)^3\left(\frac{k_B T_e}{E_R}\right)^{1/2}\left(P\left(\frac{\Delta E_{ul}}{k_B T_e}\right)\right)^{-1} \tag{2.11}$$

$$\approx 2.7\times 10^{19}\left(\frac{\Delta E_{ul}}{\mathrm{eV}}\right)^3\left(\frac{k_B T_e}{\mathrm{eV}}\right)^{1/2}\left(P\left(\frac{\Delta E_{ul}}{k_B T_e}\right)\right)^{-1}. \tag{2.12}$$

Equation (2.12) is in units of m^{-3}, T_e in Kelvin and $k_B T_e$ in units of eV. Equation (2.12) has been derived by different authors in similar forms and sometimes also without the quantum mechanical correction of the Gaunt factor (Griem 1963). This criterion is also called the McWhirter criterion (Cristoforetti et al. 2010; Mendys et al. 2014).

For complete LTE, the condition Eq. (2.12) must hold for the largest energy gap between adjacent levels. As the energy difference ΔE_{ul} between two levels u and l decreases with increasing quantum number the largest energy gap corresponds to the difference between ground state and first excited level. If there exists a low lying metastable level (has dipole forbidden transitions) which would be the first excited energy level, then attention must be paid because this breaks some assumptions made in the derivation of Eq. (2.12), see Cristoforetti et al. 2010. To overcome this problem to a first approximation the energy level corresponding to the first dipole allowed resonance transition should be used. Resonance lines are emission lines that are the result of transitions ending on the ground state of the atom or ion (Kunze 2009, p. 82). A more rigorous treatment of this problem was conducted by Hey 1976.

Equation (2.12) is valid if emitted radiation is not absorbed (optically thin plasma), but if radiation is absorbed (optically thick plasma) this will lower the necessary electron density to reach LTE, because the Planck balance is in less dis-equilibrium. If the electron density is too low to reach complete LTE, then the ground state will be overpopulated with respect to the LTE case, but if the plasma is optically thick, self-absorption tends to re-equilibrate this dis-equilibrium. In this case the overpopulated ground state will be depopulated again by self-absorption as photons from a transition from level u to the ground state g will cause the re-excitation $g \rightarrow u$ (Cristoforetti et al. 2010). This can lead to a relaxation of the LTE condition by a factor of 10 (Griem 1963).

The criterion of Eq. (2.12) is only a necessary but not sufficient criterion to asses LTE (Cristoforetti et al. 2010) and was also deduced for steady state conditions in ionization balance (ionization and recombination are in equilibrium). When temporal and spatial variations are too strong, then the steady state assumption breaks down and the system must by described by space-resolved CRMs that also include for example expansion dynamics (Cristoforetti et al. 2010). To verify that temporal variations are not too strong the conditions for steady state must also be checked.

2.4.2 Criteria for Steady State in LTE

To reach complete LTE, the QSSS (Section 2.1.1) strictly would need to apply for the rate equations (Eq. (2.1)) of all energy levels including the ground states (Fujimoto et al. 1990). This can approximately be reached if the evolution of the plasma parameters (like electron density and temperature) is sufficiently slow, such that the plasma evolves through quasi-equilibrium, near-LTE states (Cristoforetti et al. 2010). In this case the change in plasma parameters is sufficiently small compared to the establishment of the excitation (Boltzmann balance) and ionization (Saha balance) equilibrium (Griem 1963).

If a plasma in a quasi stationary complete LTE state is suddenly perturbed by a change of plasma parameters, then the time for re-equilibration of the ground state, respectively the equilibration between the upper and lower state of the resonance line, corresponds to the longest relaxation time (Griem 1963). Since in LTE radiative processes are not important, the relaxation time τ_{rel} is determined by the slowest collisional process. The resulting relaxation times can sometimes be on the order of the changing plasma conditions and break complete LTE conditions. If these considerations are restricted to excited levels only, then the timescales reduce significantly and the relaxation times are likely to be much shorter than the macroscopic change of the plasma parameters and will only infrequently cause deviations from partial LTE (Griem 1963).

To evolve at least in quasi-equilibrium, near-LTE state the plasma must fulfil (Cristoforetti et al. 2010)

$$\frac{n_e(t+\tau_{\text{rel}}) - n_e(t)}{n_e(t)} \ll 1, \qquad \text{and} \qquad \frac{T_e(t+\tau_{\text{rel}}) - T_e(t)}{T_e(t)} \ll 1. \tag{2.13}$$

Where n_e is the electron density, T_e the electron temperature, t the time and τ_{rel} the relaxation time to reach equilibrium.

Along the work of Griem 1963 and Drawin 1969, Cristoforetti et al. 2010 establishes an approximation for the relaxation time (in seconds) as

$$\tau_{rel} \approx \frac{6.3 \times 10^4}{n_e f_{12} P} \Delta E_{21} \sqrt{\frac{k_B T}{1\,\text{eV}}} \exp\left(\frac{\Delta E_{21}}{k_B T}\right), \tag{2.14}$$

with the oscillator strength f_{12}, the Gaunt factor P and the energy difference between the first excited level and the ground state ΔE_{21} (compare also Mendys et al. 2014). The temperature $k_B T$ and ΔE_{21} are in eV and n_e is in cm^{-3}. This approximation is valid for a completely ionized plasma and for partial ionization it must be multiplied with $n_z/(n_z + n_{z-1})$ where n_z is the number density of the ionization stage z (Cristoforetti et al. 2010). This expression was derived for hydrogen-like atoms and might not be valid for others.

For complete ionization ($n_z/(n_z + n_{z-1}) = 1$) of an hydrogen plasma this is at 1.5 eV and a electron density of 1×10^{17} cm^{-3} for example $\tau_{\text{rel}} \approx 0.2$ µs. For lower temperatures and densities the requirements quickly increase and prevent LTE from being established. For example at $T_e = 1$ eV, $n_e = 1 \times 10^{16}$ cm^{-3} and ionization ratios of 0.1 the requirement would already be $\tau_{\text{rel}} \approx 4$ µs for complete LTE.

2.4.3 Criteria for pLTE

If the previous criteria are not met for the first resonance transition, then criteria for pLTE can be checked to find the level where the LTE assumption starts to be violated. To find the level where the boundary between LTE and pLTE states occurs, we need to consider the radiative decay rates and the electronic de-/excitation rates. Griem 1963 defined a condition for a level with principal quantum number n, sometimes also called the thermal limit n_{th} (Kunze 2009, p. 141), to be in LTE with the higher energy levels and the continuum. In this criterion the collisional rate to levels higher than n_{th} should at least be 10 times larger than the radiative decay rate from n_{th}:

$$\sum_{u>n_{th}} n_e X(n_{th} \to u) \geq 10 \sum_{l<n_{th}} A(n_{th} \to l), \tag{2.15}$$

where X is the collisional rate for excitation and A the rate coefficient fro radiative de-excitation.

There are a number of relations to estimate the minimum electron density needed to establish pLTE at n_{th}, Griem 1963 introduced a relation for pLTE conditions as

$$\begin{aligned} \frac{n_e}{\text{m}^{-3}} &\geq 7.4 \times 10^{24} \frac{z^7}{n_{\text{th}}^{17/2}} \left(\frac{k_B T_e}{E^i_{H^z}} \right)^{1/2} \\ &= 7.4 \times 10^{24} \frac{z^7}{n_{\text{th}}^{17/2}} \left(\frac{k_B T_e}{z^2 E^i_H} \right)^{1/2} \\ &= 2 \times 10^{24} \frac{z^6}{n_{\text{th}}^{17/2}} \left(\frac{k_B T_e}{\text{eV}} \right)^{1/2}, \end{aligned} \tag{2.16}$$

where $E^i_H = 13.5984$ eV (Kramida et al. 2020) is the ionization energy of hydrogen and $E^i_{H^z} = z^2 E^i_H$ (Belmonte et al. 2015). Here z is the effective charge seen by the bound (excited) electron, which is $z = 1$ for neutrals and $z = 2$ for singly ionized ions and correspondingly for higher ionization. This relation is strictly only valid for ionized helium, but should also be approximately valid for higher excited states of other light atoms or ions, since most of these higher excited levels can be approximated by the corresponding hydrogenic levels (Griem 1963). However, Griem 1997, p. 215 finds that this can be crude for neutrals ($z = 1$).

Reordering of Eq. (2.16) gives the minimum level in equilibrium as[1]

$$n_{\text{th}} \geq 723 z^{12/17} \left(\frac{n_e}{\text{m}^{-3}}\right)^{-2/17} \left(\frac{k_B T_e}{\text{eV}}\right)^{1/17}. \tag{2.17}$$

Kunze 2009 gives also a relation for the minimum electron density of hydrogenic ions (one valence electron) for levels with quantum number n_{th} as

$$\frac{n_e}{\text{m}^{-3}} \geq 1.1 \times 10^{24} \frac{z^6}{n_{\text{th}}^{17/2}} \left(\frac{k_B T_e}{\text{eV}}\right)^{1/2}. \tag{2.18}$$

This relation was derived for for hydrogenic ions, for which the charge z equals the nuclear charge of the ion. To approximate non-hydrogenic ions the effective charge seen by the electron, which is again $z = 1$ for neutrals, $z = 2$ for singly ionized ions etc. and the effective quantum number must be used (Kunze 2009, p. 122).

Reordering of Eq. (2.18) gives the minimum level in equilibrium as:

$$n_{\text{th}} \geq 670 z^{12/17} \left(\frac{n_e}{\text{m}^{-3}}\right)^{-2/17} \left(\frac{k_B T_e}{\text{eV}}\right)^{1/17}. \tag{2.19}$$

Other estimates by van der Mullen 1990, p. 184 are suggested to be more appropriate, especially for hydrogen (Griem 1997, p. 215):

$$n_e \geq 1.32 \times 10^{24} \frac{1}{n_{\text{th}}^9} \frac{T_e z^{-2} + 2}{(T_e z^{-2})^{0.5}} \frac{3 \ln(n_{\text{th}}) - \zeta}{\ln(2/\epsilon_{\text{th}} + 1.3)(1 + \epsilon_{\text{th}}/4)} z^7. \tag{2.20}$$

or

$$n_{\text{th}} \geq \left(1.32 \times 10^{24} \frac{1}{n_e z^{-7}} \frac{T_e z^{-2} + 2}{(T_e z^{-2})^{1/2}} \frac{3 \ln(n_{\text{th}}) - \zeta}{\ln(2/\epsilon_{\text{th}} + 1.3)(1 + \epsilon_{\text{th}}/4)}\right)^{1/9} \tag{2.21}$$

It holds $\epsilon_{\text{th}} = |E_{\text{th}}|/k_B T_e$ (van der Mullen 1990, p. 148) with the ionization potential E_{th} (kinetic energy of bound electron) of level n_{th} and $\zeta = 0.25$ for optically thin conditions, respectively $\zeta = 1.84$ if only resonant hydrogen Lyman transitions are considered to be optically thick. This relation was derived for hydrogen and was generalized for hydrogenic ions, for which the charge z again equals the nuclear charge of the ion. It should also be mentioned that in the derivation of Eq. (2.20) (van der Mullen 1990, Eq. 7.21) the factor 10, which was employed in the derivation of Griem 1963 and the other equations (see Eq. (2.15)), was not used. For comparability the result of van der Mullen 1990 has been scaled with 10.

Fujimoto et al. 1990 established, based on calculations with a collisional radiative model for hydrogenic ions, further criteria to judge in which conditions pLTE can exist. They pointed out, that already by earlier workers (T. Fujimoto 1973; Engelhardt 1973), it was found that there can be plasma conditions where the criterion introduced in Eq. (2.16) holds, but partial

[1] Kunze 2009 gives this factor to 840, but this neglects the ionization energy of hydrogen which was on contrary included in his form of Eq. (2.19).

LTE is not reached. They proposed additional criteria based on their collisional radiative model calculations and found it instructive to divide plasmas into three categories.

For their categorization (introduced in T. Fujimoto 1979 and subsequent papers) they employed the quasi steady state solution and identified two extreme cases of stationary solutions, namely the purely recombining and purely ionizing plasma. This categorization builds on the population of the atomic and ionic ground states, which can be considered as the entry levels to the excitation space between ionic and atomic ground state (see also Appendix A.4; Graef 2012). These ground levels can therefore be considered as the principal density reservoirs for the internal excited levels. In the purely recombining plasma, the atomic ground state density is set to zero and the entry level to the excitation space is solely the ionic ground state. This neglects contributions from the atomic ground state entirely. The other extreme is the purely ionizing plasma for which the contributions out of the ground level dominate such that it is the only entry to the excitation space.

With this definition of ionizing and recombining plasmas it is possible to describe any plasma as the superposition of an ionizing and recombining part. It follows that the superposition of equal parts of ionizing and recombining contributions leads to an ionization and recombination equilibrium which is called steady state ionisation balance. Thus, we have three different (extreme) categories of plasmas, the recombining, ionization balance and ionizing plasma (T. Fujimoto 1979; Fujimoto et al. 1990).

Based on this distinction they gave a criterion for each category, but we will not treat the ionizing plasma criterion because this will hardly applicable in the plasmas in this study. For a plasma in ionization balance this criterion is

$$\frac{n_e}{\mathrm{m}^{-3}} \geq 3.66 \times 10^{23} \frac{z^{5.5}}{n_{\mathrm{th}}^{7.52}} \left(T_e\right)^{0.752} . \tag{2.22}$$

or

$$n_{\mathrm{th}} \geq 1.36 \times 10^{3} z^{0.73} \left(\frac{n_e}{\mathrm{m}^{-3}}\right)^{-0.133} \left(\frac{k_B T_e}{1\mathrm{eV}}\right)^{0.1} \tag{2.23}$$

For a recombining plasma two relations must simultaneously hold, one relation for the minimal electron temperature

$$\frac{k_B T_e}{\mathrm{eV}} \geq \left(\frac{2.618 z}{n_{\mathrm{th}}}\right)^2 \tag{2.24}$$

or

$$n_{\mathrm{th}} \geq 2.618 \left(z^2 \frac{\mathrm{eV}}{k_B T_e}\right)^{0.5} \tag{2.25}$$

and another for the electron density

$$\frac{n_e}{\mathrm{m}^{-3}} \geq 2.04 \times 10^{22} z^7 \left(n_{\mathrm{th}} - 2.109 \left(z^2 \frac{\mathrm{eV}}{k_B T_e}\right)^{0.43}\right)^{-6.67} \tag{2.26}$$

or

$$n_{\text{th}} \geq 2.109 \left(z^2 \frac{\text{eV}}{k_B T_e} \right)^{0.43} + 2.22 \times 10^3 \left(z^7 \frac{\text{m}^{-3}}{n_e} \right)^{0.15} \tag{2.27}$$

As these equations were also derived for hydrogen like ions, also here the charge z equals the nuclear charge. Low lying levels below the minimum temperature will never be in pLTE because electrons have not enough collisional energy to excite levels and de-excitation dominates (Fujimoto et al. 1990).

In the derivation of those equations (Eqs. (2.23) to (2.26)) a statistical distribution of different (l), (j) and core states was assumed and for non-hydrogen-like atoms it is possible that this underestimates the electron density. It is nevertheless expected that this approximation is valid above the electron density for partial LTE expressed in Eqs. (2.16) and (2.17). The relations for recombining plasmas Eqs. (2.24) to (2.27) are expected to be approximately valid also for non-hydrogen-like atoms.

The selection of criteria presented here demonstrates that the criteria for pLTE conditions are not unambiguous. The criteria by Griem 1963; Kunze 2009 and Fujimoto et al. 1990 for pLTE in ionization balance show a decreasing required electron density for decreasing temperatures, while the criterion by van der Mullen 1990 shows the opposite case (see also Figs. 4.5 and 5.5). According to Hey et al. 1999 only the latter case can intuitively describe the physical situation. An increasing electron density requirement with lower temperature is also in agreement with Eq. (2.12). Hey et al. 1999 raised some doubts about the criteria introduced by Griem 1963; Fujimoto et al. 1990 and van der Mullen 1990, especially in the low temperature region and proposed another criterion. This criterion requires additional parameters and could not be shown, but allows a comparison and discussion based on the publication. For hydrogen it yields at temperatures $k_B T_e < 0.5$eV values that are one to two orders of magnitude larger than those by the older criteria but at higher temperatures this criterion still seems to approach the older criteria. It should also be mentioned that the comparison between the criteria of Hey et al. 1999 and van der Mullen 1990 seems to be inaccurate since Hey et al. 1999 did not correct for the factor 10 in the criterion of van der Mullen 1990 as mentioned previously. With this in mind the criteria by van der Mullen 1990 and Hey et al. 1999 do not disagree fundamentally any more. At temperatures < 0.5 eV the criterion of Hey et al. 1999 yields still higher densities but at higher temperatures they seem to agree approximately. Although we will not use the criterion of Hey et al. 1999, this discussion increases the confidence in the criterion of van der Mullen 1990 and establishes this as possibly the most accurate criteria among the criteria of Griem 1963; Kunze 2009 and Fujimoto et al. 1990.

Hey et al. 1999 also emphasized that the criteria derived previously are sometimes applied for neutral atoms although they had been derived for hydrogen like ions. It is difficult to find

Table 2.1: The conditions for LTE and pLTE as derived by different authors and the species they were originally derived for.

Authors	Derived for	Type of Condition
Griem 1963	hydrogen-like ions	LTE / pLTE
Hey 1976	neutrals / ions	LTE
Fujimoto et al. 1990	neutral hydrogen / hydrogen-like ions	pLTE
van der Mullen 1990	neutral hydrogen / hydrogen-like ions	pLTE
Kunze 2009	neutral hydrogen / hydrogen-like ions	LTE / pLTE

a pLTE criterion for neutral, non hydrogen-like plasmas as an argon plasma, only Fujimoto et al. 1990 suggested that their criterion for recombining plasmas should also be valid for other atoms or ions that are not hydrogen-like. The previously presented criteria are also summarized in Table 2.1 together with the species they were derived for and show that there is no pLTE condition which was derived for an neutral argon plasma.

As an approximation to use these criteria for neutral atoms as well, the approach of the effective charge seen by the excited (bound electron) and the effective quantum number is sometimes used (Aparicio et al. 1999; Lao et al. 2002). In the case of neutrals, the excited electron is approximated to only see the charge $z = 1$ of the (shielded) nuclear core charge. For high-lying states with different quantum numbers the energy structure can also be well approximated by an effective quantum number deduced from hydrogen (Fujimoto et al. 1990). This effective quantum number can be calculated according to Aparicio et al. 1999 by

$$n_{\text{eff}} = z\sqrt{\frac{1\text{Ry}}{E_{\text{ioniz}}}}, \tag{2.28}$$

where $1\text{Ry} = hcR_\infty = 13.605\,\text{eV}$ (Kramida et al. 2020) is the Rydberg energy and z the effective charge seen by the electron (e.g. $z = 1$ for neutrals and $z = 2$ for singly ionized ions).

Another point raised by Hey et al. 1999 is also that high atomic densities compared to relatively low electron densities can also cause deviations from pLTE although the electron density would satisfy pLTE. The most reliable results to asses whether LTE or pLTE is present is however to construct a collisional radiative model for the plasma under investigation (Kunze 2009, p. 141) and use this for the plasma parameters under investigation.

2.4.4 Criteria for Steady State in pLTE

As for complete LTE, the plasma evolution could also be too fast to establish pLTE for a certain energy level p. Drawin 1969 gave an expression for the relaxation time τ of an excited level p

for partial LTE with:

$$\tau_{z-1,p} \simeq \frac{4.6 \times 10^7}{n_e p^4} z^3 \left(\frac{k_B T_e}{E_1^H}\right)^{1/2} \times \begin{cases} \psi_1(x)^{-1} \text{ for neutrals} \\ \psi_2(x)^{-1} \text{ for ions} \end{cases}, \tag{2.29}$$

with $x = 2z^2 H_1^H / k_B T_e p^3$, the charge z (for neutrals $z = 1$, for singly ionized ions $z = 1$, etc.), n_e the electron density in cm^{-3}, E_1^H the ionization energy of hydrogen and the quantum mechanical correction functions $\psi_1(x)$, $\psi_2(x)$ defined by Drawin 1969. Note that this formula does not need to be multiplied with the ionization fraction as Eq. (2.14) (Drawin 1969; Griem 1963).

Concerning the ionizing an recombining plasma criteria by Fujimoto et al. 1990, Sawada et al. 1994 found that the response time of the system of excited levels is also given by the largest relaxation time among the levels, such that Eq. (2.29) should also applicable for them.

2.5 Collisional Radiative Models

If the electron density is high enough, the concept of LTE and pLTE allows a simplified treatment of the plasma, also if the electron density becomes very low, which will not be the case at our working points, the so called corona equilibrium (Kunze 2009, p. 142) with simple relations can simplify the treatment. The corona equilibrium is valid if the electron density is low enough, such that de-excitation processes are governed by radiative decay and excitations are governed by collisional processes only.

Collisional radiative models (CRMs) close the gap between LTE and corona equilibrium by accounting for the different processes in the plasma that populate and depopulate the energy levels. These models return for high electron densities the populations according to the Boltzmann distribution, in steady state also the Saha-Eggert equation and for low electron densities the corona equilibrium (Kunze 2009, p. 147), thus they are a generalized models.

The first CRMs were developed for hydrogen and hydrogen-like ions by Bates et al. 1962 and originate from astrophysics and plasma spectroscopy. The concept and framework of those models was more recently and in more detail described by Graef 2012. The discussion of CRMs will be based on his work, but only a general introduction to the concept is shown in this section, further detail can be found in Appendix A.

2.5.1 General Remarks

Graef 2012 distinguishes between three different main features that describe the processes between the species in a plasmas, where a species is any group of particles with the same unique chemical property (this results in every excited level of an atom being its own species):

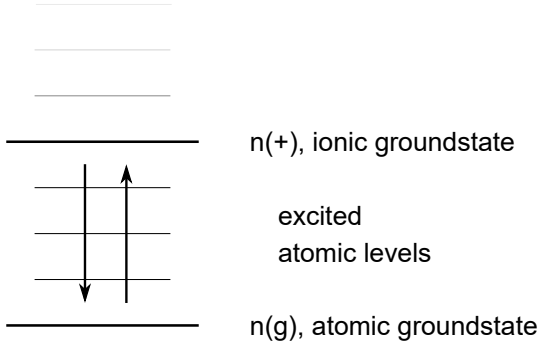

Figure 2.2: Sketch of the levels included in a CRM. The atomic and ionic ground states serve as principal density reservoirs for the excited levels in between and are usually much higher populated than those. Processes that traverse the excited levels connect the ionic and atomic ground state.

- *Configuration:* The term configuration is used to describe the interaction of the plasma with its environment. This includes aspects as the interaction with the geometry, the energy coupling or the boundary conditions.

- *Transport:* The term transport is used to describe the transport of species, momentum and energy inside the plasma and between its direct surroundings. Transport is the result of gradients between sources and sinks within a plasma, e.g. a density gradient between two species that is in turn equilibrated by transport.

- *Chemistry:* The term chemistry is used to describe the processes that produce and destroy species in a plasma which then can give rise to transport processes.

Those categories are not clearly distinct from each other and there is an interplay between them - for example the chemistry can create gradients, which in turn cause transport.

In a plasma there can be a large number of species and it is usually not practical to consider them all. The modelling is therefore reduced to include only the relevant species and processes. In a CRM the distribution of the population of atomic states (atomic state distribution function (ASDF)) is often governed by two main contributors; the atomic ground state and the ionic ground state. These two ground states are interconnected with electron collisions and radiative transitions that usually also involve excited levels in between (see Fig. 2.2). The excited levels are usually less populated than the ground states (compare also Section 2.1.1).

To build up a CRM all the different processes must be included in a rate equation (Eq. (2.1)) for each level. By using Eq. (2.1) again, we can identify how the density of an atomic state relates to the populating and depopulating processes:

$$\underbrace{\frac{\mathrm{d}n_z(p)}{\mathrm{d}t}}_{} + \underbrace{\Delta \cdot \Gamma_z(p)}_{} = \underbrace{R_z(\rightarrow p) - R_z(p \rightarrow)}_{}$$

$$\text{Accumulation} + \text{Efflux} = \text{Chemistry Production} \tag{2.30}$$

Here 'Accumulation' is the accumulated density, 'Efflux' the efflux (by configuration and transport) and 'Chemistry Production' the density produced by chemistry processes.

The transport and configurational aspects of a plasma are only described in a simplified form in CRMs and it is also not the task of a CRM to model these aspects. The application of a CRM rather is to model the 'chemistry' in a plasma. In this work the CRM is also restricted to the atomic system with atomic excitations only, excitations of ionic levels are not considered. In this context the atomic ground state and the ionic ground state can be denoted as the low energy and high energy entry to the excitation space (excited levels in between), respectively. Because the density of the entry levels is much higher and quasi stationary with respect to the excited levels (Section 2.1.1), the entry levels determine the population density of the internal levels through the excitation flow by collisional and radiative processes. A simplified example of a rate balance equation that only includes electronic processes and spontaneous emission is:

$$\underbrace{\frac{\partial n(p)}{\partial t}}_{\text{accumulation}} = \underbrace{n_e n_g K(g,p)}_{\text{electron excitation from gs}} - \underbrace{n(p) n_e K(p,g)}_{\text{electron de-excitation to gs}} \tag{2.31a}$$

$$+ \underbrace{\sum_q n_e n(q) K(q,p)}_{\text{electron de-/excitation from q}} - \underbrace{n(p) n_e \sum_q K(p,q)}_{\text{electron de-/excitation to q}} \tag{2.31b}$$

$$+ \underbrace{n_e^2 n_+ K(+,p)}_{\text{two electron recombination}} - \underbrace{n(p) n_e K(p,+)}_{\text{electron induced ionization}} \tag{2.31c}$$

$$+ \underbrace{n(u) \sum_u A(u,p)}_{\text{spont. emission cascade}} - \underbrace{n(p) \sum_l A(p,l)}_{\text{spont. emission}}, \tag{2.31d}$$

where n_e, n_g, n_+, $n(p)$ and $n(u)$ are the number densities of electrons, ground state atoms, ground state ions of the first ionization stage, level p and level u above p. $K(q,p)$ is the rate coefficient for electron induced collisions from q to p and $A(p,l)$ the Einstein coefficient for spontaneous emission from p to a lower level l. The rate coefficients K are temperature depended and introduce a temperature dependence in these balance equations. To construct a CRM the, left side of Eq. (2.31) is, according to QSSS (Section 2.1.1), usually set to zero for excited levels and a rate balance equation set up for every included level. This results in a set of coupled rate balance equations which have to be solved simultaneously (Appendix A) to determine electron temperature and density (Section 4.3).

2.6 Emission Coefficient

The transition from theoretical concepts to experimentally accessible plasma parameters can be facilitated by the radiation that is naturally produced in plasmas by spontaneous emission.

Spontaneous emission is the result of a electron transition from a higher to a lower energy level $u \rightarrow l$ with probability A_{ul}. The intensity of this emission correlates with the density of the upper level u and is measured with the line emission coefficient ϵ_{ul}. For a transition $u \rightarrow l$ this is in units of $\mathrm{Wm^{-3}sr^{-1}}$ (Fantz 2006; Kunze 2009)

$$\epsilon_{ul} = n(u) A_{ul} \frac{hc}{4\pi\lambda_{ul}}. \tag{2.32}$$

Where $n(u)$ is the density of the upper level, h the Planck constant, c the speed of light and λ_{ul} the wavelength of the emitted radiation. This coefficient shows the correlation of the line intensity with the population density of an upper level $n(u)$.

2.6.1 Self-Absorption of Radiation

Radiation that is emitted due to a transition $u \rightarrow l$ can be reabsorbed from an atom in state l and cause the re-excitation $l \rightarrow u$. This process is described as self-absorption or radiation trapping. As briefly mentioned in Section 2.2.2, absorption and stimulated emission are non-local processes which implies that radiation is produced at one location in the plasma and interacts with atoms at another location. This non-local nature makes an exact treatment in the modelling difficult, but as an approximation the spatially independent 'escape factor' θ_{ul}, introduced by Holstein 1947, is often used:

$$A^*(u,l) = \theta_{ul} A(u,l) \tag{2.33}$$

This factor θ_{ul} converts the spontaneous emission probability to an effective probability to approximatively include re-absorption. The escape factor is generally defined as (X.-M. Zhu et al. 2016)

$$\theta_{ul} = \frac{S_{ul} - S'_{lu}}{S_{ul}}, \tag{2.34}$$

where S_{ul} is the rate of spontaneous emission and S'_{lu} the rate of absorption (see also Graef 2012, p. 40). A simple approximation for this escape factor for a uniform distribution of emitting and absorbing atoms was introduced by Mewe 1967 as

$$\theta_{ul}(\tau) \approx \frac{2 - \exp(-\tau/1000)}{1 + \tau}, \tag{2.35}$$

where τ is the optical depth. The dimensionless optical depth τ is a measure for the optical thickness of a medium and is for a purely Gaussian/Doppler broadened line shape given by (Boffard et al. 2009):

$$\tau = k_{ul} r \tag{2.36}$$

$$k_{ul} = \frac{\lambda_{ul}^3}{8\pi^{3/2}} \frac{g_u}{g_l} n(l) A_{ul} \sqrt{\frac{M}{2 k_B T_g}}. \tag{2.37}$$

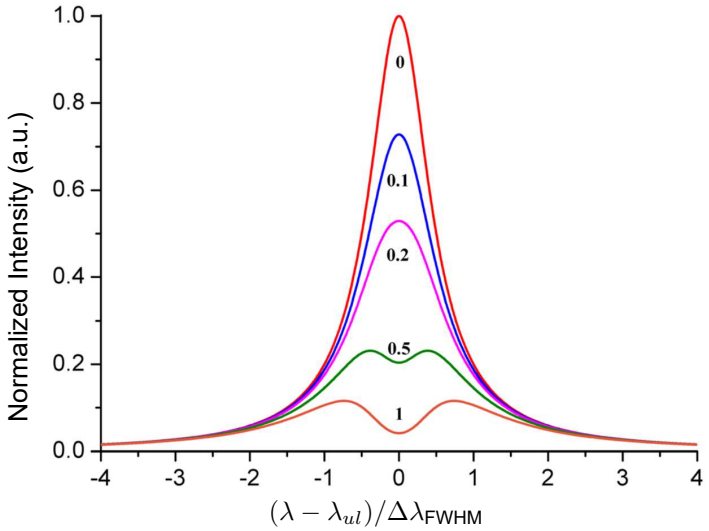

Figure 2.3: Self absorption broadening of a Lorentzian line profile at different optical depths taken from Xiong et al. 2011. The optical depths τ are indicated above the respective profiles and the x-axis is normalized to the FWHM of $\Delta\lambda_{\mathrm{FWHM}} = 0.2\,\mathrm{nm}$.

With the absorption coefficient k_{ul}, the characteristic scale length of the plasma r (the distance the light travels in average in the plasma), the density of the lower level $n(l)$, the wavelength λ_{ul}, the degeneracies g_u and g_l, the Einstein coefficient A_{ul}, the atomic mass M of the gas species, the Boltzmann constant k_B and the gas temperature T_g. Formulae for more general Voigt-profiles can be more complicated (Durocher-Jean et al. 2019).

The process of self-absorption is stronger if the density of the lower energy level is high and even more efficient if this is the ground state (resonance transitions) (Belmonte et al. 2015). Self absorption is also particularly strong at the line center and weaker at the wings and this leads to an effective line broadening in the observed spectra (Kunze 2009, p. 176). Sharper line profiles with smaller full with half maximum (FWHM) are also more easily affected by self absorption (Xiong et al. 2011) and high values of optical depth τ imply strong self absorption. Sometimes lines with $\tau < 1$ are also considered to be optically thin (Belmonte et al. 2015), but this does not strictly need to apply.

If the plasma is homogenous and the optical depth for the emitted radiation is increasing, then the line intensity approaches the blackbody limit (the Planck equilibrium as introduced in Section 2.2.1) which produces and a flattened top of the peak (Kunze 2009, 176ff). If the local emission and absorption profiles are not identical (in-homogeneous, e.g. cooler regions at the boundary with different Doppler broadenings) this will additionally cause a central dip in the emission profile for large optical depths (Kunze 2009, p. 177). A self-absorption broadened Lorentzian line profile for an in-homogeneous plasma is shown in Fig. 2.3 for different optical depths.

If self-absorption of radiation along a line of sight is present in the plasma and can be ap-

proximated with the escape factor θ_{ul}, Eq. (2.32) changes to (García et al. 2000)

$$\epsilon_{ul} = n(u)\theta_{ul}A_{ul}\frac{hc}{4\pi\lambda_{ul}}. \tag{2.38}$$

Equations (2.32) and (2.38) relate population densities of the upper levels to the measured line intensities. Since population densities depend on parameters as electron density and temperature (temperature dependence of the reaction rate of the involved processes) also the measured line emission depends on electron temperature and density.

2.7 Boltzmann Plot

By using the line emission coefficient Eq. (2.32) and by assuming LTE (Section 2.2.2) it is possible to relate the plasma emission to the electron temperature with the so called Boltzmann plot method. In LTE $n(u)$ follows a Boltzmann distribution and therefore the relative population of the energy state u of species j is (Piel 2017, p. 32; Zhang et al. 2019)

$$\frac{n(u)}{N_j} = \frac{g(u)}{Z_j}\exp\left[\frac{-E_u}{k_BT}\right], \tag{2.39}$$

with the partition function

$$Z_j = \sum_i g(i)\exp\left[\frac{-E_i}{k_BT}\right]. \tag{2.40}$$

Where $N_j = \sum_i n(i)$ is the total number density of atoms or the respective ion j and i runs over all internal state densities $n(i)$. Further, E_u is the energy of the upper level and $g(i)$ the degeneracy of level i. Inserting the energy level density $n(u)$ from Eq. (2.39) into Eq. (2.32) results in

$$\epsilon_{ul} = \frac{g(u)N_j}{Z_j}\exp\left[\frac{-E_u}{k_BT}\right]A_{ul}\frac{hc}{4\pi\lambda_{ul}}, \tag{2.41}$$

The total number density N_j in Eq. (2.41) can also be expressed in pressure P and concentration $C_j = N_j/N_{\text{tot}}$ of atom / ion j (where $\sum_j C_j = 1$) as

$$N_j = C_j\frac{P}{k_BT}, \tag{2.42}$$

where

$$P = \sum_j N_j k_B T_j \overset{\text{LTE}}{=} N_{\text{tot}} k_B T_e. \tag{2.43}$$

We rewrite Eq. (2.39) with Eq. (2.42) and introduce a factor F that accounts for losses through the optical setup (Zhang et al. 2019) and obtain an relative emission coefficient $\bar{\epsilon}_{ul}$

$$\bar{\epsilon}_{ul} = F\epsilon_{ul} = F\frac{g(u)}{Z_j}\frac{C_jP}{k_BT}\exp\left[\frac{-E_u}{k_BT}\right]A_{ul}\frac{hc}{4\pi\lambda_{ul}}. \tag{2.44}$$

After reordering and taking the logarithm this equation can be written as

$$\ln\left(\frac{\bar{\epsilon}_{ul}\lambda_{ul}}{A_{ul}g_u}\right) = -\frac{E_u}{k_B T} + \ln\underbrace{\left(\frac{hcFPC_j}{4\pi Z_j k_B T}\right)}_{const.}. \tag{2.45}$$

The factor in the logarithm on the right hand side is a constant for all emission lines within a species (W. L. Wiese 1991). This equation can be used for the Boltzmann plot method (Griem 1997; Zalach et al. 2013) to determine the electron temperature if multiple emission lines are available (see Section 3.5). The temperature can be obtained if the left hand side of Eq. (2.45) is plotted versus the energy E_u of the upper level.

Chapter 3

Experimental Setup and Methods

3.1 Optical Emission Spectroscopy

As already introduced in Section 2.6, plasma emission from spontaneous radiation can be used to investigate plasma parameters. Plasma spectroscopy, in particular optical emission spectroscopy (OES), is a well established diagnostic technique (Griem 1997) and the setup that is necessary to record an emission spectrum from a plasma is quite simple. Only diagnostic ports, that allow a line of sight through the plasma and a spectroscopic setup to measure emitted light, are necessary. As long as only emitted radiation is observed, this method is non-invasive and does not affect the plasma properties like the insertion of Langmuir probes for temperature measurements would do. The spectra are easily obtained but the interpretation, especially for non-equilibrium plasmas, can be complicated (Fantz 2006). Due to its non-invasive character and the simple setup, OES was the method of choice to investigate the electron temperature.

3.2 Experimental Setup

The experiments were conducted with two different experimental setups, one setup in a diagnostics laboratory and a second setup at the FLASHForward experiment (D'Arcy et al. 2019).

3.2.1 Diagnostics Laboratory Setup

The structure which was employed to create a plasma was a discharge capillary (Fig. 3.1) that was mounted into a vacuum chamber in which an ambient pressure of around 1×10^{-6} mbar was established. This capillary was filled either with argon or hydrogen such that the gas continuously flew through the plasma cell and was subsequently evacuated from the chamber. The plasma itself was created using a high voltage discharge current between the electrodes and an optical setup was used to measure the its light emission on a CCD intensified camera.

The discharge capillary was milled from two sapphire slabs that contain one half of the central channel each and were pressed together to form the main plasma channel. The central channel in this setup had a diameter of 1.5 mm and a length of 33 mm. The two gas inlets, through which the gas can be filled with an adjustable pressure into the discharge volume, are

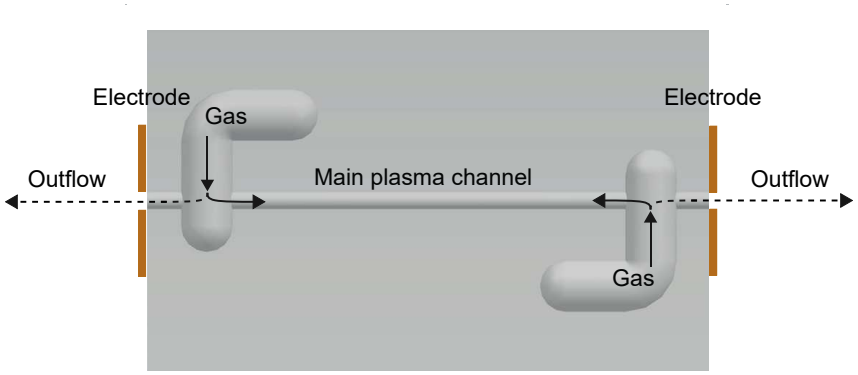

Figure 3.1: Schematic drawing of the discharge capillary adapted from Garland et al. 2021. The central channel is cylindrical, has a diameter of 1.5 mm and is connected with gas inlets at each side. At each extremity of the capillary copper electrodes (brown) with an opening of the same diameter are placed to deliver the high-voltage current pulse. Gas outflow takes place through to open ends of the capillary.

also shown in Fig. 3.1. The gas pressure is measured in a buffer volume but the actual pressure in the capillary is significantly, at least 50 % lower than the buffer pressure. At each side of the sapphire block one copper electrode with an opening diameter equal to the main plasma channel provides the contact for the high voltage current. Sapphire as a material provides a hard-surface environment to confine the plasma and due to its transparency also the possibility to make spectroscopic measurements transversely to the main channel (Garland et al. 2021).

The plasma was created using a pulse forming network (PFN) that delivers at a circuit matching impedance of 50 Ω, a 400 ns pseudo flat-top current pulse of up to 500 A. The light emanating from this resulting plasma was propagated through a window out of the vacuum chamber to the spectrometer. In the diagnostics laboratory an imaging system with two lenses was set up which allowed to make spatially resolved measurements. The imaging system was set up such that light was collected from a depth of field of ± 100 µm from the central part of the capillary. A schematic drawing of the setup is shown in Fig. 3.2.

In this setup, a Princeton Instruments SpectraPro 2150i spectrometer together with an Andor iStar DH334T intensified photo-multiplier CCD (iCCD) camera was used. This spectrometer had a grating of 1200 lines/mm and a spectral range of around 50 nm at 500 nm. The slit of the spectrometer was opened to 100 µm and aligned horizontally (corresponding to Fig. 3.1), such that a longitudinal slice of 100 µm height was observed in the center of the capillary (1:1 imaging system). The camera consisted of a CCD sensor and an upstream photo-cathode intensifier to allow spatial resolved measurements at low signals. The two dimensional CCD array had a resolution of 1024 x 1024 pixel with a pixel size of 13 µm. The horizontal dimension (corresponding to Fig. 3.1) of the CCD was used for spatial resolution such that the 1024 pixel corresponded to a 8 mm long horizontal slice along the center of the capillary. The vertical di-

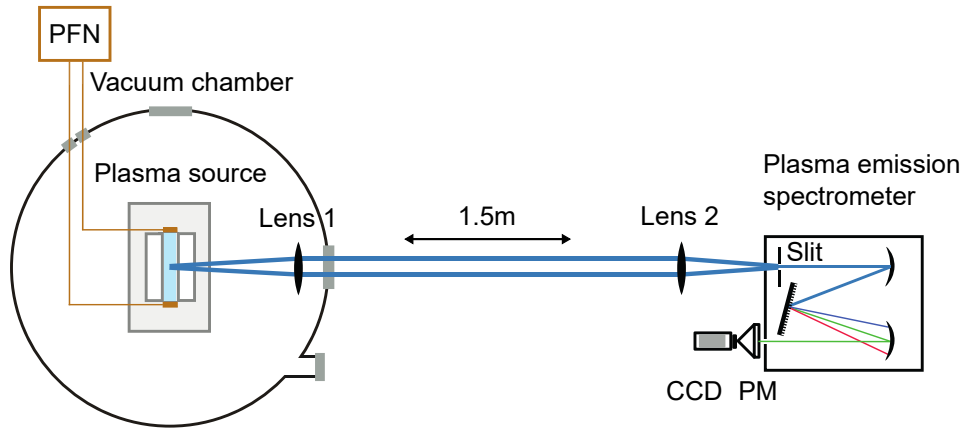

PM: Photo-Multiplier CCD: Charge-Coupled Device PFN: Pulse Forming Network

Figure 3.2: Schematic drawing of the experimental setup of the discharge capillary and the optical diagnostics in the diagnostics laboratory setup (adapted from Garland et al. 2021). The blue lines indicate the collected light which is dispersed on the spectrometer grating and the distance between spectrometer and source is around 1.5 m.

mension of the CCD was used to record the dispersed light after the spectrometer and therefore for spectral resolution. The signal on the CCD is therefore originating from a volume of (length $\times$ width $\times$ depth) 8 mm $\times$ 0.1 mm $\times$ 0.2 mm.

3.2.2 FLASHForward Experiment Setup

The setup at the FLASHForward experiment is shown in Fig. 3.3. This setup was similar to the one in the diagnostics laboratory with three important differences:

- The cell used in this setup had a length of 50 mm instead of 33 mm.
- The spectrometer was a Horiba iHR550 spectrometer with the same Andor iStar camera. The grating of this spectrometer was 1800 lines/mm and allowed a higher spectral resolution on the CCD with a wavelength range of about 10 nm at 600 nm.
- Instead of imaging the plasma emission directly, the light was coupled into a 550 µm diameter, 0.22 NA optical fiber and transported over 30 m to the plasma emission spectrometer. This fiber coupling did not allow spatially resolved measurements and the recorded signal was the average over the whole diameter of 1.5 mm and a capillary length of 7 mm. This fiber coupling reduced the light yield that is recorded with the spectrometer, but allows to obtain an in-situ measurement of the plasma in a plasma wakefield experiment.

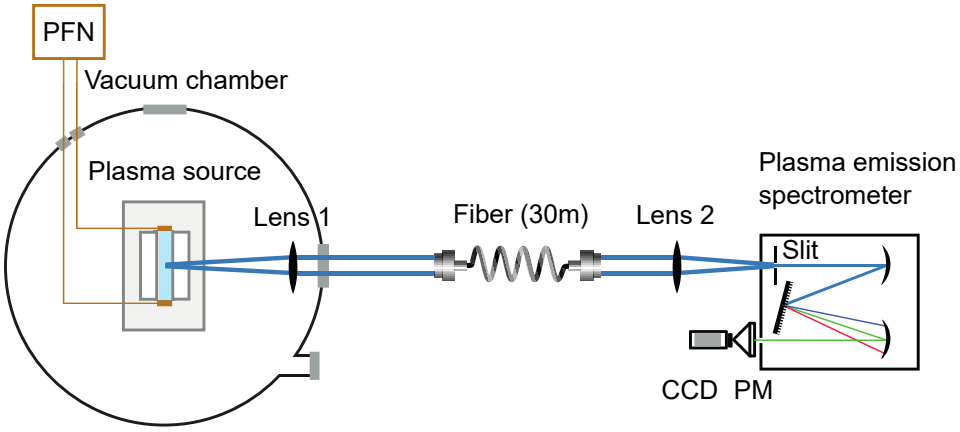

PM: Photo-Multiplier CCD: Charge-Coupled Device PFN: Pulse Forming Network

Figure 3.3: Schematic drawing of the experimental setup of the discharge capillary and the optical diagnostics at the FLASHForward experiment (adapted from Garland et al. 2021). The light from the plasma (blue lines) is collimated and coupled into a 30 m long optical fiber, before it is focused on the spectrometer entry slit.

3.3 OES Measurement Procedures

Multiple emission spectra with different central wavelength settings of the spectrometer were taken for hydrogen and argon to record multiple emission lines in each plasma. The temporal evolution of those lines during and after the discharge pulse was recorded at 21 consecutive time steps starting from the onset of the discharge at 0 µs. The actual average point in time of the measurement corresponds therefore to $t_{\text{step}} + t_{\text{int}}/2$, where t_{step} is the time of the time step and t_{int} the integration time. Since the reproduce-ability of the discharge is reasonably good, every time step was recorded 20 times to obtain sufficient statistics. Additional background images for every setting were taken with lower statistic and while the discharge was off.

3.3.1 Hydrogen

The OES measurements in hydrogen were performed in the FLASHForward experiment setup (Section 3.2.2) at a stable and commonly used working point for plasma acceleration experiments. For this working point the voltage was set to 25 kV at the PFN (Fig. 3.3) and the buffer pressure to 20.4 mbar, which corresponds to approximately 4 mbar cell pressure. The time evolution was recorded during the visible lifetime of the plasma from 0 µs to 4 µs. Due to the reduced light yield through the optical fiber and the low intensity of some lines the integration time was set to 200 ns to balance temporal resolution and line intensity. We took three different spectra to observe all visible hydrogen Balmer lines H-α, H-β and H-γ listed in Table 3.1. This measurement was additionally performed for an integration time of 400 ns.

Table 3.1: The transitions of the Balmer series of Hydrogen (Kramida et al. 2020) which were used in the measurements. Transition levels are in terms of the principal quantum numbers.

Name	Transition wavelength / nm	Transition levels
H-γ	434.047	$5 \rightarrow 2$
H-β	486.135	$4 \rightarrow 2$
H-α	656.279	$3 \rightarrow 2$

Table 3.2: The central wavelength settings at the spectrometer for argon and the corresponding transition wavelength observed at this central wavelength. The transition wavelengths and levels are taken from Kramida et al. 2020 and Boffard et al. 2009 and the transitions are given in Paschen notation.

Central wavelength / nm	Transition wavelength / nm	Transition levels
696.54	696.5431	$2p_2 \rightarrow 1s_5$
706.72	706.7218	$2p_3 \rightarrow 1s_5$
738.40	738.3980	$2p_3 \rightarrow 1s_4$
750.93	750.3869	$2p_1 \rightarrow 1s_2$
“	751.4652	$2p_5 \rightarrow 1s_4$
763.51	763.5106	$2p_6 \rightarrow 1s_5$
801.48	800.6157	$2p_6 \rightarrow 1s_4$
“	801.4786	$2p_8 \rightarrow 1s_5$
811.13	810.3693	$2p_7 \rightarrow 1s_4$
“	811.5311	$2p_9 \rightarrow 1s_5$
842.47	840.8210	$2p_3 \rightarrow 1s_2$
“	842.4648	$2p_8 \rightarrow 1s_4$

3.3.2 Argon

The OES measurements in argon were performed in the diagnostics laboratory setup (Section 3.2.1) at a working point which is also routinely used in the FLASHForward experiment. For this working point the PFN was set to 20 kV and the buffer pressure to 50 mbar, which corresponds to less than 25 mbar cell pressure. The time evolution was recorded from 0 µs to 10 µs because this reflects the time window in which FLASHForward injects beams into the plasma. The integration time could be set to 100 ns because the light yield through the imaging system was larger than through the fibre. In argon the most important groups of lines are the transitions between the $4p \rightarrow 4s$ and $5p \rightarrow 4s$ levels (Wiese et al. 1989). We chose argon emission lines from the the $4p \rightarrow 4s$ transition array only, because $5p \rightarrow 4s$ transitions in the 400 nm range were not resolvable with the equipment used in this setup. In this work, the energy levels of argon will be given in the Paschen notation (see Appendix C) such that and $4p \rightarrow 4s$ transition denote $2p \rightarrow 1s$. These Paschen $2p$ levels are also commonly used to compare CRMs to measurements (X.-M. Zhu et al. 2010a; Gangwar et al. 2012; Evdokimov et al. 2017; Durocher-Jean

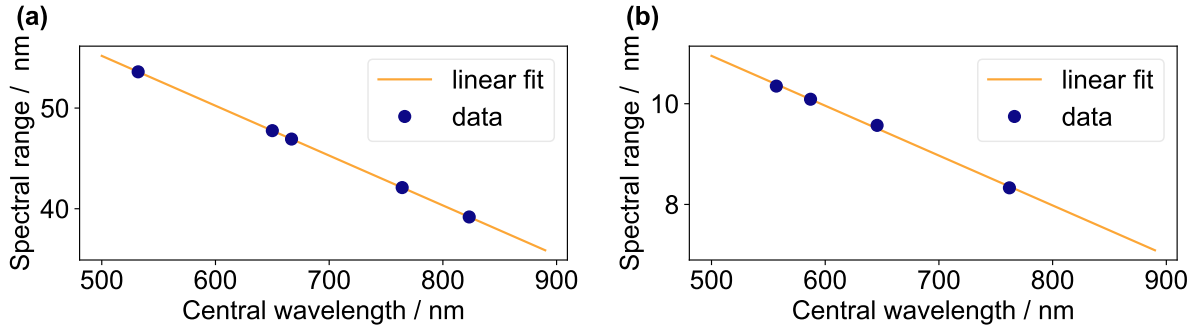

Figure 3.4: **(a)** Spectral range of the CCD sensor with the Princeton Instruments spectrometer versus the central wavelength of the spectrometer. **(b)** Spectral range of the Horiba spectrometer.

et al. 2019). We measured 12 of those $2p \rightarrow 1s$ argon emission lines with 8 different central wavelength settings of the spectrometer as listed in Table 3.2.

3.4 Calibrations

For the temperature measurements in this study it was only necessary to calibrate the intensity in the setup in a relative way since always the relative distribution of the line intensities will be considered (Sections 3.5 and 3.6). Additionally to the intensity calibration also a CCD wavelength range calibration was necessary.

3.4.1 CCD Wavelength Range Calibration

The spectral range that is captured by the sensor varies with the central wavelength (Gaigalas et al. 2009) and was therefore calibrated. For the diagnostics laboratory setup we used two alignment lasers one at 532 nm and another one at 650 nm and additionally a Xenon lamp in which three wavelengths (666.89 nm, 764.2 nm and 823.16 nm) were selected. The spectral range at those central wavelengths of the spectrometer was determined (Appendix B) and is shown in Fig. 3.4a. For the FLASHForward experimental setup the calibration was performed at 4 relevant central wavelengths (557.0 nm, 587.1 nm, 645.63 nm, 762.0 nm) and is shown in Fig. 3.4b. To obtain the best possible overlap the calibration function was also adjusted slightly during the data analysis.

3.4.2 Relative Intensity Calibration

A relative intensity calibration with a calibration light source was necessary for both setups. We used a tungsten halogen lamp HL-3 plus-INT-CAL from Ocean Insight which was calibrated for

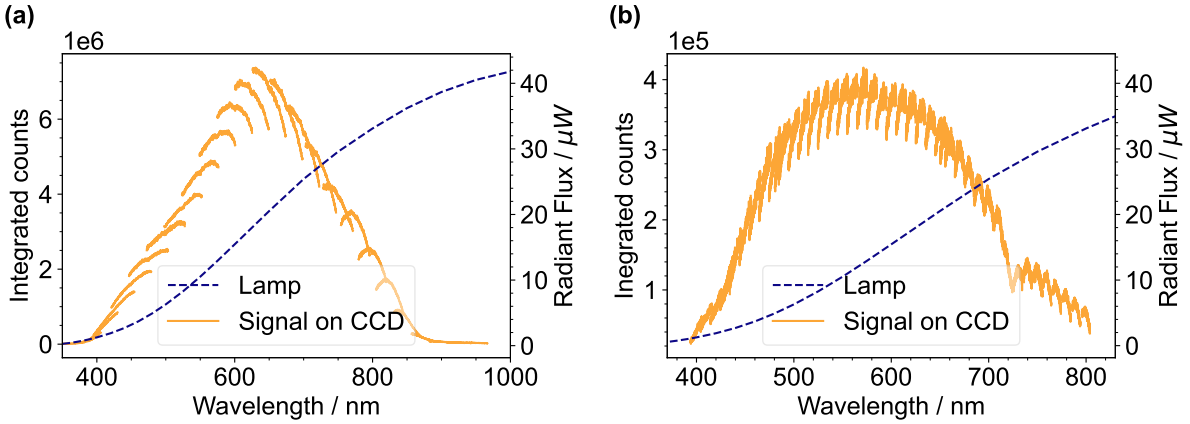

Figure 3.5: Integrated counts on the CCD as a response to the radiant flux of the calibration lamp signal. Every single curve corresponds to a different central wavelength (CWL) of the spectrometer. **(a)** Diagnostics laboratory setup, 25 nm between successive spectra / CWL's (Princeton Instruments spectrometer). **(b)** FLASHForward experiment setup, 10 nm difference between successive spectra / CWL's (Horiba spectrometer).

spectral radiant flux ($\mu W\,nm^{-1}$) in the wavelength range of 350 nm to 1100 nm. For the calibration measurements the calibration lamp was placed behind one slab of the capillary to mimic the location and optical path of the plasma light emission. The calibration was performed for every central wavelength setting that was of interest in the measurements. In the diagnostics laboratory the integration time for these measurements was set to 10 µs and in the FLASHForward experimental setup, to reach adequate signal strengths, to 500 µs.

Additional measurements to investigate the transfer function of the optical setup for a larger wavelength range were also performed and are shown in Fig. 3.5. For these measurements the central wavelength of the spectrometer was shifted in successive steps to cover a large spectral range. Due to the different spectral ranges of the spectrometers the shift was 25 nm in the diagnostics laboratory and 10 nm in the FLASHForward experiment setup.

The individual spectra in Fig. 3.5 do not overlap at their edges and most of them also exhibit a curved shape. This shape depends on the position on the CCD sensor and the central wavelength setting of the spectrometer. It shows qualitatively a lower signal if moving away from the CCD center, but the de-convolution of the shape of the calibration lamp and the optical transfer function and was outside the scope of this study. Because we could not correct for this non-linearity a separate calibration was performed for every central wavelength setting of the spectrometer that was of interest for the temperature measurements.

For the calibration of the measurements first the background was subtracted from the measurements and the calibrations, second the calibrations were de-noised with a Savitzky-Golay filter (Savitzky et al. 1964) as the calibration signal showed some jitter. The calibration was

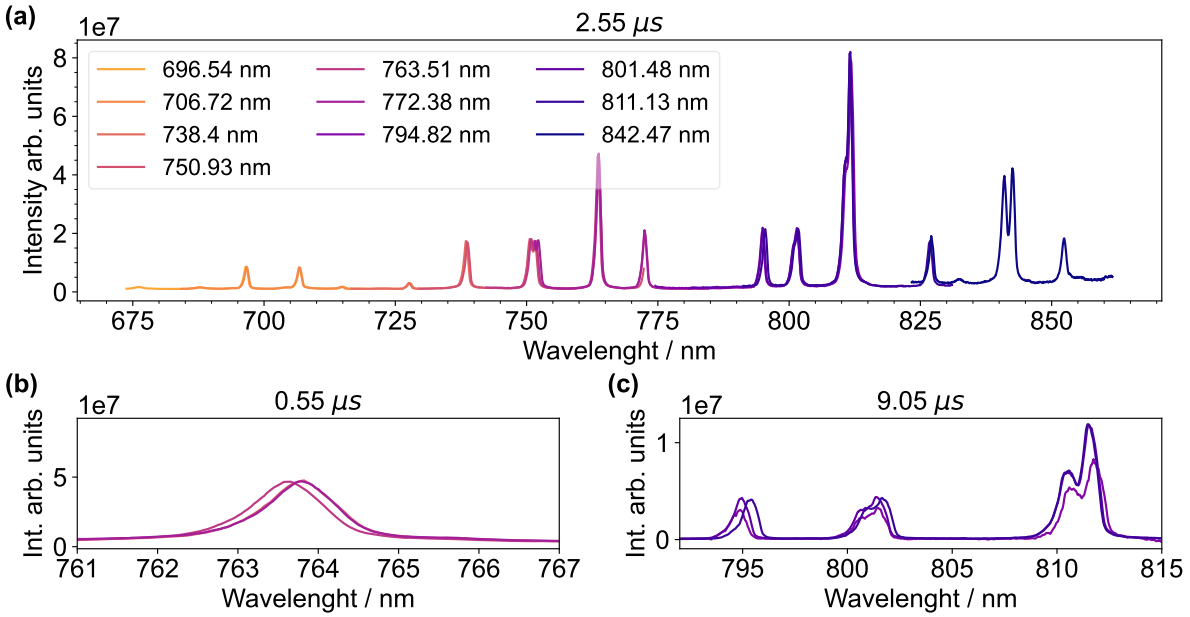

Figure 3.6: **(a)** Wavelength range and intensity calibrated spectrum for all central wavelengths of interest for the temperature measurements at 2.55 µs after the discharge (diagnostics laboratory setup, 20 kV, 50 mbar buffer pressure). Each central wavelength of the spectrometer is indicated in the legend. **(b)** Mismatch of overlapping spectra shortly after the discharge at 0.55 µs. **(c)** Mismatch of overlapping spectra long after the discharge at 9.05 µs.

performed by multiplying the signal of a measurement with the ratio between the intensity of the calibration lamp and the number of counts of the calibration measurement:

$$I_{\text{cal, rel}} = n_{\text{counts, meas}} \frac{I_{\text{lamp}}}{n_{\text{counts, cal}}} \tag{3.1}$$

where $I_{\text{cal, rel}}$ is the relative calibrated intensity, $n_{\text{counts, meas}}$ the integrated counts of the measurement and $n_{\text{counts, cal}}$ the integrated counts of the calibration lamp measurement.

The calibration of the calibration lamp itself was performed with an integrating sphere such that light from all directions of the light source was collected and the total amount of emitted light was measured. Such measurement are independent of the solid angle, but as our setup collected only light from a certain solid angle, the signal of the lamp on the CCD was only proportional to the officially calibrated intensity. The units of I_{lamp} are stated by the manufacturer as $\mu\text{W nm}^{-1}$, but change by taking the solid angle and the illuminated area in our application into account to $\mu\text{Wmm}^{-2}\text{sr}^{-1}\text{nm}^{-1}$ (Blackborow et al. 2011). This is equivalent to the units of the emission coefficient ($\text{Wm}^{-3}\text{sr}^{-1}$) in Eq. (2.32).

With Eq. (3.1) the calibration was performed for every measured dataset and an intensity and wavelength calibrated spectrum for argon (diagnostics laboratory setup; PFN: 20 kV, 400 A; 50 mbar buffer pressure) is shown in Fig. 3.6. Although calibrated, peaks with different central wavelengths do not completely overlap, especially when the intensity is low. This increases the

uncertainty of the calibration, at least at the edges of the CCD sensor, shortly after the discharge for example at 0.55 µs (Fig. 3.6b) and long after the discharge, for example at 9.05 µs (Fig. 3.6c) (see Section 4.4.1 for uncertainty discussions).

3.5 Temperature Determination in LTE Plasmas

The electron temperature in an LTE or pLTE plasma can be determined by using the Boltzmann plot (Section 2.7). For this, the left hand side of Eq. (2.45) can be plotted versus the energy of the upper level E_u for multiple emission lines that are in LTE. The electron temperature is then obtained from the slope $m = -1/k_B T$ of this plot. The intercept of Eq. (2.45) with the energy axis can in certain situations also give the relative or absolute concentration of atoms or ions (Zhang et al. 2019; Zalach et al. 2013).

If the upper energy levels of the measured transitions for the Boltzmann plot are very close to each other, this can result in large uncertainties and therefore lines with the largest available energy spacing should be used (Zhang et al. 2019). For the argon measurements in this study only a small energy level spacing of approximately 0.4 eV could be reached. The accuracy of the Boltzmann plot is affected also by the uncertainty in the measured emission coefficients ϵ_{ul} and the uncertainty on the transition probabilities A_{ul} (W. L. Wiese 1991; Zalach et al. 2013). It is therefore also important to choose emission lines with transition probabilities that are known with a good accuracy. For the emission lines that were visible with our setup the accuracy was similar for most of the lines. To reduce also uncertainties from the A_{ul} coefficients, the maximum of visible emission lines were chosen. Multiple emission lines with similar energies can also mitigate the effect of outliers in the accuracy of the A_{ul} coefficients (Zalach et al. 2013).

Significant deviations from the straight fit line can already give rise to deviations from the LTE assumption or inaccuracy in the transition probabilities (Griem 1997, p. 282). Emission lines which have the same upper level should also result in the same vertical (and horizontal) position in a Boltzmann plot if they are not self absorbed. This is because in the left hand side of Eq. (2.45) the values A_{ul}, λ_{ul} and the escape factor θ_{ul} of the emission coefficient (Eq. (2.38)) cancel out such that only $n_u \theta_{ul}$ remains in the logarithm of Eq. (2.45). The validity of the Boltzmann plot method has for example been investigated for argon by Ohno et al. 2006 and compared to Thompson scattering experiments by Wang et al. 2018.

3.6 Temperature Determination in Non-LTE Plasmas

If the plasma is not in LTE then the determination of the temperature is more complex and generally CRMs (Section 2.5 and Appendix A) are needed. In this work the treatment of a CRM

was restricted only to an argon plasma. Commonly, the electron temperature and density can be extracted from measurements with a CRM in two different ways: either the temperature is obtained by using line ratios between suitable lines that show a temperature or density dependence (Donnelly 2004; Iordanova et al. 2007; Kano et al. 2000; Vries et al. 2006; X. M. Zhu et al. 2009; Siepa et al. 2014) or by fitting the modelled population distribution to as many experimental population densities (extracted from emission lines) as available (X.-M. Zhu et al. 2010a; Gangwar et al. 2012; Evdokimov et al. 2017; Durocher-Jean et al. 2019). A review on the line-ratio method was also given by X.-M. Zhu et al. 2010b.

If it is possible to measure a set of lines with different upper levels, for example lines corresponding to the $2p$ transition array in argon, then the most accurate results can be obtained by fitting the modelled distribution of levels to the experimental distribution instead of using line ratios (X.-M. Zhu et al. 2010b). Since we require only a relative calibrated setup it is necessary to define a relative quantity to fit theoretical and measured intensities (Evdokimov et al. 2017). Using the approach of Evdokimov et al. 2017 similar to X.-M. Zhu et al. 2012 we define the relative quantity using the emission coefficient in Eq. (2.38) as

$$\epsilon_{x,\text{rel}} = \frac{\epsilon_x}{\sum_i \epsilon_i}. \tag{3.2}$$

Where the emission coefficient of a certain line x is normalized to the sum over all lines under investigation.

This relative quantity can also be defined by using the experimentally obtained population density distribution (ASDF). The population density $n(u)$ of a transitions upper level u can be used instead of ϵ_{ul}, where the upper level is commonly divided by its degeneracy g_u (X.-M. Zhu et al. 2010a). Using the measured emission coefficients ϵ_{ul} Eq. (2.32) this is

$$n(u) = \frac{\epsilon_{ul}\lambda_{ul}}{A_{ul}g_u}\frac{4\pi}{hc}, \tag{3.3}$$

with the wavelength λ_{ul} and Einstein coefficient A_{ul}. To include self-absorption Eq. (2.38) must be used.

The quantities Eq. (3.2) or Eq. (3.3) must be defined for the measured emission lines ($\epsilon^{\text{meas}}_{x,\text{rel}}$) and for the corresponding theoretical lines in the model ($\epsilon^{\text{theor}}_{x,\text{rel}}$). To find the most probable electron temperature and density the difference between measurement and model can be minimized with

$$\Delta = \sqrt{\sum_x (\epsilon^{\text{meas}}_{x,\text{rel}} - \epsilon^{\text{theor}}_{x,\text{rel}})^2}. \tag{3.4}$$

This quantity Δ depends on the electron density and temperature and depending on the processes included in the CRM also on variables like the pressure, gas temperature or plasma dimensions.

If processes like diffusion are included in the model the minimization might also not have a unique solution for every parameter (Evdokimov et al. 2017).

Quantities like Eq. (3.4) can also be defined differently, for example by including weights for different uncertainties in the measured lines (Malyshev et al. 1999; Durocher-Jean et al. 2019).

Chapter 4

Electron Temperature in Hydrogen Plasmas

4.1 Spectra

For the temperature determination the emission coefficients (Section 2.6) of the measured emission lines need to be obtained. To extract the emission coefficients from the measured hydrogen Balmer lines (Table 3.1) the spectra were averaged, background subtracted, calibrated and the spatial axis of the CCD projected on the wavelength axis to maximize the signal (no spatial resolution at the FLASHForward setup Section 3.2.2).

4.1.1 Spectral Line Fitting

The spectra were analysed with Python, in particular with the LMFIT package (Newville et al. 2014; Newville et al. 2021) which allows to fit peak-like models to the data. The shape of the line emission is well represented by the convolution of a Lorentzian and Gaussian profile. The Lorentzian component is caused by the high electron densities that lead to Stark broadening (Gigosos et al. 1996) and the Gaussian component by the temperature dependent Doppler and instrumental broadening (Kunze 2009, p. 156). To account for both broadening components the fits were performed using pseudo-Voigt models that is a weighted sum of a Gaussian and Lorentzian distribution function (LMFIT Newville et al. 2021, p. 93).

The measured Balmer lines and two example fits at different time steps for each line are shown in Fig. 4.1. The different time steps show that the line widths and heights change over time for each line. The H-β line shows as the only one a double peak structure (Fig. 4.1c) in the time from 0.4 µs to 1.2 µs which was fit using a double pseudo-Voigt model. This peak structure arises because the high electron density causes a Stark broadening and H-β has no unshifted central stark components as opposed to H-α and H-γ (W. L. Wiese et al. 1975). The peak separation can also be used for electron density determination (Parigger et al. 2018). Until 1 µs some part of the distribution also falls out of the wavelength range of the CCD sensor as seen in Fig. 4.1c. The H-γ line has the lowest intensity and approximately until 1.4 µs, also here some part of the distribution falls out of the sensor range (Fig. 4.1e).

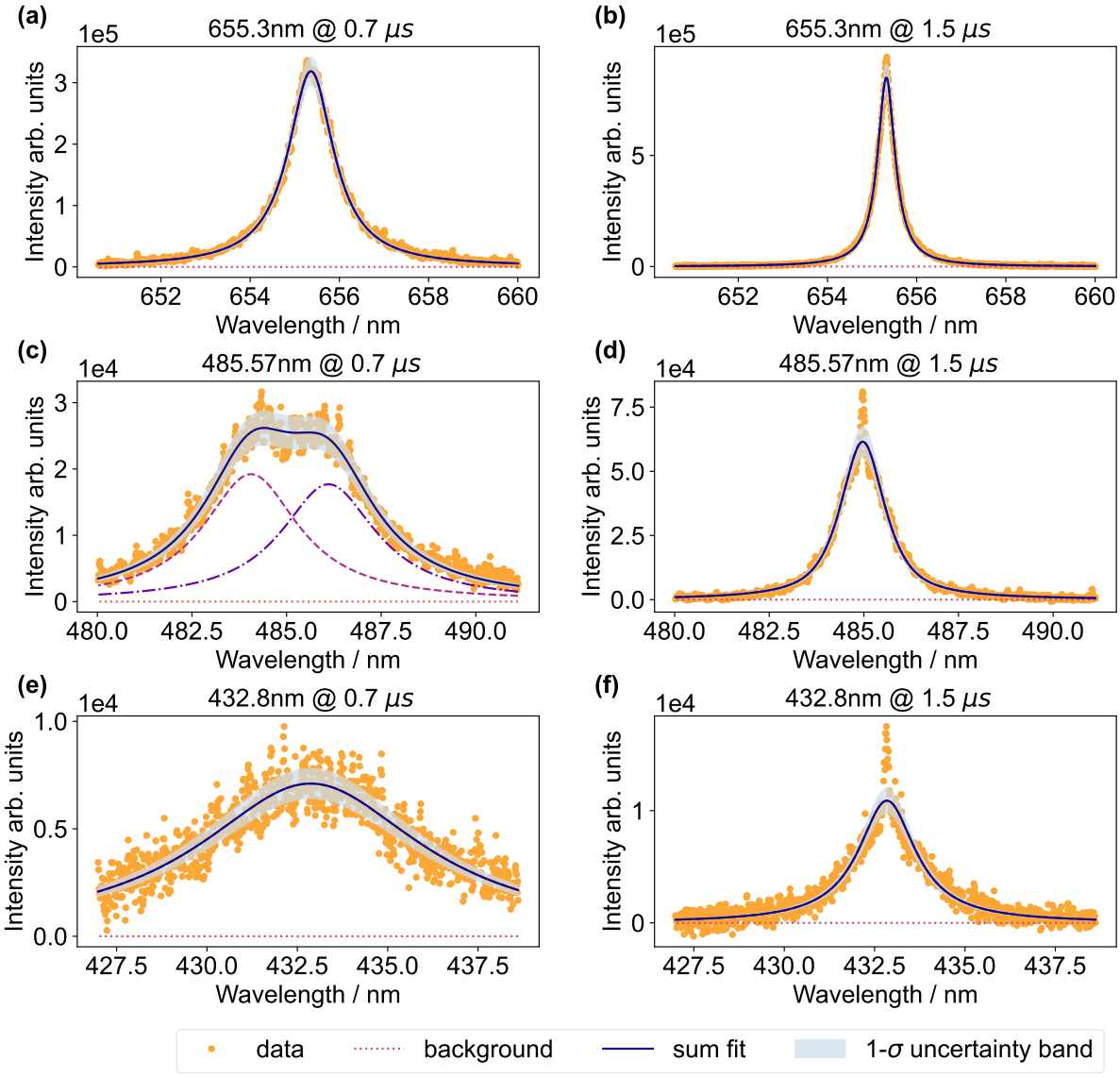

Figure 4.1: Selection of spectral fits for hydrogen. The uncertainty bands include the uncertainty of the calibration and the fits. Only the sum fit is labelled, the individual components as in **(c)** are not labelled. **(a)-(b)** H-α line, **(c)-(d)** H-β line and **(e)-(f)** H-γ line.

A frequently reoccurring pattern in the peak structure is a super Lorentzian shape that is too sharply peaked for the pseudo-Voigt fits (full Lorentzian in this case). This is observable in all three lines and is postulated to be caused by the integration time over 200 ns. To illustrate that, we deliberately use a measurement with an integration time of 400 ns for the H-β line with, apart from that, the same conditions (Fig. 4.2). The integration over a time interval is for hydrogen plasmas an average over different line widths and heights and for H-β also an average over different peak shapes (double peak structure). In Fig. 4.2a we see that there is a smeared out double peak structure and in Fig. 4.2c, 0.8 µs later, the double peak structure is basically gone. The time step in between (Fig. 4.2b) shows a double peak structure as well as a superimposed

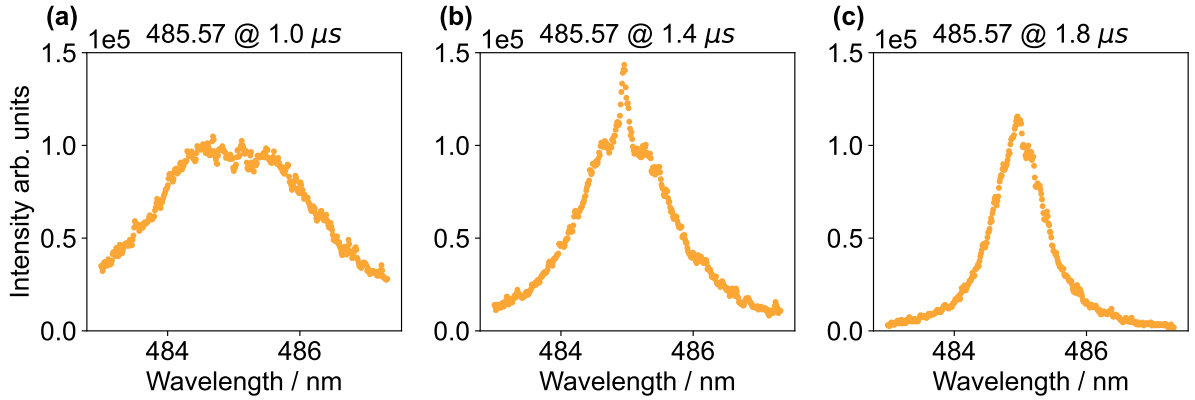

Figure 4.2: Measurements of the H-β line with 400 ns integration time. Three successive time steps are shown without fit and limited to the pixels around the center.

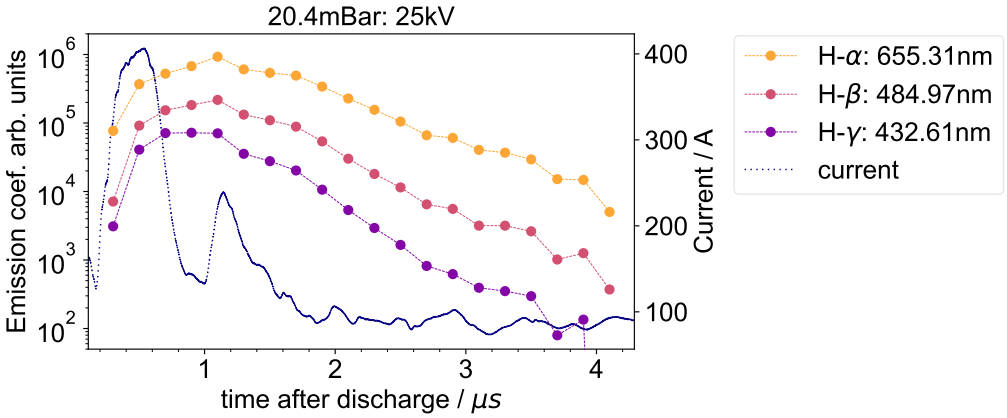

Figure 4.3: The emission coefficient in arbitrary units of the measured Balmer lines. The current trace of the discharge is also plotted.

single peak structure. This is an unrealistic peak structure, because H-β has no unshifted central stark components and should therefore show a dip in the center if stark broadening causes a line splitting. This peak structure must therefore be attributed contributions from different time steps. For single peak structures this causes sharper peaks because the decreasing Stark broadening decreases the line wing contribution while the line center contribution increases. A model that reflects the real shape would be necessary, but it was out of the scope of this work to implement such a model in a consistent manner (especially for the peaks that are not fully captured by the sensor).

The relative emission coefficients (Section 2.6) were obtained by integrating the fitted pseudo-Voigt peaks and are shown in Fig. 4.3 for the three hydrogen lines. For clarity, the error bars are omitted in these plots. By observing the recorded current trace of the discharge in Fig. 4.2, we see that the line emission increases during the discharge peak and also until the reflection of the discharge peak (second peak at around 1.2 µs).

4.2 Choice of Analysis Method

To analyse the emission coefficients we need to choose an appropriate method, either the Boltzmann plot method in Sections 2.7 and 3.5 if LTE/pLTE prevails or the CRM approach in Sections 2.5 and 3.6 if LTE/pLTE is not present. To chose the most appropriate method we apply the criteria of Section 2.4 to the hydrogen plasma.

4.2.1 Requirements for LTE

For the hydrogen measurements it was possible to measure the electron density directly from the broadening of the H-α line as described by Garland et al. 2021. The result of this measurement is shown together with its current trace in Fig. 4.4a and gives a maximum electron density of around $1 \times 10^{17}\,\mathrm{cm}^{-3}$. This measurement is, as the emission coefficients, averaged over space and time (setup in Section 3.2.2).

For complete LTE Eq. (2.12) must be fulfilled for the largest gap between adjacent levels, which is the first resonance transition of hydrogen with an energy spacing of $\Delta E_{ul} = 10.2\,\mathrm{eV}$. As hydrogen has only neutral lines, the Gaunt factor (Fig. 2.1) for neutral atoms was used in Eq. (2.12) and we obtain for e.g. 1 eV a critical electron density for complete LTE of $n_e = 1.26 \times 10^{18}\,\mathrm{cm}^{-3}$. Figure 4.4b shows the minimum required electron density for complete LTE at temperatures of 0.1 eV to 10 eV.

The required electron density is too high to reach complete LTE, but if the condition would be relaxed by an order of magnitude as proposed for optical thick conditions of transitions to the ground state (Section 2.4.1), then the plasma could possibly shortly reach complete LTE at its maximum density.

4.2.2 Requirements for Partial LTE

To check if alternatively pLTE can exist for the measured lines, we use the criteria introduced in Section 2.4.3. Among the measured lines the H-α transition from $n = 3$ to $n = 2$ has the lowest upper level. This level is therefore relevant to determine if pLTE conditions can exist. We use Eqs. (2.16), (2.18), (2.20), (2.22), (2.24) and (2.26) to asses the validity of pLTE conditions and show the results in Fig. 4.5.

Figure 4.5a shows the criteria for steady state ionisation balance. The criterion of van der Mullen 1990 was suggested (Section 2.4.3) to give the most reliable results for neutral hydrogen. From this plot, the required electron density will only eventually be too low at times comparable to 3 µs to 4 µs after the discharge, also if we take highest criterion at each temperature. To apply the criteria by Fujimoto et al. 1990 for ionizing or recombining plasmas we consider the

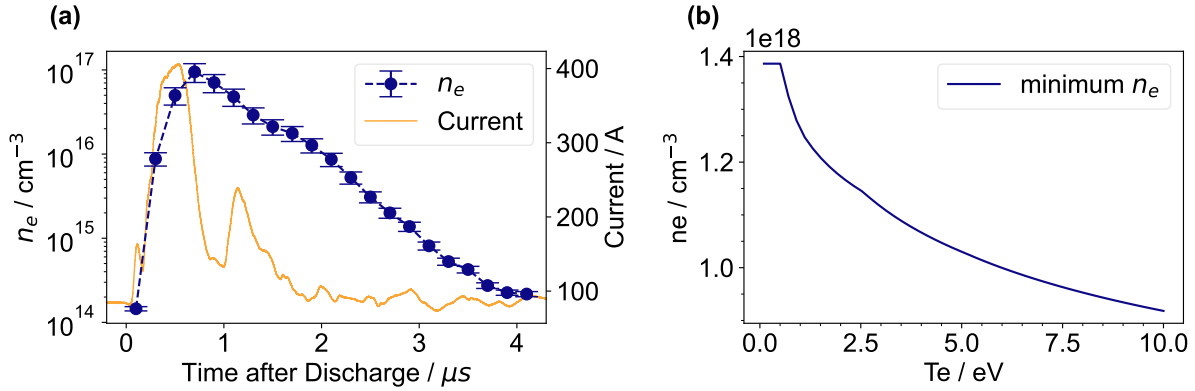

Figure 4.4: **(a)** Average electron density for the hydrogen plasma with $\Delta E_{ul} = 10.2\,\text{eV}$. **(b)** Minimal required electron density calculated with Eq. (2.12) and the Gaunt factor of Fig. 2.1 for an electron temperature range of 0.1 eV to 10 eV (at low temperatures the factor $(k_B T_e/\text{eV})^{1/2}$ in Eq. (2.12) cancels with the Gaunt factor approximation, producing a constant value).

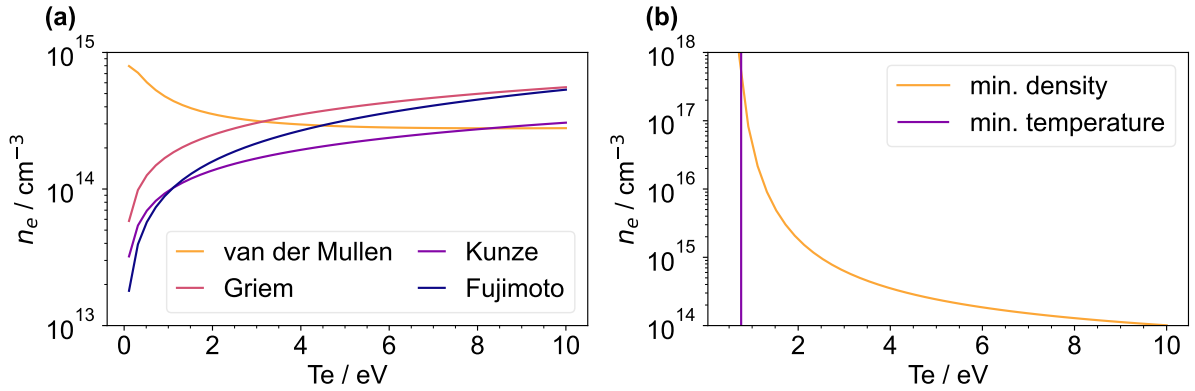

Figure 4.5: The pLTE requirements for hydrogen levels with a principal quantum number of $n = 3$. **(a)** Minimum required electron density n_e calculated according to van der Mullen 1990 with Eq. (2.20), Griem 1963 with Eq. (2.16), Kunze 2009 with Eq. (2.18) and the ionization balance criterion of Fujimoto et al. 1990 with Eq. (2.22). **(b)** Minimum required electron density for a fully recombining plasma according to Fujimoto et al. 1990 with Eq. (2.26) and the minimum required electron temperature of 0.76 eV from Eq. (2.24) (which is independent from the electron density in this formula).

electron density evolution in Fig. 4.4b and observe that the plasma has an ionizing character during the discharge pulse and a recombining character after the discharge. If we deal now with the fully recombining plasma and neglect the short period of ionization, then the criterion of Fujimoto et al. 1990 requires for pLTE significantly higher electron densities at low temperatures (Fig. 4.5b) and can break the pLTE conditions. However, this case requires zero contribution from the atomic ground state which will not be the case in our plasma. Still, the plasma has a recombining character (after the initial ionization phase) and this could increase the required density compared to Fig. 4.5a to reach pLTE.

From this standpoint the hydrogen plasma could show deviations from LTE at low tem-

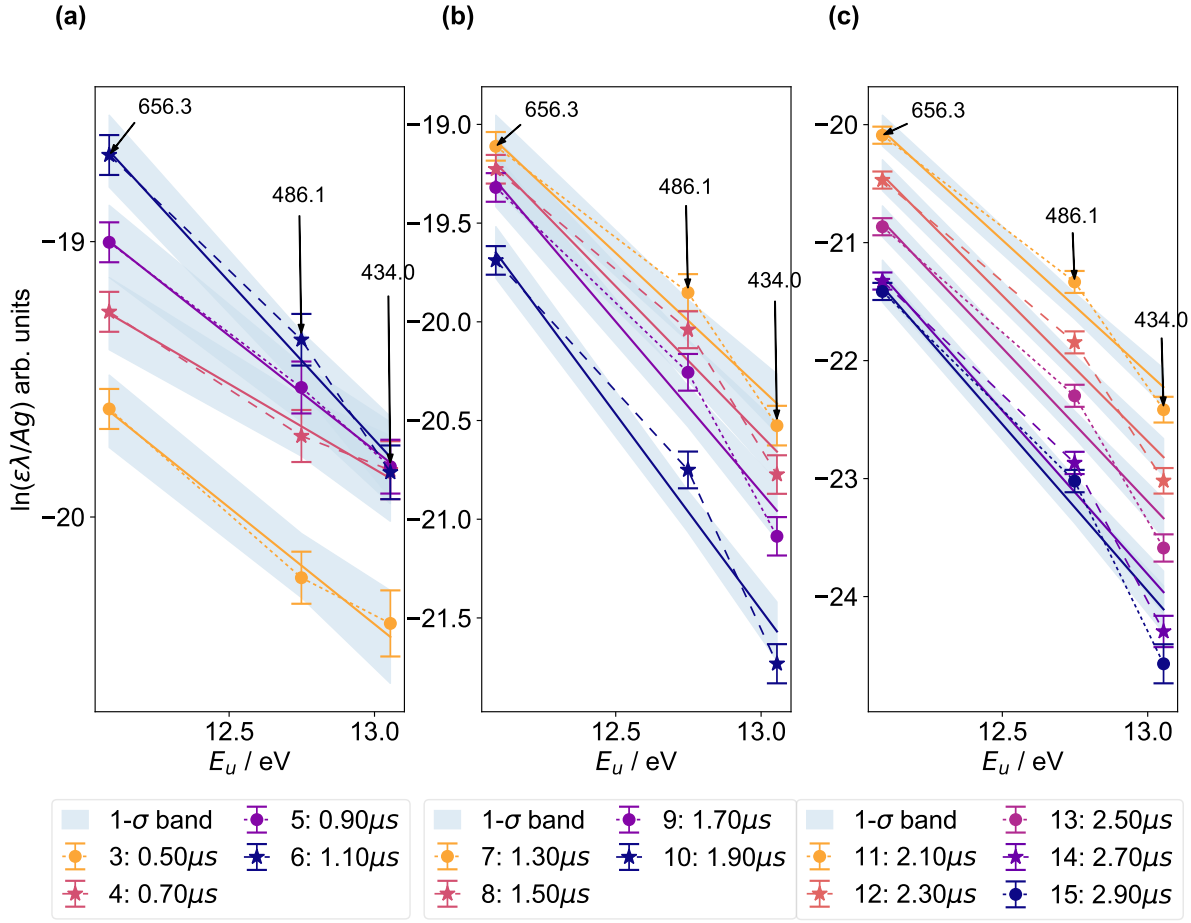

Figure 4.6: Boltzmann plots for successive time steps after the discharge. Successive steps are labelled with alternating markers for better comparison and the wavelengths are annotated in nm. The 1-σ error bands results from the weighted linear fits.

peratures but as the ionisation balance criteria require a significantly lower density the pLTE assumption seems to be justified at least while the electron density is high enough in the beginning. This justifies to use the Boltzmann plot to determine the electron temperature.

4.3 Temperature Analysis with Boltzmann Plots

If we perform the Boltzmann plot analysis method for the measured emission lines (Section 3.5 and Eq. (2.45)), we expect that the data points have a linear gradient if pLTE is valid. Figure 4.6 shows the Boltzmann plots of the H-α, H-β and H-γ line for successive time steps after the discharge and Fig. 4.7 the resulting temperatures together with the discharge current. To obtain the temperature from those data points a weighted linear fit was performed. The weights were the inverse of the uncertainties of the data points, such that values with large uncertainties contributed less to the fits and the temperature. The measurements after 2.9 µs were omitted in these plots since the signal to noise ratio of the H-γ was too small.

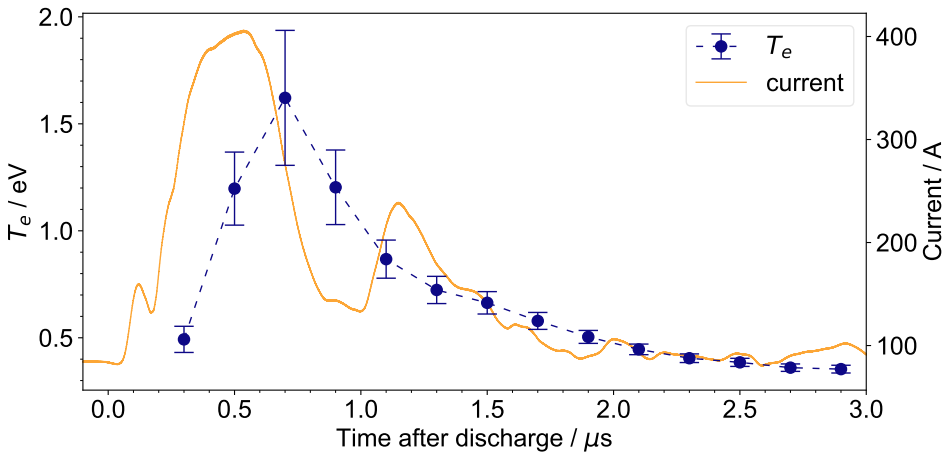

Figure 4.7: Electron temperature for the hydrogen plasma for a measurement with an integration time of 200 ns compared to the discharge current.

The temperature measurement in Fig. 4.7 shows a temperature evolution with a peak temperature of about 1.60 eV ± 0.40 eV after 0.7 µs. The electron temperature follows the discharge current and can also be seen to react to the reflected part of the current profile (1 µs to 1.5 µs) with a slight change in the decay rate at around 1.3 µs. It reaches a minimum of approximately 0.35 eV after 3 µs and will eventually not reach temperatures below 0.3 eV at longer timescales. The error bars are largest in the beginning and immediately after the the discharge when the intensity of the β- and γ-lines are low and the β-line is split. The small error bars at lower temperatures are due to the fact that the error of the slope of the linear fits, which is $m = 1/k_B T$, stays approximately the same (slight increase after 2.0 µs), while the value on the slope increases. In result the relative error on the slope decreases and the error bars on the temperature become small.

The Boltzmann plots show in general an increasing systematic mismatch between fit and data during the plasma evolution, this can already be an evidence for deviations from pLTE conditions and will be discussed together with the other uncertainties in the following sections.

4.4 Measurement Uncertainties

The measurement uncertainties are those which are drawn as error bars in the Boltzmann plots (Fig. 4.6) and consist of contributions from the calibration, the A_{ul} coefficients and the line fitting. For hydrogen Balmer lines the uncertainty on the A_{ul} coefficients is $\leq 0.3\,\%$ and therefore negligible. The uncertainties in the calibration and the line fitting are combined with Gaussian error propagation to the uncertainty drawn in the spectral fits shown in Fig. 4.1. The uncertainty on the emission coefficient for Fig. 4.6 is obtained by the difference of the integral with and without added uncertainties.

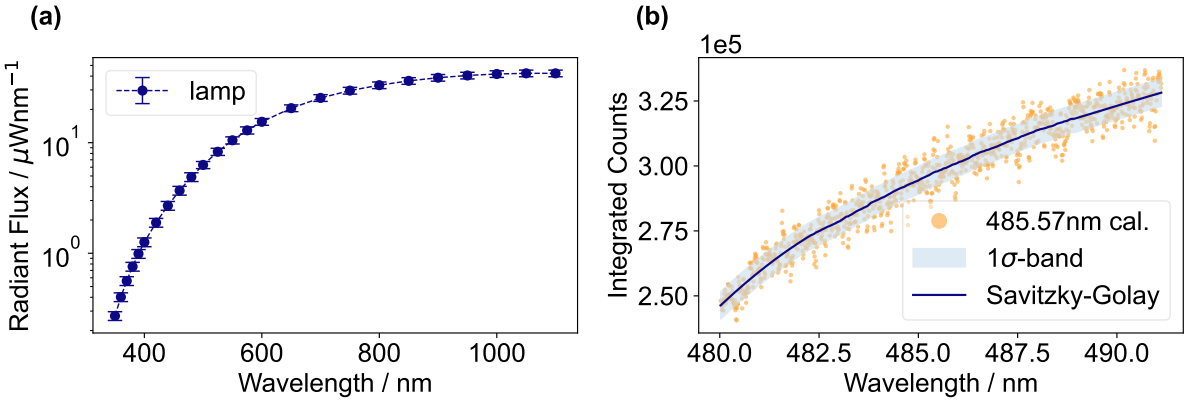

Figure 4.8: (a) Calibration lamp signal with uncertainty values measured by the manufacturer. **(b)** Calibration lamp signal at 485.57 nm for the FLASHForward experiment setup together with the Savitzky-Golay de-noised average and the 1-σ-band.

4.4.1 Calibration

The 1-σ uncertainty for the absolute radiant flux of the calibration lamp is given by the manufacturer to 7 % to 9 % in the spectral range of 400 nm to 1000 nm. The relative uncertainty is larger for shorter wavelengths and smaller for longer wavelengths and shown in Fig. 4.8a. This uncertainty refers foremost to the absolute scale of the radiant flux and the uncertainty on the shape of the calibration function should be small according to private communications with the manufacturer. As the measurement only requires a relative calibration, the uncertainty on the absolute scale is irrelevant and the absolute uncertainty by the manufacturer will overestimate the uncertainty in our measurements.

The spectra obtained with the calibration lamp, as shown in Fig. 4.8a, were de-noised with a Savitzky-Golay filter (Savitzky et al. 1964) before they were used for the calibration. To estimate the additional uncertainty the 1-σ standard deviation of the distribution of the residua between de-noised measurement and measurement was used (Fig. 4.8b). As already seen in the calibrations in argon Figs. 3.6b and 3.6c, the calibration is not always perfect and identical peaks (at the edges of the spectral ranges), which were measured with different central wavelength set points of the spectrometer, showed not exactly the same amplitude. This is larger for low intensities in the beginning and the end but is expected to be smaller at the central wavelength at the center of the sensor. To account for those uncertainties and because it was not possible to disentangle the uncertainty on the absolute and relative scale, the 7 % to 9 % uncertainty stated by the manufacturer was used to provide an upper limit for the calibration uncertainty.

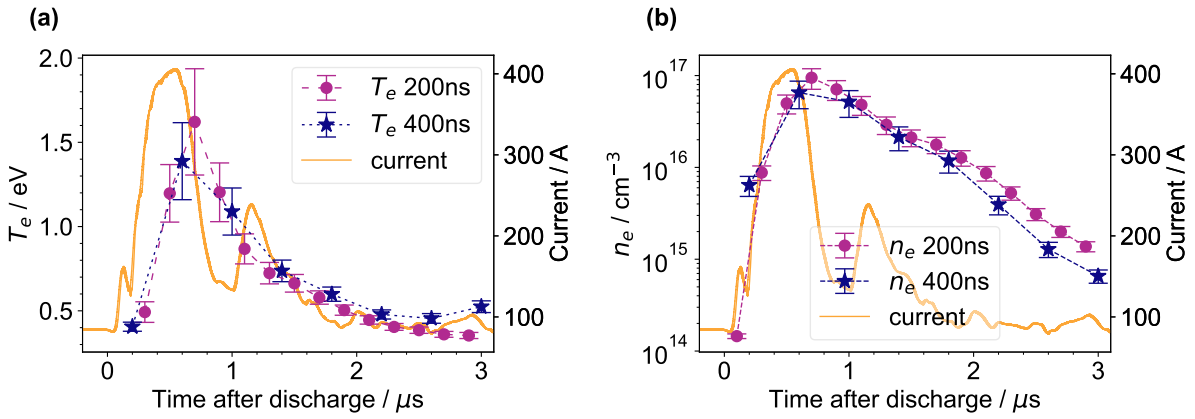

Figure 4.9: Comparison of the measurement at the 25 kV, 20.4 mbar buffer pressure working point with a 200 ns and 400 ns integration time. **(a)** Electron temperature, **(b)** electron density.

4.4.2 Line Fitting

The uncertainty contribution of the line fitting (Fig. 4.1) is estimated by using LMFIT, which offers the possibility to obtain the uncertainty band for a successful fit (LMFIT, Newville et al. 2021, pp. 37–38).

4.4.3 Integration Time

As the integration over 200 nm results in a profile that is not described by a single Lorentzian, but was fit with a single Lorentzian, additional uncertainty could be introduced. A comparison between the 200 ns measurement and the measurement with the same conditions, but an integration time of 400 nm, can be used to estimate the impact on the temperature results. In Fig. 4.9 we see between the measurements of 200 ns and 400 ns integration time a good agreement within the error bars at the maximum temperatures, although more temporal averaging is evident for 400 ns. At later times the electron temperature and also the electron density (Fig. 4.9b) show stronger disagreement which could be the result of deviations from pLTE, self absorption or also the longer integration time. The good agreement with the 400 ns measurement suggests that the uncertainty due to the 200 ns integration time averaging will not affect the maximum temperatures that would be obtained with shorter integration time strongly.

4.5 Model Concept Uncertainties

From the Boltzmann plots (Fig. 4.6) and the fit quality in terms of a χ^2/n_{dof} statistic in Fig. 4.10 we see that the fit quality of the linear fit decreases with time. The fit quality is best at the highest electron densities and decreases with time which is in disfavour of calibration problems

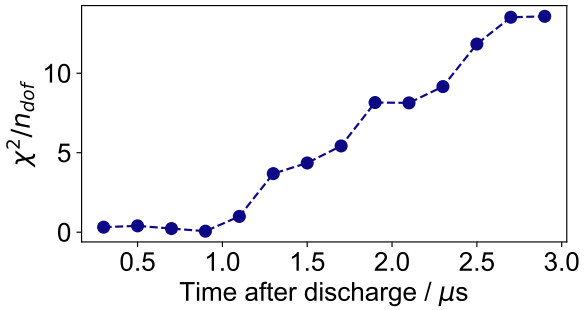

Figure 4.10: The fit quality of the Boltzmann plots from Fig. 4.6 in terms of a χ^2/n_{dof} statistics, where n_{dof} are the degrees of freedom.

because the calibration should be independent of the line intensity. The uncertainties in the measured emission coefficients are also smallest in the intermediate time steps when the effect steadily increases, which also implies that this mismatch is the result of uncertainties in the model assumption. If no other systematic measurement problems cause this discrepancy this must be attributed to deviations from pLTE or self absorption.

4.5.1 Requirements for Partial LTE

The Boltzmann plots (Fig. 4.6) show that the systematic deviations from the straight fit lines are not covered by the uncertainty starting from 1.3 µs. From this time on deviations from LTE could be possible. Now that we have analysed the temperature, we can re-evaluate the requirements which would need to hold for pLTE conditions. The temperature after 1.3 µs is decreasing approximately from 0.7 eV to 0.3 eV (Fig. 4.7) and the required electron density for a steady state plasma (Fig. 4.5a) can be close to 1×10^{15} cm^{-3} for this temperatures. According to the electron density in Fig. 4.4b this is only the case after approximately 3 µs, thus it should not cause the deviations. If we consider the recombining character in Fig. 4.5b, we see that for such low electron temperatures the required electron density is substantially higher and the temperature is after 1.3 µs even below the required minimum temperature of 0.76 eV. As the recombination rate will get smaller with time and more ground state atoms will be present, the required density for a fully recombining plasma will probably overestimate the required density. This would shift it again more towards the density required for steady state (Fig. 4.5a).

It therefore could be postulated that the plasma has increasing deviations from pLTE after 1.3 µs, but fulfils pLTE conditions at the highest electron densities around 0.7 µs to 0.9 µs. Theses calculations for the pLTE requirements were also only made for the H-α transition ($n = 3$), for H-β ($n = 4$) and H-γ ($n = 5$) the required electron densities can be relaxed by roughly one, respectively two orders of magnitude. Thus, for H-β and H-γ the pLTE conditions should not be violated and this would render them more reliable. If the Boltzmann plots are only performed

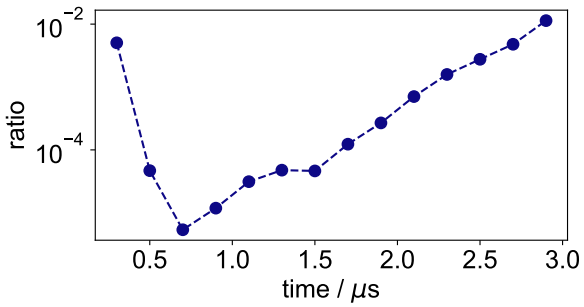

Figure 4.11: The ratio obtained from Eq. (4.1) for the change rate in the plasma parameters. Here the relaxation time from Eq. (2.29) and the electron density and temperature from Figs. 4.4b and 4.7 was employed.

with those two lines then this leads at later times to a faster temperature decay and minimum electron temperatures in the range of 0.2 eV instead of 0.35 eV.

4.5.2 Requirements for Steady State in pLTE

We also want to check if the plasma evolution can be too fast to establish pLTE conditions even if the electron density is sufficiently large (see also Sections 2.4.2 and 2.4.4). To avoid averaging over the density and temperature peak we express for that purpose Eq. (2.13) in terms of the slope $m = \Delta n_e/\Delta t$ between successive points in the time evolution as

$$\frac{n_e(t+\tau_{\text{rel}}) - n_e(t)}{n_e(t)} \approx \frac{\frac{\Delta n_e}{\Delta t}\tau_{\text{rel}} + n_e(t) - n_e(t)}{n_e(t)} = \frac{m\,\tau_{\text{rel}}}{n_e(t)} \ll 1. \tag{4.1}$$

We check the conditions for pLTE by applying Eq. (2.29) for the relaxation time τ_{rel} in Eq. (4.1). First, we notice that the functions $\psi(x)$ in Eq. (2.29) depend on the electron temperature and that for small temperatures x is getting large. This causes $\psi(x)$ to be very small (compare also Drawin 1969) and therefore the relaxation time to be very large. Reasonable estimates for the relaxation time can only be obtained if T_e is known (this can also only be an estimation since T_e may change if pLTE conditions do not hold).

By taking the electron temperature and density from Figs. 4.4b and 4.7 we obtain with Eqs. (2.29) and (4.1) for level $p = 3$, the results in Fig. 4.11. As the ratio is $\ll 1$ this suggest that the evolution is not the limiting factor to reach pLTE conditions for the H-α transition. Figure 4.11 suggests also that not the rapid change in plasma parameters at the peak electron density but the combination of decaying electron density and low temperature produces the largest ratios. If lower-lying levels would be considered, then this condition could be easily violated.

4.5.3 Radiation Trapping / Self Absorption

Self absorption could also contribute to the deviations from the linear fits in Fig. 4.6. Self absorption is stronger if the distance the light travels through the plasma is long (Eq. (2.36)) and

also if the density of the lower level of the transition is high (Eq. (2.37)). As the light in average only needs to pass through half of the diameter of the plasma cell (0.75 mm) self absorption might not play an important role, but without the densities of the lower levels it is difficult to estimate this effect.

4.6 Conclusion

The electron temperature in hydrogen could be successfully determined with the Boltzmann plot method although there remain some uncertainties in the model and the quality of the data. At the highest electron densities and temperatures the measured lines showed the best agreement with the linear fit of the Boltzmann plot. This is also the region where the closest agreement with pLTE conditions is expected. With decreasing electron densities systematic deviations from the linear fit, which are not covered by the uncertainties, become visible. As the uncertainties contain relative and absolute scale uncertainties, these are also expected to overestimate more than underestimate the real uncertainty and make systematic deviations more likely. Deviations from pLTE conditions become possible after 1.3 µs and are most likely the result of the recombining character of the plasma, because the ionisation balance criteria for pLTE would not expect deviations. Still, the criteria in the literature are not unambiguous and should be considered as estimates. The sharp rise and decay of the electron temperature and electron density of the plasma seems also to be less a problem for the pLTE conditions than the low electron temperatures and densities at later times. Self absorption could also contribute to these deviations, but could not be verified and the integration time of 200 ns also appears to change the temperature results not drastically, as shown with the 400 ns integration time measurement. If the discrepancy is only caused by deviations from pLTE, then the effect on the temperature would be a faster decay and possibly a lower minimum temperature of around 0.2 eV instead of 0.35 eV because this should only affect the H-α. Therefore the temperatures after 1.3 µs could also be systematically lower despite their small uncertainties.

Chapter 5

Electron Temperature in Argon Plasmas

5.1 Spectra

For the data analysis the spectra were also averaged, background subtracted, calibrated and projected to the wavelength axis. The setup for the argon measurements was the diagnostics laboratory setup (Section 3.2.1) and spatial resolution was available. From the available 1024 pixel on the spatial axis only a slice of the inner 100 pixel corresponding to approximately 0.8 mm was used for the analysis to limit spatial averaging.

A general feature which was consistently found in all measured spectral lines is a mismatch between the fit with a single pseudo-Voigt model and the shape of the peak on the left shoulder where the peak is too broad. This mismatch is suggested to be the result af a capillary reflection and will be discussed first.

5.1.1 Virtual Image from a Capillary Reflection

The fit quality can be improved by introducing a second peak that is a shifted and intensity reduced copy of the main peak (Fig. 5.1) and we postulate that this is the result of a reflection of the main peak at the sapphire capillary. This suggestion is supported by wavelength calibration measurements which were measured at the same setup but without the capillary. In these measurements the laser (Fig. B.1c) and Xenon lamp (Fig. B.1d) measurements did not show this distortion.

To approximate the reflected power, the direct reflection at the inner side of the capillary (argon-Sapphire interface) and a secondary reflection of the transmitted light at the backside of the capillary (Sapphire-Vacuum) were considered. Using the Fresnel-equations, for simplicity for non-polarized light incident perpendicular to the surface, the reflected power R can be expressed as (Hecht 2017, p. 131)

$$R = r^2 = \left(\frac{n_i - n_t}{n_i + n_t} \right)^2 \tag{5.1}$$

where r is the amplitude coefficient for reflection, n_i the refractive index on the incident side and n_t the refractive index on the transmitted side. We can combine both of those reflectances

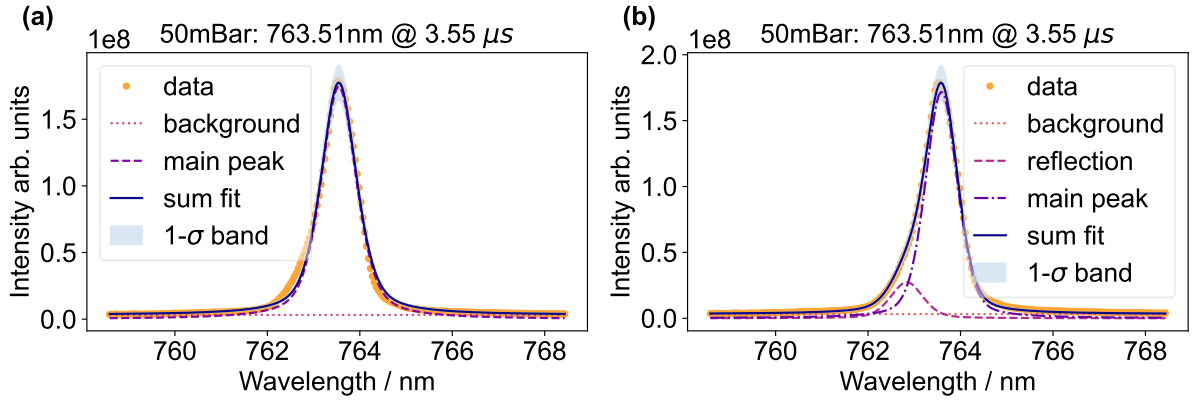

Figure 5.1: **(a)** Single pseudo-Voigt fit, **(b)** pseudo-Voigt fit with an additional peak added to take the virtual image due to an optical reflection into account.

at the capillary by using $R + T = 1$ into

$$R_{\text{saph}} = R_{\text{Ar-saph}} + (1 - R_{\text{Ar-saph}}) R_{\text{saph-vac}}. \tag{5.2}$$

To calculate Eq. (5.2) the refractive index of the argon plasma was assumed to be 1 and the wavelength dependent refractive index for sapphire was taken from Polyanskiy 2022 and references therein.

To model the reflection also a pseudo-Voigt peak model was used and The additional peak was closely constrained to the main peak shape, which was also necessary to maintain the stability of the fitting routine. The pseudo-Voigt model was displaced by 0.75 nm to the left, had the same FWHM, the same fraction of Lorentzian components with respect to the main peak and the amplitude calculated with Eq. (5.2). The amplitude of the reflection, calculated with the above approach, is about 15 % to 17 % of the main peak and was used for the analysis. By making a simple guess for the additional peak and by optimizing it for the most consistent result, similar numbers (15 % to 20 %) could confirm this amplitude.

5.1.2 Spectral Line Fitting

With this additional peak for the reflection the peaks were fitted and the results for some emission lines for the argon plasma at a voltage of 20 kV and backing pressure of 50 mbar are shown in Fig. 5.2.

The effect of the capillary reflection would only be a change in the peak area which would be similarly for every peak, if the peak separation was clear (Figs. 5.2c and 5.2d). The effect on peaks that are too close to be resolved individually (denoted as double peaks in this work), for example Figs. 5.2a and 5.2b, can be more problematic. In these cases the reflections of both peaks can, if they are not included in the peak model, falsely be attributed to the left peak

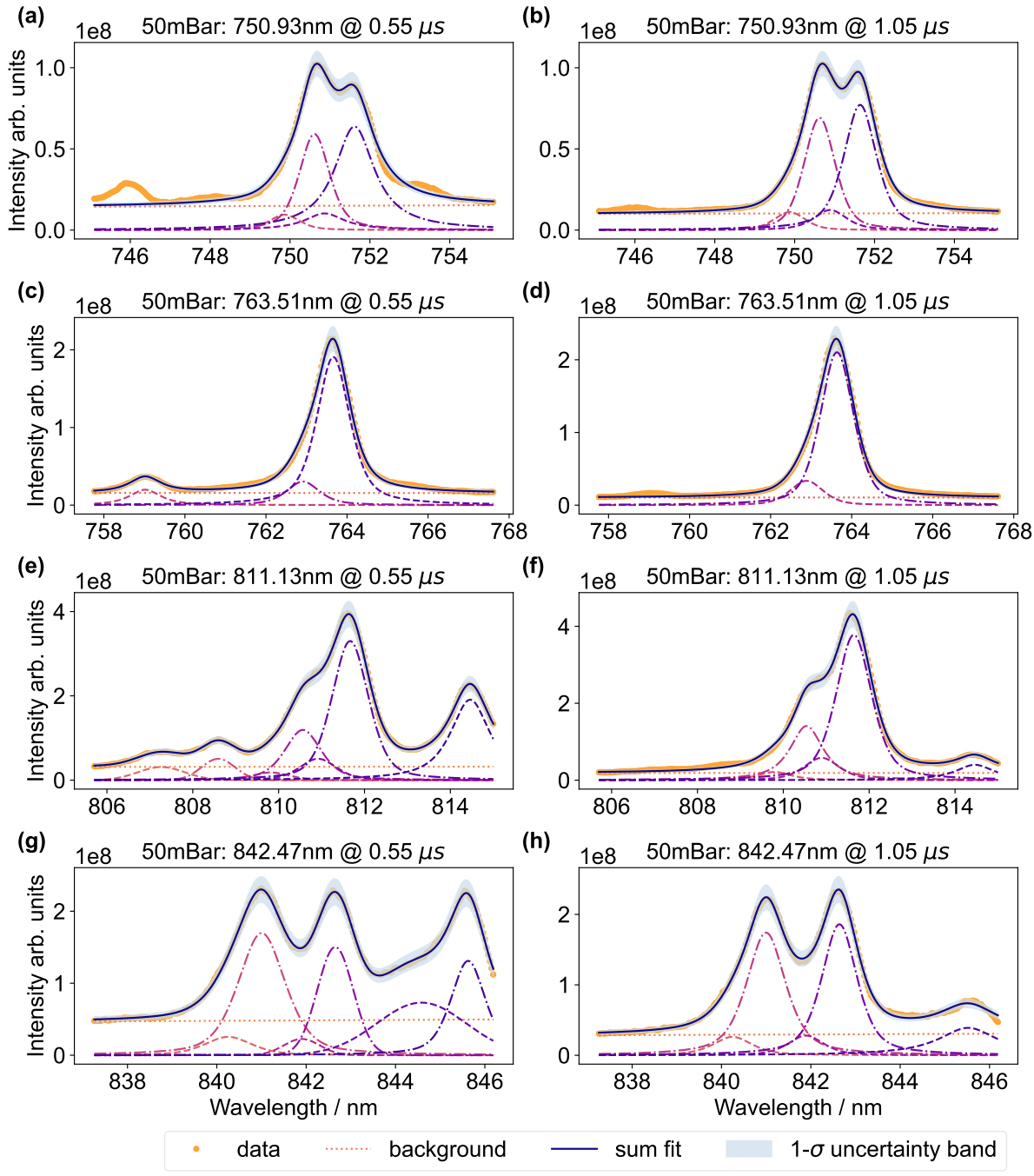

Figure 5.2: Selection of spectral fits for a voltage of 20 kV and a backing pressure of 50 mbar. The emission of higher excited / ionized levels diminishes after 1 µs. Individual fit components are not labelled rather the sum of all components is.

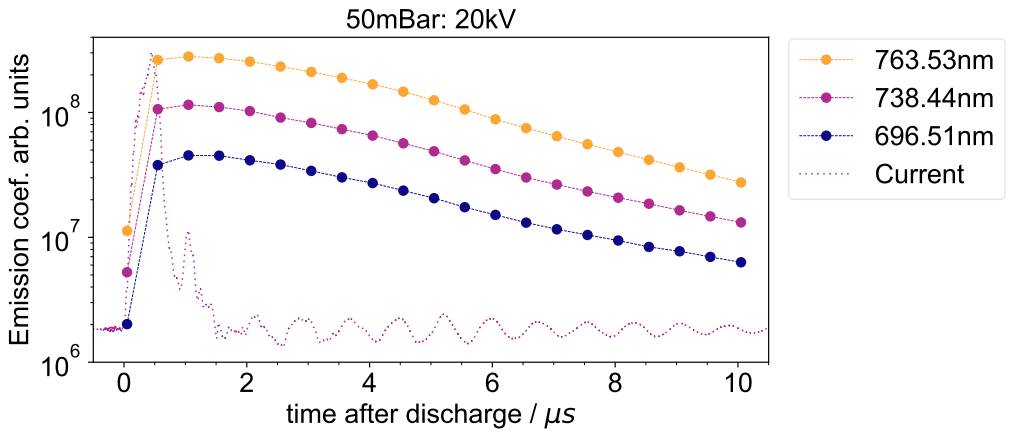

Figure 5.3: Emission coefficient for three example emission lines as indicated in the legend for 50 mbar and 20 kV together with the discharge current.

only. It was therefore necessary to include this reflection to get meaningful values for the double peaks. As this approach is however only an estimation it can not be guaranteed that it models the situation accurately. Since double peaks have more free parameters to fit, it will also affect them more strongly and add some systematic uncertainty to them.

The emission coefficients were again obtained by integrating the fits and the result for three wavelengths are shown in Fig. 5.3. This shows that the intensity increases strongly during the discharge and also slightly further until the current reflection (around 1 µs). After that, the emission of the selected emission lines decreases quite exponentially.

5.2 Choice of Analysis Method

5.2.1 Requirements for LTE

The electron density in argon was not directly measured because there was no reliable spectral analysis for argon in this parameter region and no hydrogen was added. The results of an electron density measurement of argon doped with 5 % hydrogen in a comparable setup (40 mbar buffer pressure, 20 kV, 33 mm cell) is shown in Fig. 5.4 to give a rough estimate. The density peak from this measurement has a value of around $2 \times 10^{17}\,\mathrm{cm}^{-3}$ and decreases within 10 µs to approximately $4 \times 10^{15}\,\mathrm{cm}^{-3}$.

To check the possible existence of LTE we use the first resonance transition of argon ($1s_4 \rightarrow$ gs, $\Delta E_{ul} = 11.62\,\mathrm{eV}$) for Eq. (2.12). As only argon neutral lines were measured, the Gaunt factor for neutral atoms was used in Eq. (2.12) and we obtain for example a value of $n_e \geq 1.9 \times 10^{18}\,\mathrm{cm}^{-3}$ for 2 eV. For a temperature range of 0.1 eV to 10 eV the results are shown in Fig. 5.4b. Also in argon the required electron density is too high to reach complete LTE and if the condition would again be relaxed by an order of magnitude for optically thick conditions of

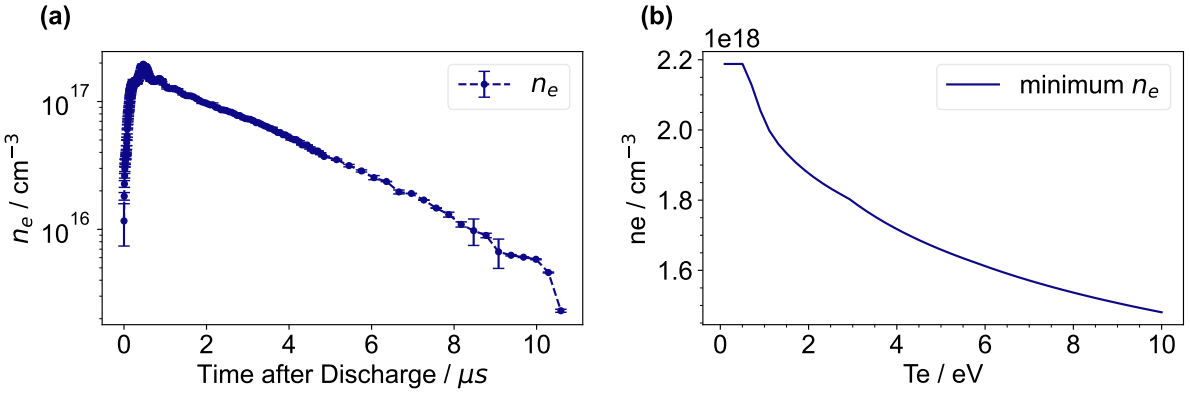

Figure 5.4: (a) Electron density of an argon plasma doped with 5 % hydrogen (backing pressure 40 mbar, 20 kV) measured in a 33 mm capillary with with laser interferometry as described by (Garland et al. 2021). **(b)** Minimal required electron density calculated with Eq. (2.12) and the Gaunt factor of Fig. 2.1 for an electron temperature range of 0.1 eV to 10 eV.

transitions to the ground state, then the electron density might only reach LTE in the beginning (provided that this density measurement is representative enough). Hence, it follows also for the argon measurements that complete LTE is unlikely.

5.2.2 Requirements for Partial LTE

As introduced in Section 2.4.3 the criteria for neutral argon are more unreliable than for hydrogen, because they are usually not derived for neutral argon (compare Table 2.1), only Fujimoto et al. 1990 stated that their criterion for recombining plasmas should also be valid for other neutrals as argon. Sometimes these criteria are however applied as an approximation with the effective quantum number n_{eff} (Aparicio et al. 1999; Lao et al. 2002). The average effective quantum number of the relevant upper $2p$ levels of the transitions can be calculated from Eq. (2.28) with the weighted ionization energy for all Paschen 2p levels as: $E_{\text{ioniz}} - E_{2p} = E_{\text{ioniz}} - \sum_j E_j g_j / g_{2p}$, with the ionization energy of argon E_{ioniz}, the degeneracy g_j and energy E_j for every energy level j and $g_{2p} = \sum_j g_j$ (Kimura et al. 1985). With this calculation we obtain an effective principal quantum number of $n_{\text{eff}} = 2.3$ for the argon 2p levels.

Figure 5.5 shows the results for the pLTE criteria proposed in different studies (Section 2.4.3, compare also Section 4.5.1) for $n_{\text{eff}} = 2.3$ of the argon $2p$ levels. The required electron density is, compared to hydrogen, roughly one order of magnitude larger for the ionisation balance criteria (Fig. 5.5a). This requirement would only be violated at the end of the electron density evolution of Fig. 5.4. For a completely recombining plasma (Fig. 5.5b) the requirements at low temperatures are again significantly higher and minimum temperatures of 1.3 eV are required (Eq. (2.24)). As the discharge plasma is expected to have a significant recombining character,

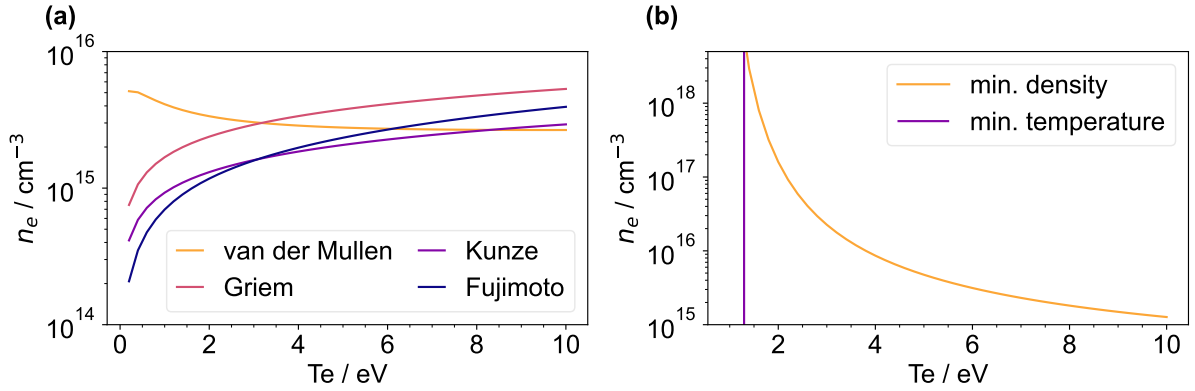

Figure 5.5: The pLTE requirements for neutral argon levels with $n_{\text{eff}} = 2.3$. **(a)** According to van der Mullen 1990 with (Eq. (2.21)), Griem 1963 with Eq. (2.16), Kunze 2009 with Eq. (2.18) and the ionization balance criterion of Fujimoto et al. 1990 with Eq. (2.22). **(b)** Fully recombining plasma according to Fujimoto et al. 1990 with Eq. (2.26) and the minimum required electron temperature of 1.3 eV from Eq. (2.24).

the required electron density should also be shifted towards the high estimate of Eq. (2.24).

Compared to hydrogen the likelihood for argon not to be in pLTE is larger, because the required electron densities are higher and because the pLTE criteria in Fig. 5.5 are only estimates for argon. Only Fig. 5.5b was considered by Fujimoto et al. 1990 to be also valid for other neutral atoms such as argon. Since the pLTE assumption simplifies the analysis and could be valid, at least at the highest electron densities, we will start with this analysis.

5.3 Temperature Analysis with Boltzmann Plots

Proceeding with the same analysis as for hydrogen, the Boltzmann plots for argon are shown in Figs. 5.6 and 5.7. The error bars are omitted in Fig. 5.6 for clarity, but shown in Fig. 5.7 for three time steps. Figure 5.8 shows the resulting electron temperatures for those Boltzmann plots.

In Fig. 5.8 we immediately recognize that the increase of temperature during the time evolution is unrealistic compared to the result we saw in hydrogen (Fig. 4.7). For these plots the temperature also reached negative values at late times after the discharge, which is impossible and thus they were, together with temperatures that have, including the error bars, values larger than 15 eV, omitted in Fig. 5.8. The temperature obtained from these plots is in the region with the best fit quality between 2 µs to 4 µs (see also Fig. 5.9) at around 2.2 eV ± 1.5 eV. The uncertainties for the temperature are not smaller than 60 % to 70 % and prohibitively large for later time steps.

From Fig. 5.6 we already see that the data does not agree closely with the required linear fit and the temporal evolution of the measured lines shows a very systematic pattern. During

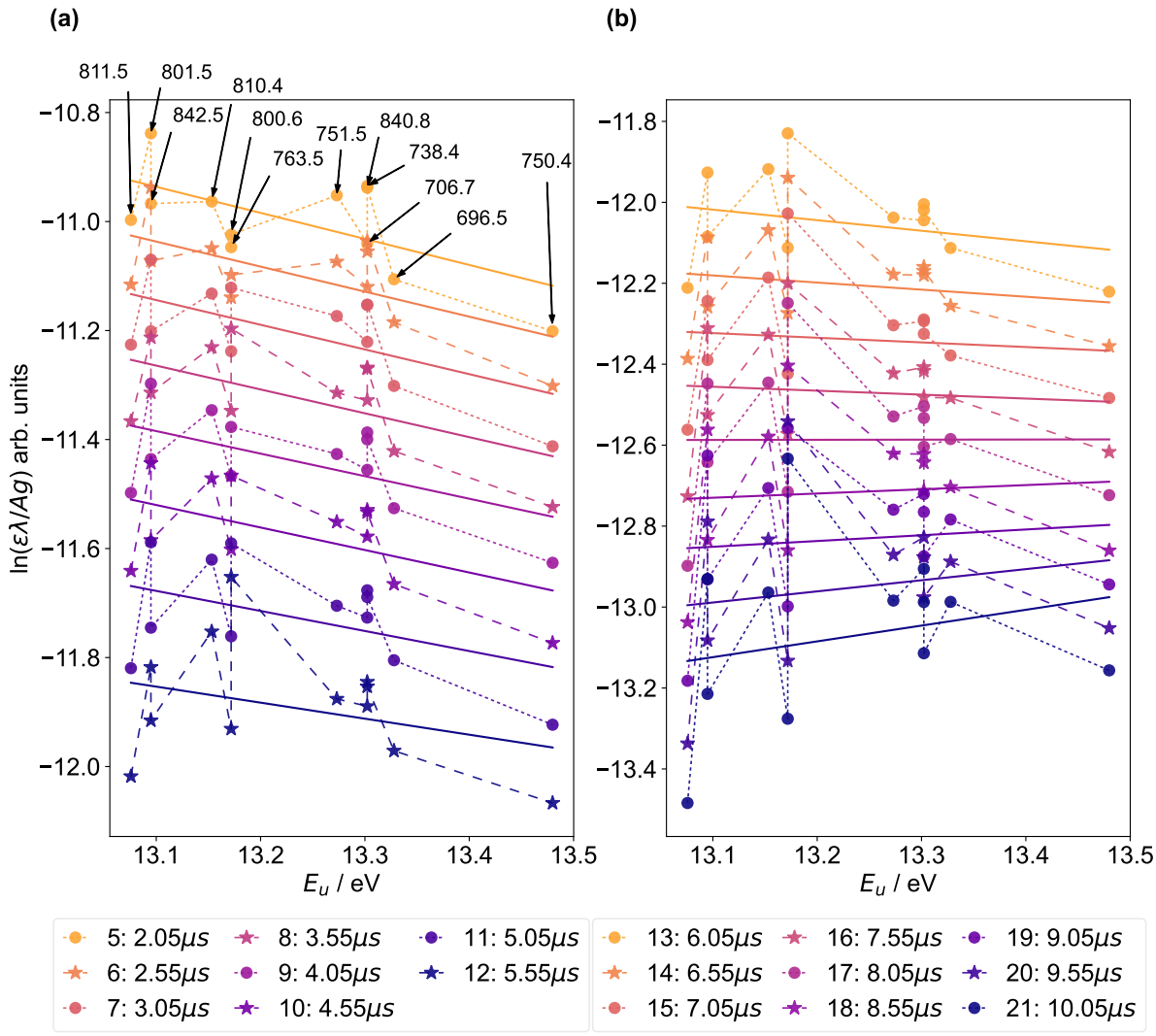

Figure 5.6: **(a)** and **(b)** Boltzmann plots from 2.05 µs to 10.05 µs after the discharge. For clarity error bars are omitted and successive time steps labelled with alternating markers. The color scale reflects

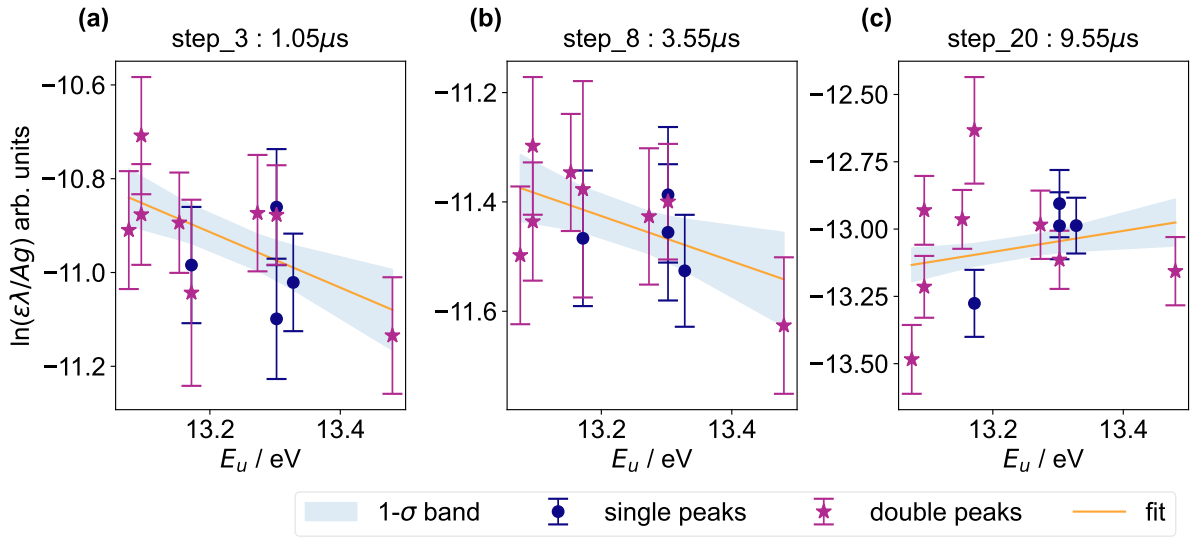

Figure 5.7: **(a)** - **(c)** Boltzmann plots for argon and different time steps after the discharge. Error bars and weighted linear fits with uncertainty bands are also plotted. A distinction was made between double and single peaks as indicated in the bottom legend.

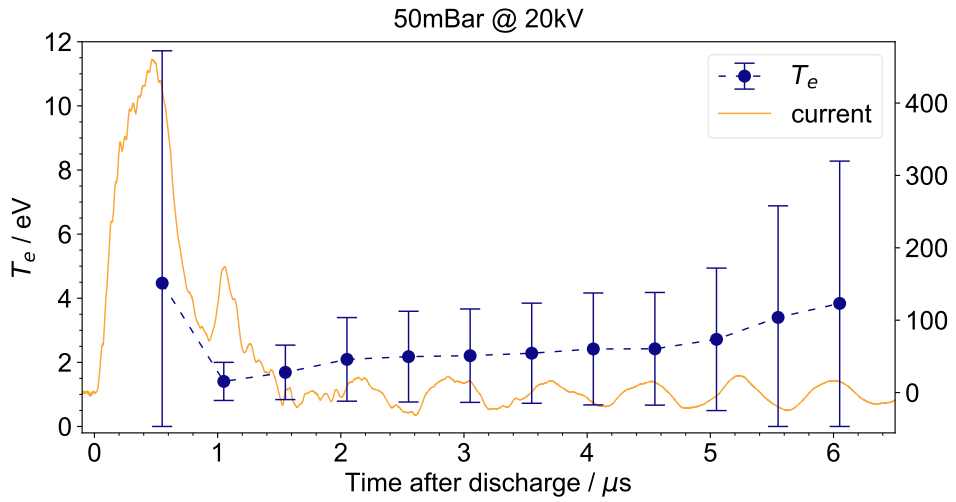

Figure 5.8: Electron temperature of the argon plasma at 50 mbar buffer pressure and 20 kV as the result of of the Boltzmann plot in Figs. 5.6 and 5.7. Error bars larger than 15 eV and negative temperatures have been omitted in these plots.

the first time steps ($t \leq 0.55\,\mu s$) some lines are more difficult to fit because additional (higher excited) lines, that affect the lines under investigation, are present (Figs. 5.2e and 5.2g). This makes the data earlier than 0.55 µs more unreliable which is also reflected in the large uncertainty. The start of the systematic evolution corresponds approximately to the onset of the decay of the emission coefficients in Fig. 5.3 after an initial rise and plateau like-phase. This corresponds also to the time when emission lines from higher excited levels have disappeared, such that the unsystematic evolution in the beginning is most likely the result of difficult fitting procedures. The spread of the data points is also increasing with time and the slope turns positive, resulting first in large and finally negative temperatures.

The error bars calculated for the data in the Boltzmann plots are shown for three exemplary times in Figs. 5.7a to 5.7c and show that these are much larger than the systematic pattern visible in Fig. 5.6. These error bars should overestimate the actual error of these data points as will be discussed subsequently, but at intermediate time steps (Fig. 5.7b) they could explain the spread in the data.

5.4 Measurement Uncertainties

A problem with the measured argon lines could already be the difference in the energies of the involved upper levels of the emission lines. This energy difference should be as high as possible, but is with 0.4 eV not especially large for the measured argon lines and increases therefore the susceptibility to errors.

The measurement uncertainties shown in Fig. 5.7 are similar to the uncertainties in the hy-

drogen analysis (Section 4.4) and constitute three major contributions:

- The uncertainty of the fits is after approximately 1 µs in the range of 1 % to 4 %. For earlier times the uncertainty can be larger because of additional emission lines close to the observed lines. The inclusion of these uncertainties alone would only give small error bars in Fig. 5.7 after 1 µs and could not account for the deviations from the linear fit.

- The calibration uncertainties are the same as for the hydrogen analysis (Section 4.4.1) and range from 7 % to 9 %. The calibration uncertainty could however increase in the 800 nm range where the instrument function of the setup allows less radiation to pass (compare Figs. 3.5a and 3.6c), but this was not included with an additional uncertainty. The contribution from the calibration is significant and larger than the systematic deviations in Fig. 5.6.

- The uncertainty from the spontaneous emission coefficients (A_{ul}) for these argon lines is much higher than it was for the hydrogen lines and is estimated to be 7 % to 10 % depending on the individual line (NIST, Kramida et al. 2020). The emission line at 801.5 nm had even 17 % uncertainty. This contribution to the error bars is also significant and larger than the systematic deviations.

The calibration uncertainty should, as discussed in Section 4.4.1, also overestimate the real uncertainty. For the uncertainty on the emission coefficients, the NIST database refers to Wiese et al. 1989 where a unified set of transition probabilities based on a critical review and data assembly was established. Wiese et al. 1989 did also not distinguish between relative and absolute scale uncertainties in their final recommended values, however they write about an 'excellent' relative scale of some of the datasets used for their compilation and data assembly. This stated uncertainty will therefore possibly also overestimate the uncertainty on the relative scale. Also a computation of the Boltzmann plots with more recent theoretical calculation of the oscillator strengths (convertible in emission coefficients) by Zatsarinny et al. 2006 showed a similar spread of the data points and thus also indicated that the distribution is not the result of the uncertainties in the emission coefficients. The increasing spread of the data around the fits is also not in favour of problems with the measurement uncertainties because the calibration and the A_{ul} coefficients should be independent of the plasma parameters and also because the fits do not degrade for later times. As deviations are also very systematic this must be caused by uncertainties that are not covered in the Boltzmann plot analysis.

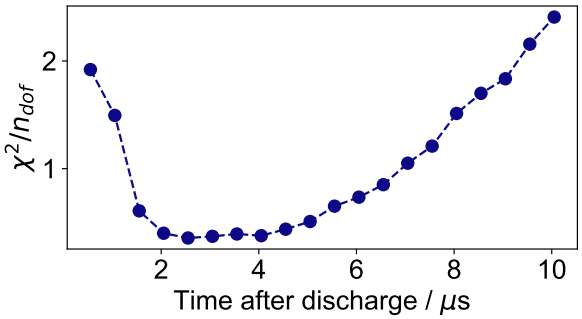

Figure 5.9: The χ^2/n_{dof} values as a measure of the fit quality of the Boltzmann plots during the evolution of the plasma, n_{dof} are the degrees of freedom.

5.5 Model Concept Uncertainties

The increasing spread of the data points in the Boltzmann plots in Fig. 5.6 is also seen in the fit quality in Fig. 5.9, which is best between 2 µs to 4 µs and decreases during the further evolution of the plasma. To explain this systematic in Fig. 5.6 and the fit quality decrease in Fig. 5.9, the uncertainties in the modelling concept should be considered.

5.5.1 Requirements for Partial LTE

Assuming that the resulting temperature from Fig. 5.8 gives at least roughly a reasonable temperature, we can re-evaluate the requirements for pLTE. For steady state conditions (Fig. 5.5a) and electron temperatures around 2 eV the required electron densities are approximately 3×10^{15} cm^{-3} and higher. This is also rarely a problem for the densities in Fig. 5.4 and might only cause deviations from pLTE starting from 9 µs to 10 µs. Comparing this again to the required density for a purely recombining plasma with 2 eV (Fig. 5.5b) yields required densities which may be never realised at this working point. If we assume the real required density to be between both estimates, then it appears to be plausible that the pLTE criteria are not met after a certain time or may be never met and cause the deviations from the linear fit line. It is also reasonable that argon shows stronger deviations from pLTE than hydrogen since the approximated effective principal quantum number for the argon 2p levels is lower.

As we saw in the fit quality in Fig. 5.9 there exists a region where χ^2/n_{dof} is minimal and this is the region where pLTE should exist, if it exists. The decreasing correlation for this measurement after 4 µs is an indication for deviations from pLTE. Deviations in the first 1 µs to 2 µs might not necessarily be caused by deviations from pLTE rather they could also be caused by the high intensity of other lines that obscure the lines under investigation and complicate the fits.

Since the investigation of stationary conditions as in Section 4.5.2 requires reliable electron

density and temperature estimates this condition was not investigated for argon.

5.5.2 Radiation Trapping / Self Absorption

There are a couple of emission lines which share the same upper energy level and thus should also have the same position in the Boltzmann plots if they are not self absorbed (Sections 2.7 and 3.6). In Fig. 5.7 and also Fig. 5.6, the relevant emission coefficients with the same energy of the upper levels (E_u) do not have the same values, although they sometimes agree within the error bars. These error bars could however also overestimate the uncertainty as discussed above. There is a significant difference between lines that share the same upper level as seen in Fig. 5.7 and for some line pairs this increases also with time (Figs. 5.6 and 5.7c). If this is caused by self absorption, then this increase could be due to an increasing population density of the lower energy levels which cause stronger self absorption (while the population of higher energy levels decreases).

Because in the diagnostics laboratory setup only a depth of field of 0.2 mm was imaged with the imaging system, it was previously expected that self absorption is negligible. Instead of self absorption it could also be possible that the reflection is not modelled accurately enough and the difference between lines with the same upper level is increased for double peaks more than for single peaks. The distinction in Fig. 5.7 between double and single peaks lets also suggest that the difference between double peaks increases stronger with time than it does for single peaks. The single peaks at 13.3 eV in Fig. 5.7 (706.7 nm: $2p_3 \rightarrow 1s_5$, 738.4 nm: $2p_3 \rightarrow 1s_4$) appear also to be closer to each other in the Boltzmann plots than the double peaks (compare also Fig. 5.6), but it is difficult to say if this is not related to weaker self absorption of those lines. As for hydrogen (Section 4.5.3), it is uncertain to estimate the strength of self absorption without the population density of the four lower energy levels. If it could be assured that the values in the Boltzmann plots are correct within their uncertainties, then this would indicate self absorption, but with the uncertainties in the modelling of the reflection this is ambiguous.

These uncertainties resulting from deviations from pLTE and self absorption, which can not be covered by the Boltzmann plot method, could explain the results we see and therefore it is useful to consider the implementation of a CRM.

5.6 Implementation of a CRM

A CRM for argon was implemented along the approach described by Graef 2012, which is also similar to those described by Gangwar et al. 2012 and Evdokimov et al. 2017. It models the first 40 excited levels of the 1s, 2p, 3d, 2s, 3p manifolds, as well as the ground states of neu-

tral and singly ionized argon. Additionally an effective level for all levels above 3p and below ionization was added (compare high lying levels in X.-M. Zhu et al. 2010a). For all these levels the processes of electronic excitation and de-excitation, electronic ionization, two-electron recombination and spontaneous emission were included as in Eq. (2.31). Other possibly relevant processes as radiative recombination, self absorption, de-/excitation by atomic collisions or diffusion to the walls were for simplicity not included. By only taking those processes into account the system of equations is linear and can easily be solved. An extended discussion of CRMs (Section 2.5), describing the approach to solve the rate equations, can also be found in Appendix A.

The cross sections for those processes were taken from theoretical calculations of Zatsarinny et al. 2014 because these provide a complete set of cross sections for many levels, whereas experimental measurements contain usually only a limited set of levels and processes. These cross sections are also expected to be the most suitable ones for this model (see L C Pitchford et al. 2013 for a comparison between electron neutral cross sections). For the 3p states, where no cross sections of Zatsarinny et al. 2014 were available, the cross sections of Gangwar et al. 2012 were used. The cross sections were retrieved from the LXCat project database (LXCat 2022; Pitchford et al. 2017), where collections of cross sections are available. Ionization cross sections for the different levels were only available from different authors and were taken for the ground state from Zatsarinny et al. 2014, for ionization out of the 1s level from Ali et al. 2008 and for the remaining levels from Deutsch et al. 2004 (where the expressions of X.-M. Zhu et al. 2010a were used). The inverse processes were calculated using the principle of detailed balance for electronic excitation Appendix A.7.1 and ionization Appendix A.7.2.

This CRM was used to calculate the excited state populations of the argon 2p levels and could reproduced for high electron densities a Boltzmann distribution. The model was not in agreement with benchmark results from a different model of X.-M. Zhu et al. 2010a, but this model was also aimed to model weakly ionized plasmas. In these plasmas additional processes which were not implemented in the current model can become relevant.

5.7 Temperature Analysis with a CRM

The CRM was used to calculate the excited state populations of the argon 2p levels which were then fit to the experimental 2p level distribution. The minimization between data and model was performed as described in Section 3.6 with the 2p level distribution per degeneracy (Eq. (3.3)). The free parameters of the minimization were electron temperature and density and for the minimization the parameter range was restricted to exclude very unrealistic results

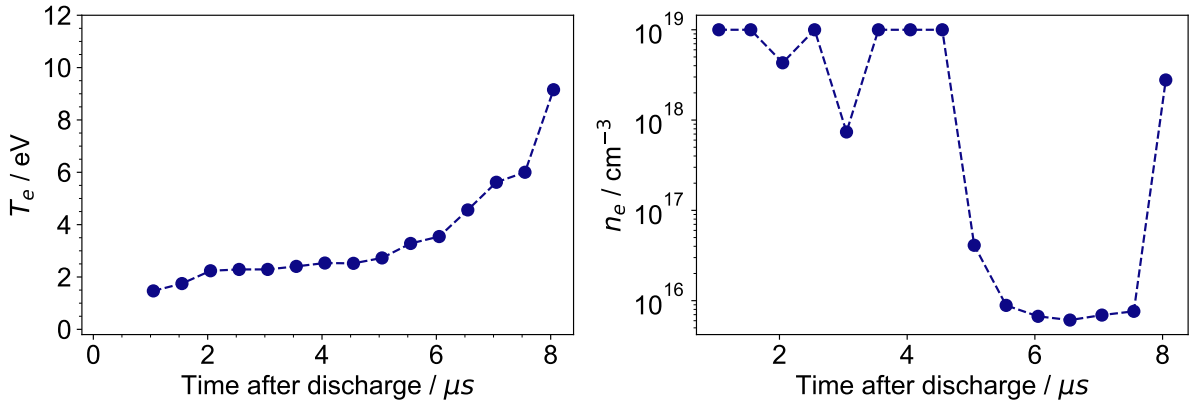

Figure 5.10: Resulting electron temperature **(a)** and density **(b)** calculated with the CRM for argon. The bounds for the minimization were set to 0.01 eV to 30 eV for the electron temperature and 1×10^9 cm^{-3} to 1×10^{19} cm^{-3} for the density. Data points which had temperature values lager than 10 eV were omitted.

to 0.01 eV to 30 eV and respectively 1×10^9 cm^{-3} to 1×10^{19} cm^{-3}. With a buffer pressure of 50 mbar the cell pressure p_{cell} is at maximum 25 mbar, which corresponds to a neutral gas density of $n_g = p_{\text{cell}}/(k_B T) = 6 \times 10^{17}$ cm$^{-}3$ at a neutral gas temperature of $T = 300$ K. To reach the limit of $n_e = 1 \times 10^{19}$ cm^{-3} this would require more than 16 fully ionized ionization stages, which is not possible at this working point (also the temperature should not be much colder).

Figure 5.10 shows the results of this minimization and data points which had temperature values lager than 10 eV were omitted to facilitate the comparison with Fig. 5.8. This is the case within the first 1 µs and after 8 µs. The electron temperature obtained with this minimization is similar to the temperature obtained with the Boltzmann plots in Fig. 5.8, but shows the same unrealistic increase in temperature. This is probably due to the fact that the model converges against a Boltzmann distribution at high electron densities and determines a Boltzmann like distribution to be the most suitable one. On the other hand, the electron density Fig. 5.10a is highly unreliable and the model could in overall not give very realistic results for the plasma parameters and their evolution.

5.8 Modelling Limitations and Uncertainties

Many CRMs studies can be found in the literature (e.g. Iordanova et al. 2007; X.-M. Zhu et al. 2010a; Gangwar et al. 2012; Evdokimov et al. 2017; Durocher-Jean et al. 2019), but CRMs for discharge capillary plasmas which are used in plasma wakefield accelerators and evolve over time from high to lower electron densities (1×10^{17} cm$^{-}3$ to 1×10^{15} cm$^{-}3$) and pressures in the mbar range, were not found. Although Broks 2006 also studied discharge capillaries his model was not suitable to determine the electron temperature. Reasons for the moderate results of the

current model could include:

- Diffusion to the walls is important but was not considered. As the capillary has a small diameter of 1.5 mm the interaction with the walls could be an additional important de-excitation channel.
- Radiative recombination is important, but was not included and the recombining character of the plasma was therefore not correctly modelled.
- In this model self absorption was not included and therefore discrepancies between lines with the same upper level could not be accounted for. More work would be needed to include self absorption and maybe it would be necessary to employ more accurate models (e.g. Durocher-Jean et al. 2019) than which were introduced in Section 2.6.1 for Gaussian line shapes and homogenous plasmas.
- The discrepancy of lines with the same level could also originate from a systematic error in the modelling of the reflection for double peaks (Section 5.1.1) which could not be considered with the model.
- The model is not benchmarked and the implementation could still contain errors.

5.9 Conclusion

The electron temperature for the argon plasma obtained by the Boltzmann plot shows an unphysical increase in temperature with time and results also in negative temperatures. Although it might give, at the region with the best fit quality between 2 µs to 4 µs, temperatures of around 2.2 eV ± 1.5 eV, it is questionable if those results can give the correct scale at all. The increasing systematic deviations from the linear fits in the Boltzmann plots indicate deviations from pLTE, possibly combined with self absorption which makes the Boltzmann plot method inapplicable. The criteria for pLTE in argon can only be considered as estimates, but they suggest that the requirements for pLTE conditions could be violated for the expected electron density. However, this is only the case if the deviations are mainly caused by the recombining character of the plasma (provided that criteria are accurate enough). Beside the pLTE conditions, self absorption could also contribute to the deviations and especially to the difference between emission lines that share the same upper level in the Boltzmann plot. Unfortunately, self absorption could not unambiguously identified because some uncertainties remained in the modelling of the virtual image (reflection) that especially obscured double peaks.

The CRM which was developed to account for these deviations could also not improve the results because it either did not describe all the relevant processes in the discharge plasma correctly, or because it was still not implemented flawlessly. Further improvements and developments of the CRM would need to be considered, but were out of the scope of this thesis.

Chapter 6

Conclusions and Outlook

6.1 Conclusions

First studies have been performed to obtain the electron temperature of hydrogen and argon plasmas which are used in plasma wakefield accelerator experiments. This was possible with the simple method of the Boltzmann plot which allowed the calculation of the electron temperature from OES measurements of multiple emission lines. This method requires the existence of pLTE and the absence of self absorption for the emission lines under investigation. To check these requirements, the LTE and pLTE conditions were thoroughly discussed with the result that larger deviations from pLTE could exist for the measured argon emission lines compared to the measured hydrogen lines. Because pLTE was possible in both plasmas, the Boltzmann plot method could be applied to the hydrogen and argon measurements to explore the electron temperature.

With this method we could determine a maximum electron temperature of 1.60 eV ± 0.40 eV for hydrogen after 0.7 µs after the discharge and found for the specific discharge capillary setup and the relevant working point much smaller uncertainties than in previous studies performed by Garland et al. 2021. In this previous study the electron temperature was also only inferred from electron density measurements and also only calculated for argon. For the argon measurements, this method could not give as plausible values and also resulted, with decreasing electron densities, in clearly un-physically increasing and finally negative electron temperatures. The electron temperature for the best agreement in the Boltzmann plot, which is where pLTE prevails if it prevails, was with 2.2 eV ± 1.5 eV higher than in hydrogen, but because of the un-physical temperature evolution this value should be considered with some caution. An important difference between the hydrogen and argon measurement was also the difference in the energy range of the upper levels which were involved in the measured transitions. For argon this was with 0.4 eV less than half that of hydrogen (0.97 eV) and therefore increased especially for the Boltzmann plots in Argon the susceptibility to errors.

For hydrogen, deviations from pLTE could be possible after the electron density has decreased to approximately half of the maximum density, but this could not be disentangled from the possible self absorption of those emission lines. Self absorption remains for both plasmas

an uncertainty and could not be clearly identified. Possible deviations from pLTE would lead to a faster electron temperature decay and lower temperatures, but should not affect the maximum temperatures. In argon, the measurements showed very systematic deviations which indicated a stronger deviation from pLTE and, or self absorption than in hydrogen. The stronger deviations in argon also agreed with the requirements for pLTE, which were found to be higher than for the hydrogen emission lines. The criteria used to validate the pLTE conditions indicated also that for both plasmas the criteria for ionization balance were mostly met, but the criteria for recombining plasmas were violated and required higher electron densities. This indicated, provided that those criteria are accurate enough, that the recombining character of the discharge plasma could be the decisive contribution to the deviations from pLTE.

The implementation of a CRM, to account for a non-LTE argon plasma was pursued, but could not yield better results and its improvement was out of the scope of this thesis. The modelling could not provide physically realistic results, either because the model did not describe the discharge plasma physics completely, or because it was not benchmarked and still contained errors.

The quality of the measurement data also influenced the accuracy of the results. For the argon measurements the quality was, due to a higher signal yield in the setup, higher than in hydrogen. However, a virtual image, which was postulated to be a capillary reflection, could influence the accuracy of the argon data. This virtual image also prevented us from making clear statements about the presence of self absorption in argon. In the hydrogen measurements, the low signal strength and therefore also the longer integration time, together with a faster plasma dynamics, increased the uncertainty. However, it was inferred from a measurement with longer integration time, that this should not change the calculated temperatures in hydrogen strongly.

In conclusion, the determination of the electron temperature was succesful in hydrogen and less successful in argon. The measurements faced mainly two different types of problems, problems with the data and problems to model the plasma physics of the discharge capillary correctly (as pLTE and self absorption). Despite these uncertainties, the electron temperature in hydrogen could be determined for the first time and in a more direct measurement, with smaller uncertainties than in previous studies and will pave the way for further, more detailed studies on electron temperature characterisation in discharge capillary plasmas for plasma wakefield accelerators.

6.2 Outlook

In further studies and developments the issues with the quality of the data and the model assumptions should be investigated further. To mitigate problems with the data quality the following

measures are proposed:

- Further investigation on the virtual image / capillary reflection (diagnostics laboratory setup Section 3.2.1) should be performed and if possible mitigated with better optics designs and more powerful setups to resolve closely spaced emission lines better.

- The effect of the long integration time for hydrogen, due to the low signal yield, should be investigated further and the integration time kept as low as possible. Alternatively the integrated spectra could be deconvolved properly and fitted with more appropriate peak shape models. To enhance the low light yield, the statistics of the measurements could possibly also be increased further.

- The spectral range of the CCD sensor could be increased to capture the full emission line when the line broadening in hydrogen is very strong or the full range assembled of measurements with different central wavelengths. If the integration time is short, or the peak shape accurately enough deconvolved, this might be dispensable.

The mitigation of problems with the model assumptions would involve further development in the plasma modelling and measurement method:

- It should be investigated again if spectral lines for argon from the transitions $3p \rightarrow 1s$ in the range of 400 nm can be resolved with the setup, or if the setup can be improved to make that feasible. Since these lines originate from higher energy levels, they would increase the energy range in the argon Boltzman plots from around 0.4 eV to approximately 1.5 eV. This significantly larger energy range would not only decrease the susceptibility to errors (e.g. from the spontaneous emission coefficients), but would also improve the Boltzmann plots because higher energy levels suffer less from deviations from pLTE.

- The development of the CRM should be proceeded, missing processes included and benchmarking should also be done. Of prime importance should be the proper inclusion of self absorption, the modelling of diffusion to the capillary walls and recombination processes, as well as testing and benchmarking.

- For some plasmas There are CRMs, or modelling tools, which are available as web applications to calculate population distributions. These tools do not model discharge capillary plasmas, but could give rough estimates which could be used to compare the results of future studies. For hydrogen this is a CRM developed for nuclear fusion by Wünderlich et al. 2020 and electron density and temperature ranges of $n_e = 1 \times 10^8\,\mathrm{cm}^{-3}$ to $1 \times 10^{16}\,\mathrm{cm}^{-3}$, respectively $T_e = 1\,\mathrm{eV}$ to $50\,\mathrm{eV}$. Although the electron densities are lower it might still

be helpful, as it already exists and is accessible. The FLYCHK online modelling tool (Chung et al. 2005) could also give alternative estimations for argon, but works better for ions (private email communication).

- Further investigations on the presence of self absorption would be useful, either with CRMs, where it could be necessary to employ more general absorption profile models (Durocher-Jean et al. 2019) than described in Section 4.5.3, or with measurements (Belmonte et al. 2015, pp. 19–20).

- The Boltzmann plot can also be improved if emission lines of at least two ionization stages are known (e.g. neutral and first ionization stage) and the electron density is available through an independent measurement (e.g. Stark broadening). In this case it is possible to increase the sensitivity of the Boltzmann plot by use of the Saha equation (Zhang et al. 2019). These lines of ionized species can however also have stronger requirements for pLTE.

- It could be possible to improve the argon measurements by doping argon with hydrogen and using, additionally to the argon lines, some hydrogen Balmer lines. The Balmer lines have lower requirements for pLTE and with these hydrogen lines also the energy range of the emission lines in the Boltzmann plot could be increased to up to 1 eV. However, if the admixture of hydrogen is too large this can lead to additional de-excitation mechanisms by atomic collisions such that the de-excitation is not governed by electrons anymore and lead to deviations from pLTE. For low electron densities this mechanism can also already be dominant at admixtures of 15 % (Siepa et al. 2014).

Appendix A

Collisional Radiative Models

To extend the discussion of Section 2.5 based on the work of Graef 2012, we continue to complete the rate balance equations.

A.1 Particle Rate Balance Equations

To describe the whole set of particle balance equations (zeroth moment of the Boltzmann equation Eq. (2.1)) we first consider only one single equation and all possibly relevant processes. The general form of the simplified balance equation from Eq. (2.31) for the density $n(p)$ of level p is:

$$\underbrace{\frac{\partial n(p)}{\partial t}}_{\text{accumulation}} + \underbrace{\nabla \cdot \Gamma}_{\text{efflux}} = \tag{A.1a}$$

$$\underbrace{n_e n_g K(g,p)}_{\text{electron excitation from gs}} \overset{B_g}{-} \underbrace{n(p) n_e K(p,g)}_{\text{electron de-excitation to gs}} + \tag{A.1b}$$

$$\underbrace{n_e \sum_q n(q) K(q,p)}_{\text{electron de-/excitation from q}} \overset{B}{-} \underbrace{n(p) n_e \sum_q K(p,q)}_{\text{electron de-/excitation to q}} + \tag{A.1c}$$

$$\underbrace{n_e^2 n_+ K(+,p)}_{\text{two electron recombination}} \overset{S}{-} \underbrace{n(p) n_e K(p,+)}_{\text{electron induced ionization}} + \tag{A.1d}$$

$$\underbrace{\sum_l n(l) B(l,p) \rho_\nu}_{\text{absorption}} \overset{P_l}{-} \underbrace{n(p) \sum_l \Big[A(p,l) + B(p,l) \rho_\nu \Big]}_{\text{emission (spont. + stim.)}} + \tag{A.1e}$$

$$\underbrace{\sum_u n_u \Big[A(u,p) + B(u,p) \rho_\nu \Big]}_{\text{cascade (spont. + stim.)}} \overset{P_u}{-} \underbrace{n(p) \sum_u B(p,u) \rho_\nu}_{\text{photo excitation}} + \tag{A.1f}$$

$$\underbrace{n_e n_+ \Big[K_{\text{rad}}(+,p) + B(+,p) \rho_\nu \Big]}_{\text{radiative recombination (spont. + stim.)}} \overset{P_+}{-} \underbrace{n(p) B(p,+) \rho_\nu}_{\text{photo ionization}} \tag{A.1g}$$

Where the left hand side of the equation describes accumulation and transport and the right hand side the various collisional and radiative processes that lead to population or depopulation of p. The terms on the right hand side are grouped into so called proper balances (see van der Mullen 1990), such that every process is grouped with its reverse process. Those balances

are identified with a superscript over the minus and according to Section 2.2.1 these are the Boltzmann balance B for electronic de-/excitations, the Saha balance S for ionization and two electron recombination and the Planck balance P for emission and absorption. The Boltzmann and Planck balances are split into different parts, B_g for the equilibrium with the ground state and P_l, P_u, P_+ for the Planck equilibrium with the lower l, upper u and continuum $+$ levels respectively. The complete notation is:

- **levels:** p for the level in balance, q for any other level with $q \neq p$, g for the ground state, l for a level lower than p, u for a level higher than p and $+$ for the ionization continuum.
- **coefficients:** K for the rate coefficient for electron induced collisions for example from level q to p ($K(q,p)$), $A(p,l)$ for the transition probability for spontaneous decay from level p to l, $B(p,u)$ for absorption and $B(u,p)$ for stimulated emission.
- **others:** Γ for the efflux, n_e for the electron density and ρ_ν for the spectral energy density in $\mathrm{Jm^{-3}Hz^{-1}}$.

If one of the proper balances in Eq. (A.1) is not in equilibrium this must be compensated by other processes which can lead to accumulation, transport or to the disequilibrium of another balance. As introduced in Section 2.2.1 the Planck balance is in laboratory plasmas usually in disequilibrium and therefore its often replaced by an effective emission coefficient A^*, for example for P_l:

$$n(l)B(l,p)\rho_\nu - n(p)\Big[A(p,l) + B(p,l)\rho_\nu\Big] \equiv -n(p)A^*(p,l). \tag{A.2}$$

The other Planck balances can be replaced in an analogue way.

A.1.1 Matrix Notation

As we have many equations as Eq. (A.1) (one for every level) we want to cast this in a matrix and vector notation. First, we reorder the terms of a single rate balance equation in populating and destructing terms. For a level p we define the populating frequency F by collisional and radiative contributions from the atomic system as

$$F(q,p) = n_e K(q,p) + A^*(q,p), \tag{A.3}$$

where $q \neq p$. For the contributions from the ionic system by recombination we define

$$F(+,p) = n_e^2 K(+,p) + n_e K_{\mathrm{rad}}(+,p). \tag{A.4}$$

Combining both contributions gives the production P of level p as:

$$P(p) = \sum_{q \neq p} n(q) F(q,p) + n_+ F(+,p) \tag{A.5}$$

and in an analogue way the destruction D of level p

$$D(p) = \sum_{q \neq p} F(p,q) = n_e \sum_{q \neq p} K(p,q) + \sum_{p \neq q} A^*(p,q). \tag{A.6}$$

With this definitions we write Eq. (A.1) as

$$\underbrace{\frac{\partial n(p)}{\partial t}}_{\text{accumulation}} + \underbrace{\nabla \cdot \Gamma}_{\text{efflux}} = \underbrace{P(p)}_{\text{production}} - \underbrace{n(p) D(p)}_{\text{destruction}}, \tag{A.7}$$

which is expressed even more general as

$$\underbrace{T(p)}_{\text{transport}} = \underbrace{S(p)}_{\text{source}}. \tag{A.8}$$

In a matrix vector notation this can be written as

$$\mathbf{T} = \mathbf{S} = \boldsymbol{F}\mathbf{n}, \tag{A.9}$$

where the elements of the transport vector $\mathbf{T}$ have the form of the left hand side of Eq. (A.7), $\mathbf{S}$ is the source vector, $\boldsymbol{F}$ the transition-matrix containing the populating and depopulating frequencies and $\mathbf{n}$ the vector containing all level densities. This frequency matrix describes how the agents as electrons and photons act on the level densities with populating and depopulating processes. The elements of this matrix $\boldsymbol{F}$ are defined as:

$$F_{pq} = F(q,p) \qquad \text{with } p \neq q, \text{ incl. ion} \tag{A.10}$$

$$F_{pp} = -F(p,p) \equiv -\sum_{q \neq p} F(p,q) \qquad \text{diagonal elements.} \tag{A.11}$$

The diagonal elements F_{pp} correspond to the total destruction rate and therefore to the depopulation of level p (the sign is analogue to Eq. (A.7)) and the non-diagonal elements to the populating processes. It is also important to pay attention to the naming convention of the matrix: According to the mathematical convention F_{pq} is the element on row p at column q but the CRM convention is the other way round because the matrix vector multiplication results in elements $F_{pq} n_q$ corresponding to the depopulation of q in favour of p which is $F(q,p)$.

The system of equations will be linear as long as only electrons and photons are considered because they can be treated as external agents which cause the transitions. If other processes are included, which for example depend on the level density itself, the system will become also non-linear.

A.2 Local Chemistry and Transport

As in the quasi steady state solution (Section 2.1.1) we can compare the timescales for chemistry and transport related processes. The frequencies for the destruction of species by transport are usually up to 1×10^4 Hz whereas the destruction frequencies for chemistry processes can range up to 1×10^8 Hz. The destruction frequencies for excited species are usually also much larger than their transport frequencies while the destruction frequencies for the atomic and ionic ground states are on the order of the transport frequencies. In the following levels that have a high destruction frequency compared to their transport frequency are called, according to Graef 2012, 'local chemistry' (LC) levels and levels that have a destruction frequency comparable to their transport frequency 'transport sensitive' (TS) levels. This approach is comparable to the QSSS approach. Local chemistry levels will in general also have low densities compared to the TS species because of their high destruction frequencies and therefore TS species will serve as the density reservoirs for the LC levels.

A.3 The Tasks of Collisional Radiative Models

The transport and configurational aspects of a plasma are only described in a simplified form in CRMs and it is also not the task of a CRM to model these aspects. The application of a CRM is to model the 'chemistry' in a plasma. In this work, the CRM is also restricted to the atomic species only, excitations of ionic levels are not considered. In this context the atomic ground state and the ionic ground state are denoted as the low energy and high energy entry to the excitation space of the excited levels (LC) in between. The density of the entry levels determines the population density of the internal LC levels through an excitation flow by collisional and radiative processes. The result of these processes is an atomic state distribution function (ASDF) which is dependent on parameters as the electron density and temperature.

To simplify the construction of this ASDF not all levels of the atomic system must be taken into account and usually the number of levels is restricted to only those which have a significant effect on the result. This can be achieved by using cut-off procedures (van der Mullen 1990), where levels above a certain cut-off level are simplified, or effective levels, which group multiple high lying levels into single levels (X.-M. Zhu et al. 2010a).

A.4 Two Level Systems

The simplest formulation of a CRM is a two level system that consists of only two TS entry levels (the ground states of the atom and ion) and the LC levels in between. In this framework

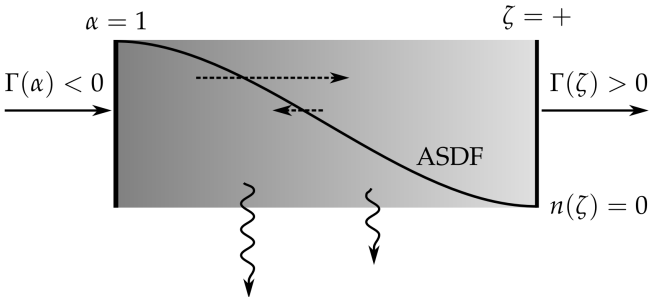

Figure A.1: Sketch of a fully ionizing two level system (Graef 2012, p. 20). The lower entry level (TS) is the atomic ground state $\alpha = 1$ and the high energy entry the ion ground state $\zeta = +$. The density of the ionic ground state is set to zero $n(\zeta) = 0$ and the ASDF is shown as a black solid line. The efflux at either the low or high energy side is denoted as Γ, the dashed arrows indicate electronic excitations and de-excitations and the wavy lines radiation loss.

it is possible to distinguish between two extreme cases, the fully ionizing and the fully recombining system. In the following the atomic ground state will be denoted as α, the ionic ground state as ζ and the efflux again as Γ. The plasma will also be considered to be in a steady state (Section 2.1.1) and optically thin (Section 2.6.1).

Ionizing System

In a fully ionizing system the density of the ion ground state is set to zero $n(\zeta) = 0$, which can in reality be achieved if the efflux by strong diffusion of ions and electrons at the high energy side is extremely large. The influx on the low energy side must be of the same absolute value to sustain the efflux on the high energy side. Here the sign convention for efflux is positive if the transport is outwards and negative if it is inwards, hence $\Gamma(\zeta) = -\Gamma(\alpha)$. An ionizing system with the corresponding ASDF is shown in Fig. A.1. The electronic excitation and de-excitation kinetics (dashed arrows) create a net ionization flux through the system that goes along with the production of radiation (wavy lines).

In this simple case and because the system of equations is treated as linear, the population of an internal level i (LC level) can be expressed by contributions from the ground state α only:

$$n^{\alpha}(i) = R_{i\alpha} n(\alpha), \tag{A.12}$$

where $R_{i\alpha}$ is the function that relates the internal level densities to the ground level. This function depends on all excitation and de-excitation processes and therefore also strongly on the properties of the electron gas like electron density n_e and electron temperature T_e.

Recombining System

The opposite case is a fully recombining system where the density of the ground state is set to zero $n(\alpha) = 0$ (Fig. A.2). For a recombining system the efflux at the low energy side will be

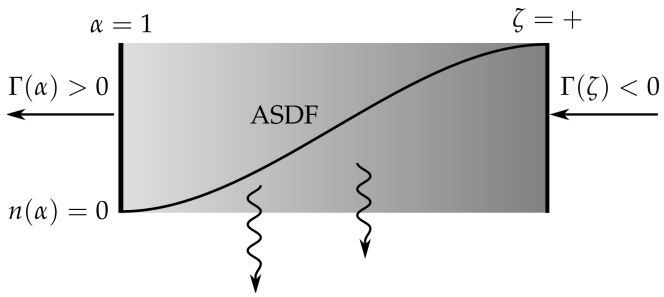

Figure A.2: Sketch of a fully recombining system (Graef 2012, p. 20). The labelling is the same as in Fig. A.1 and the density of the atomic ground state is set to zero, $n(\alpha) = 0$.

positive and the efflux on the high energy side negative, which will result in an influx to the system of internal levels from the high energy side. For the recombining system the density of an internal level is equivalently determined by

$$n^{\zeta}(i) = R_{i\zeta} n(\zeta). \tag{A.13}$$

A.5 Multiple Level Systems

To create a more general model, ionizing and recombining systems are combined such that the density of an internal level $n(i)$ is the sum over all density contributions $n^{\xi}(i)$ from different entry levels ξ (not restricted to only two entry levels)

$$n(i) = \sum_{\xi} n^{\xi}(i) = \sum_{\xi} R_{i\xi} n(\xi). \tag{A.14}$$

This can also be formulated in a matrix-vector notation for multiple internal levels:

$$\mathbf{n}^{l} = \boldsymbol{R}^{lt} \mathbf{n}^{t}, \tag{A.15}$$

where the superscript l designates LC species and t TS species. The matrix $\boldsymbol{R}^{lt}$ translates between the TS level densities and the LC level densities. This matrix $\boldsymbol{R}^{lt}$ can be used to determine the ASDF.

A.6 Determination of the ASDF

We have seen two different matrix notations so far: the generalized form of the zeroth Boltzmann moment with the coupled set of balance equations Eq. (A.9)

$$\mathbf{T} = \mathbf{S} = \boldsymbol{F}\mathbf{n}.$$

and the relation between LC levels and TS levels in Eq. (A.15)

$$\mathbf{n}^l = \boldsymbol{R}^{lt}\mathbf{n}^t.$$

To calculate the ASDF, hence the vector $\mathbf{n}$ in Eq. (A.9) we express $\boldsymbol{R}$ in terms of $\boldsymbol{F}$ which contains the rates for populating and depopulating processes. For that purpose is useful to re-arrange the matrix such that levels for which the transport can be neglected (LC levels) and which are sensitive to transport (TS levels) are grouped together. This groups $\boldsymbol{F}$ into four blocks and $\mathbf{S}$ and $\mathbf{n}$ into two sub-vectors of TS and LC levels:

$$\begin{pmatrix} \mathbf{S}^t \\ \mathbf{S}^l \end{pmatrix} = \begin{pmatrix} \mathbf{S}^t \\ 0 \end{pmatrix} = \begin{pmatrix} \boldsymbol{F}^{tt} & \boldsymbol{F}^{lt} \\ \boldsymbol{F}^{tl} & \boldsymbol{F}^{ll} \end{pmatrix} \begin{pmatrix} \mathbf{n}^t \\ \mathbf{n}^l \end{pmatrix} \tag{A.16}$$

again with t and l for TS and LC sensitive levels. Here the source $\mathbf{S}^l$ for the LC levels was set to zero due the QSSS (Section 2.1.1). With that notation $\boldsymbol{F}^{ll}$ contains only processes between LC levels and for example $\boldsymbol{F}^{lt}$ only processes from LC to TS levels.

To obtain the ASDF of the LC levels we only need to solve the lower line of the matrix representation for $\mathbf{n}^l$:

$$\mathbf{n}^l = \underbrace{-\left(\boldsymbol{F}^{ll}\right)^{-1}\boldsymbol{F}^{tl}}_{\boldsymbol{R}^{lt}}\mathbf{n}^t, \tag{A.17}$$

and identify $\boldsymbol{R}^{lt} = -\left(\boldsymbol{F}^{ll}\right)^{-1}\boldsymbol{F}^{tl}$. To obtain the whole ASDF including TS levels we can add the unity matrix

$$\mathbf{n} = \begin{pmatrix} \boldsymbol{I} \\ -\left(\boldsymbol{F}^{ll}\right)^{-1}\boldsymbol{F}^{tl} \end{pmatrix}\mathbf{n}^t. \tag{A.18}$$

A.7 Transition-matrix

The transition matrix $\boldsymbol{F}$ contains all the processes introduced in Eq. (A.1) and the elements of this matrix are frequencies which are defined such that their multiplication with the density $n(j)F(j,k)$ is the number of transitions $j \to k$ per unit time. The processes which are included in this matrix will be described in the following.

A.7.1 Electronic Excitation and De-excitation

If an electron e collides with another particle X in state p it can increase the particles energy by the reaction

$$X(p) + e + (E_{pq}) \overset{K(p,q)}{\to} X(q) + e, \tag{A.19}$$

if it reaches the threshold energy ($E_{pq} = E_q - E_p > 0$) for the excitation to the energy state q. The rate coefficient $K(p,q)$ is

$$K(p,q) = \langle \sigma v \rangle = \int_{E_{pq}}^{\infty} \sigma_{pq}(E') v(E') f(E') dE', \tag{A.20}$$

where σ is the cross section for this reaction, $f(E)$ the EEDF and $v(E) = \sqrt{2E/m_e}$ the electron velocity with electron mass m_e (see also Appendix A.8). Cross sections are either available from experiments or calculated from theoretical models. If the EEDF is Maxwellian it can be described solely by the electron temperature and the rate coefficient can also be expressed by a function with usually exponential dependence on T_e.

The rate for electronic de-excitation (backward process) can be calculated from the rate for electronic excitation (forward process) by employing the principle of detailed balance (in LTE the number of forward processes equals the number of backward processes, see Section 2.2.1 and Eq. (2.5)):

$$n_e n^B(p) K(p,q) = n_e n^B(q) K(q,p),$$

where n_e is the electron density and n_p^B and n_q^B the level density of level p respectively q according to the Boltzmann distribution (Eq. (2.4))

$$\frac{n^B(q)}{g_q} = \frac{n^B(p)}{g_p} \exp\left(-\frac{E_{pq}}{k_B T_e}\right). \tag{A.21}$$

Where g is the degeneracy of the respective level and k_B the Boltzmann constant. This leads to the relation

$$K(p,q) = \frac{g_p}{g_q} K(q,p) \exp\left(-\frac{E_{pq}}{k_B T_e}\right) \tag{A.22}$$

between rate coefficients for forward and backward processes. Strictly, this only applies for thermodynamic equilibrium, but as cross sections are independent of the existence of thermodynamic equilibrium it is also possible to relate the cross section for forward and backward processes by the principle of detailed balance to obtain a generally valid relation:

$$\sigma_{qp} = \frac{g_p}{g_q} \frac{E + E_{pq}}{E} \sigma_{pq}(E + E_{pq}). \tag{A.23}$$

A.7.2 Ionization and Recombination

If the energy of an electron reaches the ionization threshold E_{p+} it can ionize the the particle X in state p via the process

$$X(p) + e + (E_{p+}) \overset{K(p,+)}{\rightarrow} X(+) + e + e \tag{A.24}$$

where $K(p,+)$ is the rate coefficient for ionization. Analogously to Eq. (A.20) this rate coefficient for ionization can be calculated with an appropriate ionization cross section.

The reverse process of electronic excitation is two electron recombination which is ruled by the Saha balance (compare Eq. (A.1d)) and the reverse process of photo ionization, radiative recombination (compare Eq. (A.1g)). To find a relation between ionization and two electron recombination we require again thermodynamic equilibrium and use the Saha balance Eq. (2.6) in a slightly different ordering

$$\frac{n(p)}{g_p} = \frac{n^S(p)}{g_p} = \frac{n_e}{g_e}\frac{n(+)}{g_+}\left(\frac{h^2}{2\pi m_e k_B T_e}\right)^{3/2} \exp\left(\frac{E_{p+}}{k_B T_e}\right). \tag{A.25}$$

With the principle of detailed balance

$$n_e n(+) K(+,p) = n_e n^S(p) K(p,+). \tag{A.26}$$

we obtain together with the degeneracy of electrons $g_e = 2$ the recombination rate

$$K(+,p) = K(p,+)\frac{g_p}{2g_+}\left(\frac{h^2}{2\pi m_e k_B T_e}\right)^{3/2} \exp\left(\frac{E_{p+}}{k_B T_e}\right). \tag{A.27}$$

Radiative recombination takes place via the process

$$X(+) + e \overset{K_{\text{rad}}(+,p)}{\rightarrow} X(p) + h\nu_{p+} \tag{A.28}$$

and the required rate coefficient can be obtained by (van der Mullen 1986)

$$K_{\text{rad}} = \frac{n^S(p)}{n_e n(+)}\gamma Z^4 \frac{1}{\mathsf{p}_p}\int_{\epsilon_p}^{\infty}\frac{\exp(-\epsilon)}{\epsilon}P(\epsilon/\epsilon_p)d\epsilon \tag{A.29}$$

where Z is the core charge number, p_p the (effective) principal quantum number and P the Gaunt factor that can be approximated by 1 in this formula. The quantities ϵ_p and γ are defined as

$$\epsilon_p = \frac{E_{p+}}{k_B T_e}, \qquad \gamma = \frac{8\alpha^4 c}{3\pi\sqrt{3}a_0}. \tag{A.30}$$

with the fine structure constant α and the Bohr radius a_0.

A.7.3 Radiation

Radiative transitions due to spontaneous emission, absorption or stimulated emission can cause transitions between energy levels. These processes are for an upper level u and a lower level l: spontaneous emission

$$X(u) \overset{A(u,l)}{\rightarrow} X(l) + h\nu_{ul}, \tag{A.31}$$

absorption

$$X(l) + h\nu_{ul} \overset{\rho_\nu B(l,u)}{\rightarrow} X(u) \tag{A.32}$$

and stimulated emission

$$X(u) + h\nu_{ul} \overset{\rho_\nu B(u,l)}{\rightarrow} X(l) + h\nu_{ul} + h\nu_{ul}. \tag{A.33}$$

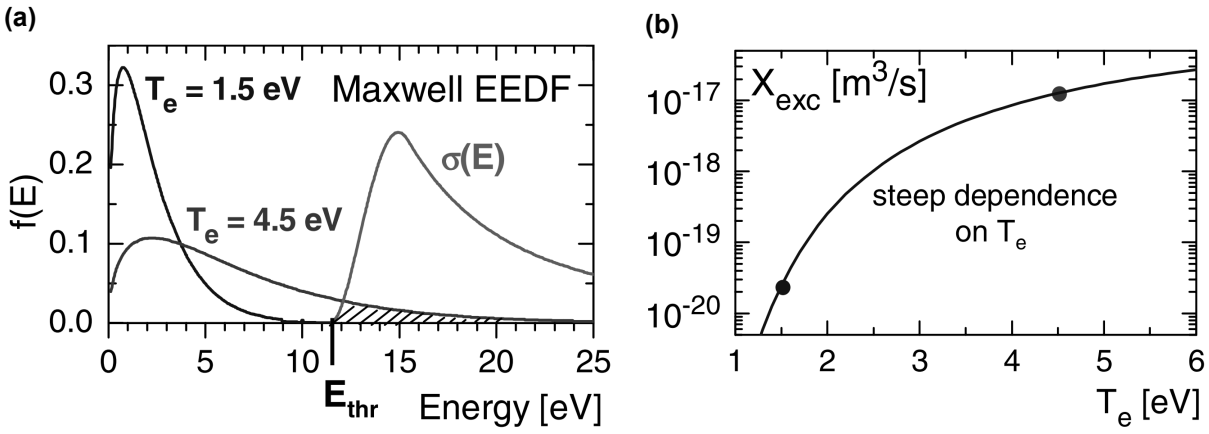

Figure A.3: Figures taken from Fantz 2006. **(a)** Convolution of a Maxwellian EEDF at two different temperatures $T_e = 1.5\,eV$ and $T_e = 4.5\,eV$ with a typical cross section for electron impact excitation $\sigma(E)$. The shaded area is the overlap of the convolution. **(b)** Resulting excitation rate coefficient X_{exc} of **(a)**. The black dots represent the temperature values from **(a)**.

Here ν_{ul} is the photon frequency $\nu_{ul} = c/\lambda_{ul}$, ρ_ν the spectral energy density and $A(u,l)$, $B(l,u)$ and $B(u,l)$ the Einstein coefficients for spontaneous emission, absorption and stimulated emission respectively.

Because absorption and stimulated emission are non-local they are difficult to include into a CRM and to approximate these processes the escape factor as introduced in Section 2.6.1 is commonly used to employ an effective emission coefficient Eq. (A.2).

A.8 Temperature Dependence of Rate Coefficients

To exemplify the temperature dependence of rate coefficients we consider now electron impact excitation. The excitation rate is obtained by a convolution of the EEDF with the cross section for the respective excitation process. The result of the convolution is dependent on the electron temperature since the shape of the EEDF itself depends on the electron temperature.

The difference between the convolution of a Maxwellian EEDF with two different temperatures and a typical cross section for electron impact excitation is illustrated in Fig. A.3. This shows the origin of the dependence of the rate coefficients on the electron temperature. Figure A.3b explains that the sensitivity on the electron temperature is strong for EEDFs that are characterized by a temperature below the threshold E_{thr} and gets weaker while approaching the threshold since the change in overlap of EEDF and cross section decreases. In this way the different processes between the energy levels with different thresholds add the temperature dependence to the CRMs.

Appendix B

Wavelength Calibration

The wavelength range was before this study only calibrated at one central wavelength to a fixed range of 48.7 nm independent of the central wavelength of the spectrometer. This wavelength range was used to determine the wavelength axis in the following plots. For the wavelength calibration of the Princeton Instruments spectrometer the wavelengths 532 nm, 650 nm, 666.89 nm, 764.2 nm and 823.16 nm were used. To analyse the expected and measured position on the CCD, the position of the peak on the CCD was shifted by stepping the central wavelength of the spectrometer in 5 nm steps across the CCD range (of every wavelength). Figure B.1b shows 9 different spectrometer central wavelength settings as indicated in the legend for the 650 nm laser. To obtain the observed peak wavelength every spectrum was fit with a pseudo-Voigt model (Figs. B.1c and B.1d). The fits for the laser lines excluded the central region of the peak where the spectrum shows a flat top structure (Fig. B.1c). This analysis yields the observed peak wavelength versus central wavelength as in Fig. B.1a.

According to Yuan et al. 2017 the relation between the pixel p on a CCD at the exit plane of a spectrometer and the wavelength is a third order polynomial function, but for this analysis it was approximated by a linear relation. The spectral range $\Delta\lambda_{\text{real}}$ was therefore obtained from

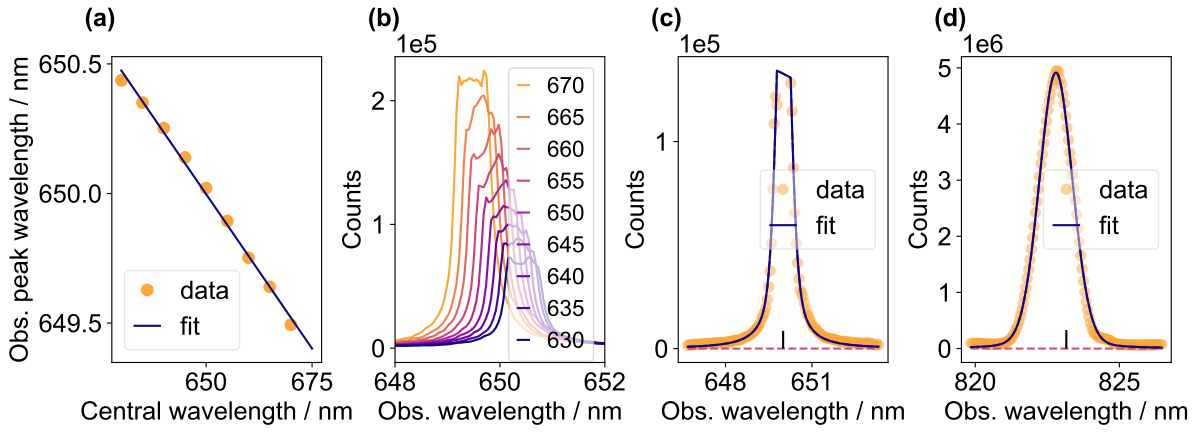

Figure B.1: **(a)** Observed peak position vs. central wavelength for the 650 nm laser line at different central wavelengths. **(b)** Spectra of **(a)** for the central wavelengths indicated in the legend (in nm). **(c)** Example fit of the spectrum at a central wavelength of 650 nm (laser). **(c)** Fit for a Xenon line. The red line at the bottom of **(c)**, **(d)** is the background contribution. The small vertical line at the bottom indicates the theoretical peak position.

the slope of the linear fits (Fig. B.1a) by realizing that:

$$\Delta\lambda_{\text{real}} = \Delta\lambda_{\text{fix}} + \delta_{\text{cwl}} = \Delta\lambda_{\text{fix}} + \frac{\delta_{\text{cwl}}}{\Delta\lambda_{\text{fix}}}\Delta\lambda_{\text{fix}} = \Delta\lambda_{\text{fix}}(1+m), \tag{B.1}$$

where $\Delta\lambda_{\text{real}}$ is the real spectral range, $\Delta\lambda_{\text{fix}}$ the fixed spectral range of 48.7 nm, δ_{cwl} the difference between fixed spectral range and $\Delta\lambda_{\text{real}}$ at a given central wavelength and $m = \Delta y/\Delta x = \delta_{\text{cwl}}/\Delta\lambda_{\text{fix}}$ the slope of the linear fit. By using $\Delta\lambda_{\text{fix}} = 48.7$ it is possible to calculate the spectral range per central wavelength with the result that was shown in Fig. 3.4a.

The wavelength range calibration for the Horiba spectrometer was performed in a simpler way at 4 certain wavelengths (557.0 nm, 587.1 nm, 645.63 nm and 762.0 nm). The spectral range was determined by shifting the emission line to the CCD borders by changing the central wavelength setting at the spectrometer and observing its difference (Fig. 3.4b).

Appendix C

Paschen Notation

With the following tables Paschen notation can be converted in Recah notation or Recah notation in Paschen notation. The tables are taken from Graef 2012, pp. 203–204.

Table C.1: Table for the conversion between blocks in the Recah notation (top row) to Paschen notation (bottom row, italics).

Orbital	Block			
s	4s	5s	6s	7s
	1s	*2s*	*3s*	*4s*
p	4p	5p	6p	7p
	2p	*3p*	*4p*	*5p*
d	3d	4d	5d	6d
	3d	*4d*	*5d*	*6d*

Table C.2: Table for the conversion of levels in the Recah notation (top row, brackets) per orbital and the Paschen notation (bottom row, italics). The prime in the Racah notation denotes the core configuration: $P_{3/2}$ for unprimed, $P_{1/2}$ for primed.

Orbital	Level					
s	$[3/2]_2$	$[3/2]_1$	$'[1/2]_0$	$'[1/2]_1$		
	s_5	s_4	s_3	s_2		
p	$[1/2]_1$	$[5/2]_3$	$[5/2]_2$	$[3/2]_1$	$[3/2]_2$	
	p_{10}	p_9	p_8	p_7	p_6	
	$[1/2]_0$	$'[3/2]_1$	$'[3/2]_2$	$'[1/2]_1$	$'[1/2]_0$	
	p_5	p_4	p_3	p_2	p_1	
d	$[1/2]_0$	$[1/2]_1$	$[7/2]_4$	$[7/2]_3$	$[3/2]_2$	$[3/2]_1$
	d_6	d_5	d'_4	d_4	d_3	d_2
	$[5/2]_2$	$[5/2]_3$	$'[5/2]_2$	$'[5/2]_3$	$'[3/2]_2$	$'[3/2]_1$
	d''_1	d'_1	s''''_1	s'''_1	s''_1	s'_1

Bibliography

Ali, M. Asgar et al. (2008). “Electron impact ionization of metastable rare gases: He, Ne and Ar”. In: *International Journal of Mass Spectrometry* 271.1-3, pp. 51–57. ISSN: 1387-3806. DOI: 10.1016/j.ijms.2007.10.006.

Aparicio, Juan A. et al. (1999). “Measurement of Excitation Equilibrium Departure Evolution in an Argon Pulsed Plasma”. In: *Journal of the Physical Society of Japan* 68.12, pp. 3885–3892. ISSN: 0031-9015. DOI: 10.1143/JPSJ.68.3885.

Bates, D. R. et al. (1962). “Recombination between electrons and atomic ions, I. Optically thin plasmas”. In: *Proceedings of the Royal Society of London. Series A. Mathematical and Physical Sciences* 267.1330, pp. 297–312. ISSN: 0080-4630. DOI: 10.1098/rspa.1962.0101.

Belmonte, Thierry et al. (2015). “Theoretical background of optical emission spectroscopy for analysis of atmospheric pressure plasmas”. In: *Plasma Sources Science and Technology* 24.6, p. 064003. ISSN: 0963-0252. DOI: 10.1088/0963-0252/24/6/064003.

Blackborow, P. et al. (2011). “Understanding Radiance (Brightness), Irradiance and Radiant Flux”. In: URL: https://www.energetiq.com/hubfs/Energetiq_March2019/PDF/Understanding%20Radiance%20(Brightness)%2c%20Irradiance%20and%20Radiant%20Flux%20-%20Mar%202011.pdf.

Blumenfeld, Ian et al. (2007). “Energy doubling of 42 GeV electrons in a metre-scale plasma wakefield accelerator”. In: *Nature* 445.7129, pp. 741–744. ISSN: 1476-4687. DOI: 10.1038/nature05538.

Boffard, John B. et al. (2009). “Measurement of metastable and resonance level densities in rare-gas plasmas by optical emission spectroscopy”. In: *Plasma Sources Science and Technology* 18.3, p. 035017. ISSN: 0963-0252. DOI: 10.1088/0963-0252/18/3/035017.

Boffard, John B. et al. (2010). “Optical emission measurements of electron energy distributions in low-pressure argon inductively coupled plasmas”. In: *Plasma Sources Science and Technology* 19.6, p. 065001. ISSN: 0963-0252. DOI: 10.1088/0963-0252/19/6/065001.

Broks, B. H.P. (2006). *Multi-fluid modeling of transient plasmas:a case study in the generation and guiding of light*. DOI: 10.6100/IR610194.

Butler, A. et al. (2002). “Guiding of high-intensity laser pulses with a hydrogen-filled capillary discharge waveguide”. In: *Physical Review Letters* 89.18, p. 185003. DOI: 10.1103/PhysRevLett.89.185003.

Carbone, E. A. D. et al. (2012). “Experimental investigation of the electron energy distribution function (EEDF) by Thomson scattering and optical emission spectroscopy”. In: *Journal of Physics D: Applied Physics* 45.47, p. 475202. ISSN: 0022-3727. DOI: 10.1088/0022-3727/45/47/475202.

Chen et al. (1985). “Acceleration of electrons by the interaction of a bunched electron beam with a plasma”. In: *Physical Review Letters* 54.7, pp. 693–696. DOI: 10.1103/PhysRevLett.54.693.

Chung, H.-K. et al. (2005). “FLYCHK: Generalized population kinetics and spectral model for rapid spectroscopic analysis for all elements”. In: *High Energy Density Physics* 1.1, pp. 3–12. ISSN: 15741818. DOI: 10.1016/j.hedp.2005.07.001.

Cristoforetti, G. et al. (2010). “Local Thermodynamic Equilibrium in Laser-Induced Breakdown Spectroscopy: Beyond the McWhirter criterion”. In: *Spectrochimica Acta Part B: Atomic Spectroscopy* 65.1, pp. 86–95. ISSN: 0584-8547. DOI: 10.1016/j.sab.2009.11.005.

D’Arcy, R. et al. (2019). “FLASHForward: plasma wakefield accelerator science for high-average-power applications”. In: *Philosophical transactions. Series A, Mathematical, physical, and engineering sciences* 377.2151, p. 20180392. DOI: 10.1098/rsta.2018.0392.

Deutsch, H. et al. (2004). “Calculated cross sections for the electron-impact ionization of excited argon atoms using the DM formalism”. In: *International Journal of Mass Spectrometry* 233.1-3, pp. 39–43. ISSN: 1387-3806. DOI: 10.1016/j.ijms.2003.10.016.

Donnelly, V. M. (2004). “Plasma electron temperatures and electron energy distributions measured by trace rare gases optical emission spectroscopy”. In: *Journal of Physics D: Applied Physics* 37.19, R217–R236. ISSN: 0022-3727. DOI: 10.1088/0022-3727/37/19/R01.

Drawin, H. W. (1969). “Validity conditions for local thermodynamic equilibrium”. In: *Zeitschrift für Physik* 228.2, pp. 99–119. DOI: 10.1007/BF01397532.

Durocher-Jean, Antoine et al. (2019). “Characterization of a microwave argon plasma column at atmospheric pressure by optical emission and absorption spectroscopy coupled with collisional-radiative modelling”. In: *Physics of Plasmas* 26.6, p. 063516. ISSN: 1070-664X. DOI: 10.1063/1.5089767.

Engelhardt, W. (1973). “Establishment of partial local thermal equilibrium in transient and inhomogeneous plasmas”. In: *The Physics of Fluids* 16.2, p. 217. ISSN: 0031-9171. DOI: 10.1063/1.1694321.

Esarey, E. et al. (2009). “Physics of laser-driven plasma-based electron accelerators”. In: *Reviews of Modern Physics* 81.3, pp. 1229–1285. DOI: 10.1103/RevModPhys.81.1229.

Evdokimov, K. E. et al. (2017). “Determination of the Electron Density and Electron Temperature in A Magnetron Discharge Plasma Using Optical Spectroscopy and the Collisional-Radiative Model of Argon”. In: *Russian Physics Journal* 60.5, pp. 765–775. ISSN: 1573-9228. DOI: 10.1007/s11182-017-1137-0.

Fantz, U. (2006). “Basics of plasma spectroscopy”. In: *Plasma Sources Science and Technology* 15.4, S137–S147. ISSN: 0963-0252. DOI: 10.1088/0963-0252/15/4/S01.

Fujimoto, Takashi (1973). “Validity Criteria for Local Thermodynamic Equilibrium and Coronal Equilibrium”. In: *Journal of the Physical Society of Japan* 34.1, pp. 216–224. ISSN: 0031-9015. DOI: 10.1143/JPSJ.34.216.

Fujimoto, Takashi (1979). “Kinetics of Ionization-Recombination of a Plasma and Population Density of Excited Ions. I. Equilibrium Plasma”. In: *Journal of the Physical Society of Japan* 47.1, pp. 265–272. ISSN: 0031-9015. DOI: 10.1143/JPSJ.47.265.

Fujimoto et al. (1990). “Validity criteria for local thermodynamic equilibrium in plasma spectroscopy”. In: *Physical review. A, Atomic, molecular, and optical physics* 42.11, pp. 6588–6601. ISSN: 1050-2947. DOI: 10.1103/PhysRevA.42.6588.

Gaigalas, A. K. et al. (2009). “Procedures for Wavelength Calibration and Spectral Response Correction of CCD Array Spectrometers”. In: *Journal of research of the National Institute of Standards and Technology* 114.4, pp. 215–228. ISSN: 1044-677X. DOI: 10.6028/jres.114.015.

Gangwar, R. K. et al. (2012). “Argon plasma modeling with detailed fine-structure cross sections”. In: *Journal of Applied Physics* 111.5, p. 053307. ISSN: 0021-8979. DOI: 10.1063/1.3693043.

García, M.C et al. (2000). “Spectroscopic study of a stationary surface-wave sustained argon plasma column at atmospheric pressure”. In: *Spectrochimica Acta Part B: Atomic Spectroscopy* 55.11, pp. 1733–1745. ISSN: 0584-8547. DOI: 10.1016/S0584-8547(00)00279-2.

Garland, J. M. et al. (2021). “Combining laser interferometry and plasma spectroscopy for spatially resolved high-sensitivity plasma density measurements in discharge capillaries”. In: *Review of Scientific Instruments* 92.1, p. 013505. ISSN: 0034-6748. DOI: 10.1063/5.0021117.

Gigosos, Marco A. et al. (1996). “New plasma diagnosis tables of hydrogen Stark broadening including ion dynamics”. In: *Journal of Physics B: Atomic, Molecular and Optical Physics* 29.20, pp. 4795–4838. ISSN: 0953-4075. DOI: 10.1088/0953-4075/29/20/029.

Gonsalves, A. J. et al. (2019). “Petawatt Laser Guiding and Electron Beam Acceleration to 8 GeV in a Laser-Heated Capillary Discharge Waveguide”. In: *Physical Review Letters* 122.8, p. 084801. DOI: 10.1103/PhysRevLett.122.084801.

Graef, WAAD Wouter (2012). “Zero-dimensional models for plasma chemistry”. In: DOI: 10.6100/IR733421.

Griem, Hans R. (1963). “Validity of Local Thermal Equilibrium in Plasma Spectroscopy”. In: URL: https://journals.aps.org/pr/pdf/10.1103/PhysRev.131.1170.

Griem, Hans R. (1997). *Principles of plasma spectroscopy*. Vol. 2. Cambridge monographs on plasma physics. Cambridge: Cambridge University Press. ISBN: 9780521455046. DOI: 10.1017/CBO9780511524578.

Hagelaar, G. J. M. et al. (2005). “Solving the Boltzmann equation to obtain electron transport coefficients and rate coefficients for fluid models”. In: *Plasma Sources Science and Technology* 14.4, pp. 722–733. ISSN: 0963-0252. DOI: 10.1088/0963-0252/14/4/011.

Hecht, Eugene (2017). *Optics*. 5 edition. Global edition. Boston: Pearson Education. ISBN: 9780133977226. URL: https://www.pearson.com/us/higher-education/program/Hecht-Optics-5th-Edition/PGM45350.html?tab=resources.

Hey, John D. (1976). “Criteria for local thermal equilibrium in non-hydrogenic plasmas”. In: *Journal of Quantitative Spectroscopy and Radiative Transfer* 16.1, pp. 69–75. ISSN: 00224073. DOI: 10.1016/0022-4073(76)90124-2.

Hey, John D. et al. (1999). “Partial local thermal equilibrium in a low-temperature hydrogen plasma”. In: *Journal of Quantitative Spectroscopy and Radiative Transfer* 62.3, pp. 371–387. ISSN: 00224073. DOI: 10.1016/S0022-4073(98)00110-1.

Holstein, T. (1947). “Imprisonment of Resonance Radiation in Gases”. In: *Physical Review* 72.12, pp. 1212–1233. DOI: 10.1103/PhysRev.72.1212.

Hooker, S. M. (2013). “Developments in laser-driven plasma accelerators”. In: *Nature Photonics* 7.10, pp. 775–782. ISSN: 1749-4893. DOI: 10.1038/nphoton.2013.234.

Iordanova, S. et al. (2007). “Optical emission spectroscopy diagnostics of inductively-driven plasmas in argon gas at low pressures”. In: *Spectrochimica Acta Part B: Atomic Spectroscopy* 62.4, pp. 344–356. ISSN: 0584-8547. DOI: 10.1016/j.sab.2007.03.026.

Kano, K. et al. (2000). “Spectroscopic measurement of electron temperature and density in argon plasmas based on collisional-radiative model”. In: *Plasma Sources Science and Technology* 9.3, pp. 314–322. ISSN: 0963-0252. DOI: 10.1088/0963-0252/9/3/309.

Karsch, S. et al. (2007). “GeV-scale electron acceleration in a gas-filled capillary discharge waveguide”. In: *New Journal of Physics* 9.11, p. 415. ISSN: 1367-2630. DOI: 10.1088/1367-2630/9/11/415.

Kimura, A. et al. (1985). “Calculation of collisional and radiative transition probabilities between excited argon levels”. In: *Journal of Quantitative Spectroscopy and Radiative Transfer* 34.2, pp. 189–215. ISSN: 00224073. DOI: 10.1016/0022-4073(85)90046-9.

Kramida, Alexander et al. (2020). *NIST Atomic Spectra Database (ver. 5.8), NIST Standard Reference Database 78*. DOI: 10.18434/T4W30F.

Kunze, Hans-Joachim (2009). *Introduction to Plasma Spectroscopy*. Vol. 56. Berlin, Heidelberg: Springer Berlin Heidelberg. ISBN: 978-3-642-02232-6. DOI: 10.1007/978-3-642-02233-3.

L C Pitchford et al. (2013). “Comparisons of sets of electron–neutral scattering cross sections and swarm parameters in noble gases: I. Argon”. In: *Journal of Physics D: Applied Physics* 46.33, p. 334001. ISSN: 0022-3727. DOI: 10.1088/0022-3727/46/33/334001.

Lao, C. et al. (2002). “Excitation Equilibria in an Argon Surface-Wave-Produced and -Sustained Plasmas”. In: *Japanese Journal of Applied Physics* 41.Part 1, No. 9, pp. 5659–5667. ISSN: 0021-4922. DOI: 10.1143/JJAP.41.5659.

Leemans, W. P. et al. (2014). “Multi-GeV electron beams from capillary-discharge-guided subpetawatt laser pulses in the self-trapping regime”. In: *Physical Review Letters* 113.24, p. 245002. DOI: 10.1103/PhysRevLett.113.245002.

Lindstrøm, C. A. et al. (2018). “Emittance Preservation in an Aberration-Free Active Plasma Lens”. In: *Physical Review Letters* 121.19, p. 194801. DOI: 10.1103/PhysRevLett.121.194801.

Litos, M. et al. (2014). “High-efficiency acceleration of an electron beam in a plasma wakefield accelerator”. In: *Nature* 515.7525, pp. 92–95. ISSN: 1476-4687. DOI: 10.1038/nature13882.

LXCat (2022). *Plasma Data Exchange Project*. URL: www.lxcat.net.

Malyshev, M. V. et al. (1999). “Trace rare gases optical emission spectroscopy: nonintrusive method for measuring electron temperatures in low-pressure, low-temperature plasmas”. In: *Physical review. E, Statistical physics, plasmas, fluids, and related interdisciplinary topics* 60.5 Pt B, pp. 6016–6029. ISSN: 1063-651X. DOI: 10.1103/physreve.60.6016.

Mendys, A. et al. (2014). “Investigation of the local thermodynamic equilibrium of laser-induced aluminum plasma by Thomson scattering technique”. In: *Spectrochimica Acta Part B: Atomic Spectroscopy* 96, pp. 61–68. ISSN: 0584-8547. DOI: 10.1016/j.sab.2014.03.009.

Mewe, R. (1967). “Relative intensity of helium spectral lines as a function of electron temperature and density”. In: *British Journal of Applied Physics* 18.1, pp. 107–118. ISSN: 0508-3443. DOI: 10.1088/0508-3443/18/1/315.

Newville, Matthew et al. (2014). *LMFIT: Non-Linear Least-Square Minimization and Curve-Fitting for Python*. DOI: 10.5281/ZENODO.11813.

Newville, Matthew et al. (2021). “Non-Linear Least-Squares Minimization and Curve-Fitting for Python”. In: URL: https://lmfit.github.io/lmfit-py/lmfit.pdf.

Ohno, Noriyasu et al. (2006). “Validity of Electron Temperature Measurement by Using Boltzmann Plot Method in Radio Frequency Inductive Discharge in the Atmospheric Pressure Range”. In: *Plasma and Fusion Research* 1, p. 028. ISSN: 1880-6821. DOI: 10.1585/pfr.1.028.

Panofsky, W. K. H. et al. (1950). “A Focusing Device for the External 350–Mev Proton Beam of the 184–Inch Cyclotron at Berkeley”. In: *Review of Scientific Instruments* 21.5, pp. 445–447. ISSN: 0034-6748. DOI: 10.1063/1.1745611.

Parigger, Christian et al. (2018). “Laboratory Hydrogen-Beta Emission Spectroscopy for Analysis of Astrophysical White Dwarf Spectra”. In: *Atoms* 6.3, p. 36. DOI: 10.3390/atoms6030036.

Piel, Alexander (2017). *Plasma physics: An introduction to laboratory, space, and fusion plasmas / Alexander Piel*. Second edition. Graduate texts in physics, 1868-4513. Cham, Switzerland: Springer. ISBN: 978-3-319-63425-8. DOI: 10.1007/978-3-319-63427-2.

Pitchford, Leanne C. et al. (2017). "LXCat: an Open-Access, Web-Based Platform for Data Needed for Modeling Low Temperature Plasmas". In: *Plasma Processes and Polymers* 14.1-2, p. 1600098. ISSN: 16128850. DOI: 10.1002/ppap.201600098.

Polyanskiy, Mikhail N. (2022). *Refractive index database: Optical constants of Al2O3 (Aluminium sesquioxide, Sapphire, Alumina)*. URL: https://refractiveindex.info/?shelf=main&book=Al2O3&page=Malitson-o.

Savitzky, Abraham. et al. (1964). "Smoothing and Differentiation of Data by Simplified Least Squares Procedures". In: *Analytical Chemistry* 36.8, pp. 1627–1639. ISSN: 0003-2700. DOI: 10.1021/ac60214a047.

Sawada et al. (1994). "Temporal relaxation of excited-level populations of atoms and ions in a plasma: Validity range of the quasi-steady-state solution of coupled rate equations". In: *Physical review. E, Statistical physics, plasmas, fluids, and related interdisciplinary topics* 49.6, pp. 5565–5573. ISSN: 1063-651X. DOI: 10.1103/PhysRevE.49.5565.

Siepa, Sarah et al. (2014). "On the OES line-ratio technique in argon and argon-containing plasmas". In: *Journal of Physics D: Applied Physics* 47.44, p. 445201. ISSN: 0022-3727. DOI: 10.1088/0022-3727/47/44/445201.

Spence, D. J. et al. (2003). "Gas-filled capillary discharge waveguides". In: *JOSA B* 20.1, p. 138. ISSN: 1520-8540. DOI: 10.1364/JOSAB.20.000138.

Tajima, T. et al. (1979). "Laser Electron Accelerator". In: *Physical Review Letters* 43.4, pp. 267–270. DOI: 10.1103/PhysRevLett.43.267.

van der Mullen, J. A. M. (1986). *Excitation equilibria in plasmas : a classification*. URL: https://pure.tue.nl/ws/portalfiles/portal/3554256/194154.pdf.

van der Mullen, J. A. M. (1990). "Excitation equilibria in plasmas; a classification". In: *Physics Reports* 191.2-3, pp. 109–220. ISSN: 0370-1573. DOI: 10.1016/0370-1573(90)90152-R.

van Regemorter, Henri (1962). "Rate of Collisional Excitation in Stellar Atmospheres". In: *The Astrophysical Journal* 136, p. 906. ISSN: 0004-637X. DOI: 10.1086/147445.

Vries, N. d. et al. (2006). "A spectroscopic method to determine the electron temperature of an argon surface wave sustained plasmas using a collision radiative model". In: *Journal of Physics D: Applied Physics* 39.19, pp. 4194–4203. ISSN: 0022-3727. DOI: 10.1088/0022-3727/39/19/011.

Wang, Fei et al. (2018). "Spectroscopic investigation of partial LTE assumption and plasma temperature field in pulsed MAG arcs". In: *Journal of Physics D: Applied Physics* 51.25, p. 255203. ISSN: 0022-3727. DOI: 10.1088/1361-6463/aac47f.

Wiese, W. L. (1991). “Spectroscopic diagnostics of low temperature plasmas: techniques and required data”. In: *Spectrochimica Acta Part B: Atomic Spectroscopy* 46.6-7, pp. 831–841. ISSN: 0584-8547. DOI: 10.1016/0584-8547(91)80084-G.

Wiese, W. L. et al. (1975). “Variations in Balmer-line Stark profiles with atom-ion reduced mass”. In: *Physical review. A, General physics* 11.6, pp. 1854–1864. ISSN: 0556-2791. DOI: 10.1103/PhysRevA.11.1854.

Wiese et al. (1989). “Unified set of atomic transition probabilities for neutral argon”. In: *Physical review. A, General physics* 39.5, pp. 2461–2471. ISSN: 0556-2791. DOI: 10.1103/PhysRevA.39.2461.

Wünderlich, D. et al. (2020). “Yacora on the Web: Online collisional radiative models for plasmas containing H, H2 or He”. In: *Journal of Quantitative Spectroscopy and Radiative Transfer* 240, p. 106695. ISSN: 00224073. DOI: 10.1016/j.jqsrt.2019.106695.

Xiong, Q. et al. (2011). “A simple profile-fitting method to determine the metastable and resonant densities in a cold atmospheric pressure argon plasma jet”. In: *Journal of Applied Physics* 110.7, p. 073302. ISSN: 0021-8979. DOI: 10.1063/1.3643004.

Yuan, Qun et al. (2017). *Comparative assessment of astigmatism-corrected Czerny-Turner imaging spectrometer using off-the-shelf optics*. Vol. 388. DOI: 10.1016/j.optcom.2016.11.004.

Zalach, J. et al. (2013). “Iterative Boltzmann plot method for temperature and pressure determination in a xenon high pressure discharge lamp”. In: *Journal of Applied Physics* 113.4, p. 043303. ISSN: 0021-8979. DOI: 10.1063/1.4788701.

Zatsarinny, Oleg et al. (2006). “B -spline calculations of oscillator strengths in neutral argon”. In: *Journal of Physics B: Atomic, Molecular and Optical Physics* 39.9, pp. 2145–2158. ISSN: 0953-4075. DOI: 10.1088/0953-4075/39/9/004.

Zatsarinny, Oleg et al. (2014). “Electron-impact excitation of argon at intermediate energies”. In: *Physical review. A, Atomic, molecular, and optical physics* 89.2, p. 022706. ISSN: 1050-2947. DOI: 10.1103/PhysRevA.89.022706.

Zhang, Hantian et al. (2019). “Application of Calibration-Free Boltzmann Plot Method for Composition and Pressure Measurement in Argon Free-Burning Arcs”. In: *Plasma Chemistry and Plasma Processing* 39.6, pp. 1429–1447. ISSN: 0272-4324.

Zhu, Xi-Ming et al. (2010a). “A simple collisional–radiative model for low-temperature argon discharges with pressure ranging from 1 Pa to atmospheric pressure: kinetics of Paschen 1s and 2p levels”. In: *Journal of Physics D: Applied Physics* 43.1, p. 015204. ISSN: 0022-3727. DOI: 10.1088/0022-3727/43/1/015204.

Zhu, Xi-Ming et al. (2010b). “Optical emission spectroscopy in low-temperature plasmas containing argon and nitrogen: determination of the electron temperature and density by the line-ratio method”.

In: *Journal of Physics D: Applied Physics* 43.40, p. 403001. ISSN: 0022-3727. DOI: 10.1088/0022-3727/43/40/403001.

Zhu, Xi-Ming et al. (2012). "Possibilities of determining non-Maxwellian EEDFs from the OES line-ratios in low-pressure capacitive and inductive plasmas containing argon and krypton". In: *Plasma Sources Science and Technology* 21.2, p. 024003. ISSN: 0963-0252. DOI: 10.1088/0963-0252/21/2/024003.

Zhu, Xi-Ming et al. (2016). "Escape factors for Paschen 2p–1s emission lines in low-temperature Ar, Kr, and Xe plasmas". In: *Journal of Physics D: Applied Physics* 49.22, p. 225204. ISSN: 0022-3727. DOI: 10.1088/0022-3727/49/22/225204.

Zhu, X. M. et al. (2009). "Measurement of the electron density in atmospheric-pressure low-temperature argon discharges by line-ratio method of optical emission spectroscopy". In: *Journal of Physics D: Applied Physics* 42.14, p. 142003. ISSN: 0022-3727. DOI: 10.1088/0022-3727/42/14/142003.

Auxiliaries

I used Python (v. 3.8.12) for data analysis, modelling and plotting in combination with the Spyder IDE (v. 5.1.5) and especially the LMFIT (v. 1.0.1) package for line fitting. I used LaTeX (LuaLaTex) and TeXstudio (v. 4.1.2) for text processing and Inkscape for drawings. I used Citavi for literature management and the ‘Web of Science’ and ‘Google Scholar’ webpages for literature research.

Eidesstattliche Erklärung

Ich versichere, dass ich die beigefügte schriftliche Masterarbeit selbstständig angefertigt und keine anderen als die angegebenen Hilfsmittel benutzt habe. Alle Stellen, die dem Wortlaut oder dem Sinn nach anderen Werken entnommen sind, habe ich in jedem einzelnen Fall unter genauer Angabe der Quelle deutlich als Entlehnung kenntlich gemacht. Dies gilt auch für alle Informationen, die dem Internet oder anderer elektronischer Datensammlungen entnommen wurden. Ich erkläre ferner, dass die von mir angefertigte Masterarbeit in gleicher oder ähnlicher Fassung noch nicht Bestandteil einer Studien- oder Prüfungsleistung im Rahmen meines Studiums war. Die von mir eingereichte schriftliche Fassung entspricht jener auf dem elektronischen Speichermedium.

Ich bin damit einverstanden, dass diese Masterarbeit veröffentlicht wird.

Hamburg, den 16. Mai 2022

Ort, Datum

Julian Hörsch